UNIVERSITY OF CALIFORNIA

IRVINE

A Study of Select Decays of J/ψ and ψ' States Produced in Antiproton-Proton Annihilations

DISSERTATION

submitted in partial satisfaction of the requirements for the degree of

DOCTOR OF PHILOSOPHY

in Physics

by

Andrew James Smith

Dissertation Committee:

Professor Mark Mandelkern, Co-Chair

Professor Jonas Schultz, Co-Chair

Professor Myron Bander

1996

The dissertation of Andrew James Smith is approved,

and is acceptable in quality and form

for publication on microfilm:

Committee Co-Chair

Committee Co-Chair

University of California, Irvine

1996

Contents

List of Figures

List of Tables

Acknowledgement

This is where I thank people.

Curriculum Vitae

B.S.	University of California, Davis, Physics, 1988
M.S.	University of California, San Diego, Physics, 1990
Ph.D.	University of California, Physics (expected September 1996) Thesis topic: Study of Select Decays of J/ψ and ψ' Produced in Antiproton-Proton Annihilations Thesis Advisor: Professor Mark A. Mandelkern and Professor Jonas Schultz

PUBLICATIONS

T.A. Armstrong *et al.*, Observation of the $^1P_1$ State of Charmonium, Phys. Rev. Lett. **69** (1992) 2337.

J.Z. Bai *et al.*, Measurement of the Mass of the τ lepton, Phys. Rev. Lett., **69** (1992) 3021.

T.A. Armstrong *et al.*, Measurement of the J/ψ and ψ' Resonance Param-eters in $\bar{p}p$ Annihilations, Phys. Rev. D **47** (1993) 772.

T.A. Armstrong *et al.*, Proton Electromagnetic Form Factors in the Time-like Region form 8.9 to 13.0 GeV^2, Phys. Rev. Lett. **70** (1993) 1212.

T.A. Armstrong *et al.*, Measurement of the $\gamma\gamma$ Partial Width of the χ_2 Charmonium Resonance, Phys. Rev. Lett. **70** (1993) 2988.

T.A. Armstrong *et al.* , Evidence for $\eta\eta$ Resonances in Antiproton-Proton Annihilations at $2950 < \sqrt{s} < 3620$ MeV, Phys. Lett. B **307** (1993) 394.

T.A. Armstrong *et al.*, Production of the $f_2(1520)$ Resonance in Antiproton-Proton Annihilations at $2980 < \sqrt{s} < 3526$ MeV, Phys. Lett. B **307** (1993) 399.

T.A. Armstrong *et al.*, Charmonium Formation in $\bar{p}p$ Annihilations by Experiment E-760. Nuclear Physics A, **5**58 (1993) 259.

T.A. Armstrong *et al.*, Light Quark Spectroscopy at the Fermilab Antiproton Accumulator. Nuclear Physics A, **5**58 (1993) 259.

T.A. Armstrong *et al.*, Study of the Angular Distribution of the Reaction $\bar{p}p \rightarrow J/\psi\gamma \rightarrow e^+e^-\gamma$, Phys. Rev. D **4**8 (1993) 3037.

J.Z. Bai *et al.*, Direct Measurement of the Pseudoscalar Decay Constant, F_{D_S}. Phys. Rev. Lett., **73** (1995) 4599.

J.Z. Bai *et al.*, Direct Measurement of the D_s Branching Fraction to $\phi\pi$. Phys. Rev. D **5**2 (1995) 3781

T.A. Armstrong *et al.*, Study of the η_c (1 $^1\mathrm{S}_0$) State of Charmonium Formed in $\bar{p}p$ Annihilations and a Search for the η_c' (2 $^1\mathrm{S}_0$). Phys. Rev. D **5**2 (1995) 4839.

J.Z. Bai *et al.*, Measurement of the Mass of the τ lepton. Phys. Rev. D **5**3 (1996) 20.

T.A. Armstrong *et al.*, Observation of the Radiative decay $J/\psi \rightarrow e^+e^-\gamma$. In Preparation.

T.A. Armstrong *et al.*, Measurement of the Branching Ratios $\psi' \rightarrow e^+e^-$, $\psi' \rightarrow J/\psi\pi\pi$ and $\psi' \rightarrow J/\psi\eta$. In Preparation.

Abstract of the Dissertation

A Study of Select Decays of J/ψ and ψ' States Produced in Antiproton-Proton Annihilations

by

Andrew James Smith

Doctor of Philosophy in Physics

University of California, Irvine, 1996

Professor Jonas Schultz, Co-Chair

Professor Mark A. Mandelkern, Co-Chair

The E760 Collaboration performed an experiment in the Antiproton Accumulator at Fermilab to study resonant formation of the J/ψ and ψ' charmonium states formed in $\bar{p}p$ annihilations. Decays to high mass e^+e^- pairs are detected with a non-magnetic spectrometer. By comparing the numbers of events detected through the decay channels $\psi' \to e^+e^-$, $\psi' \to J/\psi\pi^+\pi^-$, $\psi' \to J/\psi\pi^o\pi^o$, and $\psi' \to J/\psi\eta$ with the total number of J/ψ inclusive events ($\psi' \to J\psi X$) the experiment made a new measurements of the branching fractions $B(\psi' \to e^+e^-) = (.83 \pm .05_{stat} \pm .07_{syst}) \times 10^{-2}$, $B(\psi' \to J/\psi\pi^+\pi^-) = (28.3 \pm 2.1_{stat} \pm 2.0_{syst}) \times 10^{-2}$, $B(\psi' \to J/\psi\pi^o\pi^o -) = (18.4 \pm 1.9_{stat} \pm 1.3_{syst}) \times 10^{-2}$ and $B(\psi' \to J/\psi\eta) = (3.5 \pm 0.9_{stat} \pm 0.2_{syst}) \times 10^{-2}$. The

angular distributions of J/ψ and ψ' decays were studied. The angular distribution for the reactions $J/\psi \to e^+e^-$ is fit to the theoretical angular distribution $1 + \lambda_{J/\psi} cos^2\theta_e$ where and $\lambda_{J/\psi}$ was found to be 0.91 ± 0.19. The angular distribution of ψ' decays to e^+e^- and $J/\psi X$ were found to be described by $\lambda_{\psi'} = 0.69 \pm 0.26$. The decay $J/\psi \to e^+e^-\gamma$ was observed and found to be consistent with the expected rate for final state radiation.

Chapter 1

Introduction

Fermilab experiment E760 was designed for the study of charmonium states produced in $\bar{p}p$ annhihilations. Charmonium is a bound state of a charm quark (c) and an anticharm quark ($\bar{c}$). Since the discovery of charmonium in 1974, numerous experiments have studied its properties. However, precise measurements of the states that do not have quantum numbers of the photon ($J^{PC} = 1^{--}$) were not well measured, because they could not be directly formed in electron-positron colliders. In E760 charmonium is produced in $\bar{p}p$ annhihilations, where all charmonium states are directly accessible. Direct measurements of the mass and width of the χ_1 and the χ_2 states[1] and discovery of the h_c state [2] are among this experiments numerous contributions [3, 4, 5, 6, 7, 8]. Because charmonium is produced in $\bar{p}p$ annhihilations, this experiment also provides a unique laboratory for the study of the decays of the 1^{--} charmonium states to e^+e^-, a decay channel that has high backgrounds from direct scattering in electron positron colliders. This dissertation is a study of such decays.

1.1 The discovery of charmonium

In 1964, Gell-Mann and Zweig [9, 10] independently devised a system for categorizing hadrons based on their charge, spin and strangeness. They proposed that hadrons were composed of constituent particles which Gell-Mann called quarks. Three "flavors" of quarks (up (u), down (d), and strange (s)) were required to account for the spectrum of known baryons and mesons. In the same year, Bjorken and Glashow [11] proposed the existence of a fourth quark, charm (c), to symmetrize the quark system with the lepton system. Leptons e and μ were known to exist paired with neutrino counterparts ν_e and ν_μ. If the same were true of the quark system then a fourth quark is required to form a pair with the s quark.

In 1970, Glashow, Iliopoulos, and Maiani [12] (GIM) demonstrated that the existence of a fourth quark could explain the observed rates of weak decays. The GIM mechanism exploits an idea proposed by Cabibbo [13] that the weak interaction mixes the d and s quarks and extends it to a system of two quark generations, (u,d) and (c,s). In this formalism, mixing between generations could explain observed rates for flavor changing decays. This work was later generalized to three generations by Kobayashi and Masakawa [14] in 1973.

In 1974, Gaillard and Lee [15] estimated that the proposed charm quark mass to be about 1.5 $\frac{GeV}{c^2}$ based on measurements of the $K_L^0 - K_S^0$ mass difference. In the same year, Appelquist and Politzer [16] predicted that the charm quark would form bound states in a spectrum similar to positronium, which they called "charmonium". Both predictions were made prior to the discovery of any direct experimental evidence for the existence of the charm quark.

In November of 1974 the charm quark was discovered independently by two research groups[17, 18]. Scientists at Brookhaven National Laboratory (BNL) identified a narrow resonance at about 3.1 $\frac{GeV}{c^2}$, produced in proton beryllium collisions, that decayed to electron positron pairs. The same resonance was seen by physicists at the Stanford Linear Accelerator Laboratory's SPEAR electron storage ring, by what would later be called the Mark-I experiment. The BNL group named the new res-

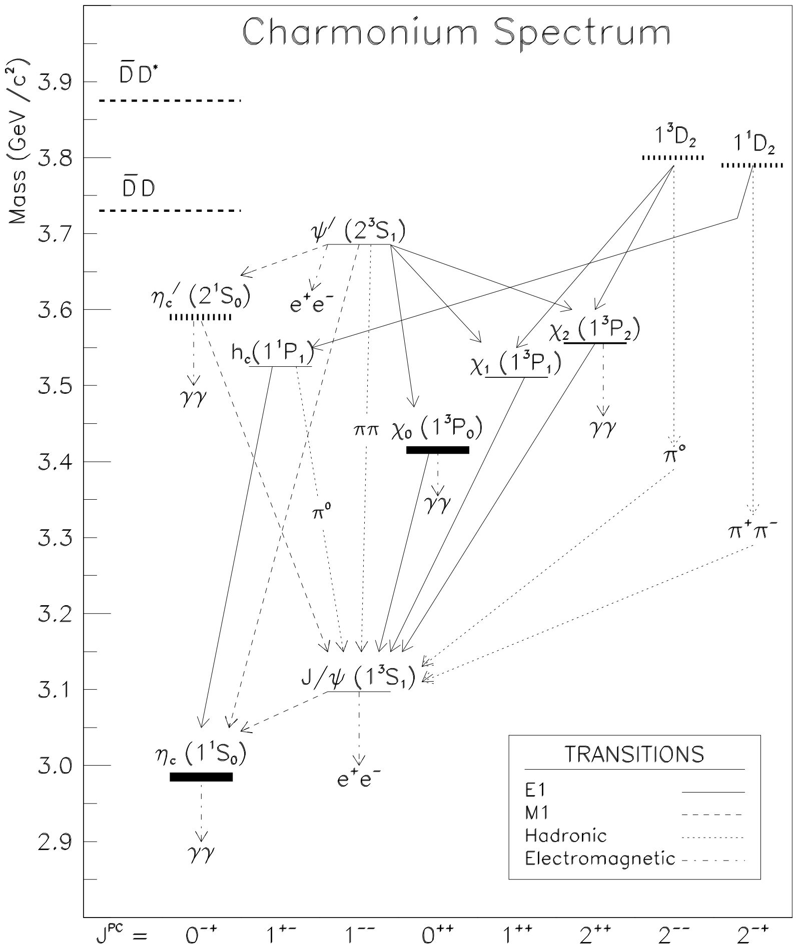

Figure 1.1: The charmonium spectrum.

onance J and the SLAC group named it ψ. The discovery of the what we now call the J/ψ was a critical step in the understanding of the nature of matter. The J/ψ was quickly identified as a 1^3S_1 bound state of a charm and an anticharm quark. Subsequent searches lead to the discovery of a spectrum of charm quark bound states (figure 1.1).

Although a total of six quarks have been discovered, the charm quark remains a subject of much study. Unlike the lighter u,d,s quarks, eight charmonium bound states reside below the open charm threshold. Strong and electromagnetic decays of these states can only occur through transitions from one bound state to another or by annihilation of the charm quark constituents. Weak decays are highly supressed. This is easily observed by comparing the decay lifetime of the D^0 meson, a bound state of a charm and a light quark which undergoes weak decays only, with charmonium lifetimes. The D^0 decays in $10^{-12}s$ while charmonium states decay in about $10^{-22}s$. Furthermore, because the mass of the charm quark is large compared with the charmonium binding energy, non-relativistic potential models can be used to test predictions of quantum chromodynamics (QCD). The same is true for heavier bottom (b) quark bound states, but the heaviest quark, the top (t), if it forms bound states at all, forms bound states that are hopelessly mixed because their mass separations are small compared to the resonance widths.

1.2 Charmonium production in e^+e^- annhihilations

Since the discovery of charmonium, its properties have been studied by numerous electron positron collider experiments. Charmonium states J/ψ and ψ' can be copiously produced in e^+e^- collisions. Several tens of millions of J/ψ's and a few million ψ''s have been produced in this manner. These experiments have low background rates for most of the decay channels. In e^+e^- colliders, charmonium states are produced through a virtual photon (figure 1.4a). Only charmonium states with the quantum numbers of the photon ($J^{PC} = 1^{--}$) can be formed directly using this method. In these e^+e^- experiments, the remaining six charmonium states below the $D\bar{D}$ threshold can only be studied through the decays of J/ψ and ψ' states.

Although the backgrounds for the process $e^+e^- \to J/\psi(\psi') \to hadrons$ has almost no background from the non-resonant process, the process $e^+e^- \to J/\psi(\psi') \to e^+e^-$ has a large background from direct elastic scattering. Figures 1.2 and 1.3 show the line shapes for J/ψ and ψ' resonance scans from the Mark-I experiment [19, 20]. The signal to background ratio for the J/ψ resonance scan for the process $e^+e^- \to J/\psi \to e^+e^-$ is about 2:1 at the peak and the decay of ψ' to e^+e^- is almost undetectable. Fits to the data from these resonance scans were used to measure the resonance mass, width, and the branching ratios to hadrons, $\mu^+\mu^-$ and e^+e^-. In the case of the ψ', the decay of the ψ' to e^+e^- was excluded from the fit, but the branching fraction $\mathrm{B}(\psi' \to e^+e^-)$ could still be measured from the input channel for ψ' formation. These data were collected in the months following the discovery of the J/ψ and ψ'. Of numerous electron positron collider experiments operated since, only the DASP experiment[21] has performed a careful resonance scan to remeasure these resonance parameters.

Recently, the Mark-III experiment measured the branching ratio $\mathrm{B}(J/\psi \to e^+e^-)$ [22] by studying the process $\psi' \to J/\psi\pi^+\pi^-$. Detection of the two pions identifies the event. Counting the total number of observed events and the number of events in which the J/ψ decays to e^+e^- gives a direct measurement of $\mathrm{B}(J/\psi \to e^+e^-)$. The error in the Mark-III measurement is 4 times smaller than Mark-I's and free from the systematic errors associated with resonance scans.

In this dissertation, a new measurement of the branching fraction $\mathrm{B}(\psi' \to e^+e^-)$ is presented. Because this experiment produces ψ' in $\bar{p}p$ annihilations, there is negligible background from non-resonant processes. The total number of ψ' events is estimated by counting the number ψ' events that decay to $J/\psi X$, where the J/ψ subsequently decays to e^+e^-. Relatively well measured branching fractions for the processes $\psi' \to J/\psi X$ and $J/\psi \to e^+e^-$ are the limiting systematic error in the measurement. Detailed studies of the angular distribution of ψ' and J/ψ decays, measurements of branching

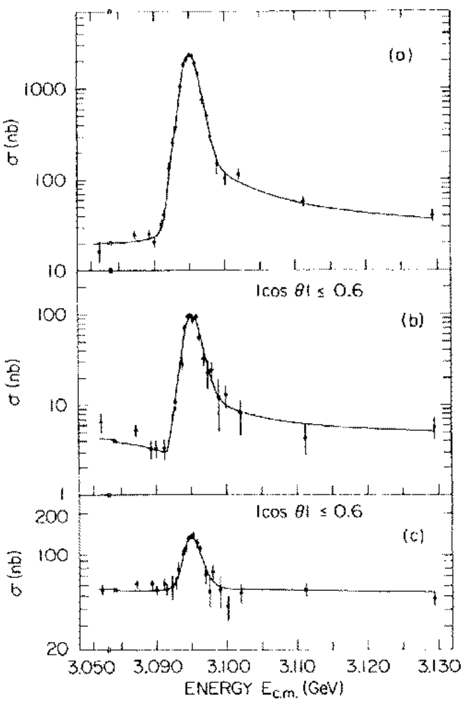

Figure 1.2: Data from the Mark-I J/ψ resonance scan. The top plot is the cross section for the process $e^+e^- \rightarrow hadrons$, the middle plot is the cross section for the process $e^+e^- \rightarrow \mu^+\mu^-$ and the bottom plot is the cross section for the process $e^+e^- \rightarrow e^+e^-$.

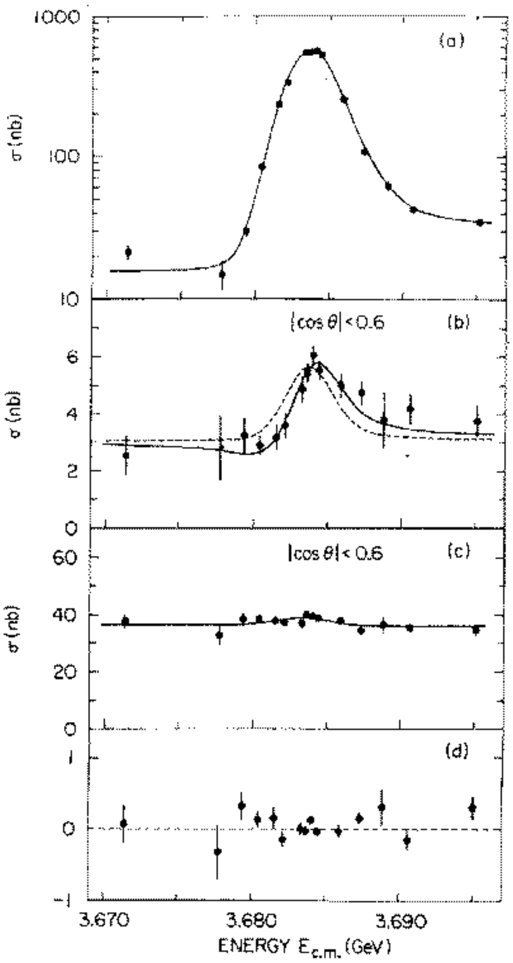

Figure 1.3: Data from the Mark-I ψ' resonance scan. The top plot is the cross section for the process $e^+e^- \to hadrons$, the middle plot is the cross section for the process $e^+e^- \to \mu^+\mu^-$ and the bottom plot is the cross section for the process $e^+e^- \to e^+e^-$.

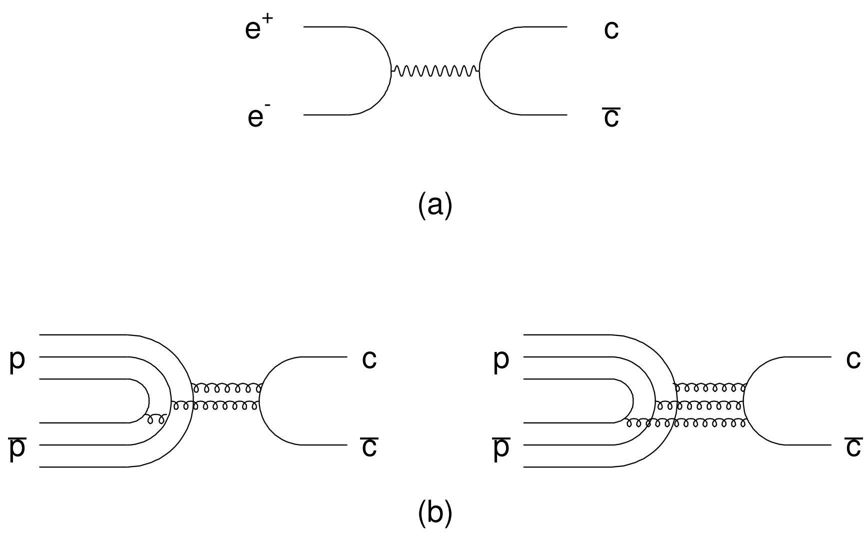

Figure 1.4: Diagrams for (a) production of charmonium in e^+e^- through a virtual photon and (b) production of charmonium in $\bar{p}p$ through two or three gluons.

fractions B($\psi' \to J/\psi\pi\pi$) and B($\psi' \to J/\psi\eta$) and observation of the radiative decay $J/\psi \to e^+e^-\gamma$ are also presented.

1.3 Charmonium production in $\bar{p}p$ annhihilations

In proton-antiproton annihilations all charmonium states can be directly produced. Charmonium resonances of even spin are produced through a two gluon intermediate state and resonances of odd spin are produced through a three gluon intermediate state (figure 1.4b). In 1985, CERN experiment R704 [23, 24, 25, 26] developed a technique of stochastically cooling an antiproton beam and colliding it with a hydrogen target. A two-arm spectrometer was used to detect J/ψ decays to e^+e^-. The techniques developed by R704 were refined in E760. The E760 detector has a larger acceptance and full azimuthal coverage. The Fermilab Antiproton facility has roughly ten times the luminosity as the ISR facility at CERN where R704 was situated.

Chapter 2

Theory

In this chapter, the theory of the production of J/ψ and ψ' charmonium resonances in $\bar{p}p$ annihilations and their decays to e^+e^- is presented. Also presented is a detailed analysis, in the helicity formalism, of the angular distribution of $\psi' \to J/\psi X$ decays.

2.1 J/ψ and ψ' decay to e^+e^-

The decay width for 1^{--} charmonium states to light lepton pairs is

$$\Gamma_{ee\ or\ \mu\mu} = \frac{64\pi\alpha^2}{9M_{c\bar{c}}^2}|\phi_{c\bar{c}}(0)|^2\left[1 - \frac{16}{3\pi}\alpha_s(M_c^2)\right]. \tag{2.1}$$

In this expression, α is the fine structure constant, α_s is the coupling constant for the strong force, $M_{c\bar{c}}$ is the mass of the charmonium state and $|\phi_{c\bar{c}}(0)|$ is the value of the charmonium wave function at the origin. Measurement of the decay widths of $J/\psi \to e^+e^-$ and $J/\psi \to ggg \to hadrons$ have been used to isolate $\alpha_s(M_{J/\psi}^2)$ [22]. At the ψ', the hadronic decays that proceed through the reaction $\psi' \to ggg$ are obscured by the transition decays to other charmonium states where the second charmonium state subsequently decays hadronically. Therefore, the method used at the J/ψ for measurement α_s is not suitable for use at the ψ' resonance.

ψ' decays to lepton pairs have been used by many experiments as a method of cleanly identifying charmonium states. The limiting systematic error in such experiments is typically the branching ratio of ψ' to lepton pairs. The new measurement of $Br(\psi' \to e^+e^-)$ should provide a substantial improvement for many experimental results.

2.2 Production of J/ψ and ψ' in $\bar{p}p$ annihilations

The coupling of the 1^{--} charmonium states, J/ψ and ψ', to the antiproton and the proton is described in a manner exactly analogous to the coupling of the proton and antiproton to a time-like virtual photon originally calculated by Rosenbluth [27]. In this case the massless vector boson (photon) is replaced by a massive vector boson (J/ψ or ψ'). The transverse and longitudinal polarizations of the produced charmonium states are

$$T = \frac{E^2}{E^2 + 4|\frac{G_E}{G_M}|^2 M_p^2}, \tag{2.2}$$

$$L = \frac{4|\frac{G_E}{G_M}|^2 M_p^2}{E^2 + 4|\frac{G_E}{G_M}|^2 M_p^2}. \tag{2.3}$$

M_p is the proton mass and G_E and G_M are the "electric" and "magnetic" Sachs form factors. Note that the form factors, G_E and G_M, are not the electromagnetic form factors of the proton. They are specific to the charmonium state formed.

The processes $\bar{p}p \to J/\psi \to e^+e^-$ and $\bar{p}p \to \psi' \to e^+e^-$ will be shown to have electron angular distributions described by

$$\frac{dN}{dcos\theta} \propto 1 + \lambda cos^2\theta_e, \qquad \lambda = \frac{E_{CM}^2 - 4\left|\frac{G_E}{G_M}\right|^2 M_p^2}{E_{CM}^2 + 4\left|\frac{G_E}{G_M}\right|^2 M_p^2}. \tag{2.4}$$

Where E_{CM} is the $\bar{p}p$ center of mass energy and M_p is the proton mass. The Sachs form factors are related to the Pauli form factors by the expressions

$$G_E \equiv F_1 + \frac{q^2}{4M_p^2} F_2, \tag{2.5}$$

$$G_M \equiv F_1 + F_2. \tag{2.6}$$

If the proton were a structureless fermion, such as e or μ, then the Pauli form factor F_2 is zero and the ratio $\frac{G_E}{G_M}$ would be 1. The angular distribution would then be described by $\lambda = \frac{E_{CM}^2 - 4M_p^2}{E_{CM}^2 + 4M_p^2}$, or $\lambda_{J/\psi} = 0.46$ and $\lambda_{\psi'} = 0.59$. Deviation from these predicted values is a measure of the proton's structure.

Claudson, Glashow and Wise[28] assume that in the limit that the quark masses can be neglected, the $\bar{q}qg$ vertex must conserve helicity due to the vectorial nature of the gluon. This result of perturbative QCD is used in the form factor formalism of spin-$\frac{1}{2}$ particles to perform corrections due to the proton mass. They predict that $F_2 = 0$.

Carimalo [29] accounts for the non-negligible proton mass by assuming that the quark masses are equal to $\frac{1}{3}M_p$. This method leads to $|\frac{G_E}{G_M}|^2 = 0.5$, predicting $\lambda_{J/\psi} = 0.69$ and $\lambda_{\psi'} = 0.72$.

Murgia and Melis [30] generalized the work of Carimalo. They demonstrate that the the angular distribution of J/ψ decays can be used to measure the hadronic distribution amplitudes (DA) which describe how the momentum is shared among the valence constituents of the proton. $\lambda_{J/\psi}$ is calculated using several different QCD sum rules for DA's. Table 2.1 is a list of proposed QCD sum rule model DA's along with the nonrelativistic and asymptotic DA's and the associated prediction for $\lambda_{J/\psi}$ made by each.

2.3 Angular Distribution of J/ψ and ψ' decays

The processes that contribute to the proton-antiproton-charmonium coupling are manifested in the polarization of the formed charmonium state. The polarization of charmonium states can be measured through the angular distribution of its decay

DA	$\lambda_{J/\psi}$
nonrelativistic	0.688
asymptotic	0.667
Chernyak and Zhitnitsky [31]	0.587
Chernyak, Ogloblin and Zhitnitsky [32]	0.587
King and Sachrajda [33]	0.591
Gari and Stefanis [34]	0.963
Stefanis and Bergmann [35]	0.689

Table 2.1: Predictions for $\lambda_{J/\psi}$ for various proposed hadronic distribution amplitudes.

products. In this section, the angular distribution if J/ψ and ψ' decays are calculated, and connection is made between the form of the angular distributions and the form factors that describe the charmonium production process.

2.3.1 Angular distribution of $\bar{p}p \to J/\psi(\psi') \to e^+e^-$

In the helicity formalism, the matrix element for the process $\bar{p}p \to J/\psi(\psi') \to e^+e^-$ can be expressed as

$$\mathcal{M}(\lambda_{\bar{p}}, \lambda_p, \lambda_{e^+}, \lambda_{e^-}) = \sum_{M_z} C_{M_z} D^{*(J_{J/\psi(\psi')})}_{\lambda_{\bar{p}}-\lambda_p, M_z}(0,0,0) B_{\lambda_{e^+}\lambda_{e^-}} D^{*(J_{J/\psi(\psi')})}_{M_z, \lambda_{e^+}-\lambda_{e^-}}(\phi, \theta, -\phi). \tag{2.7}$$

The helicity variables are defined in figure 2.3.1. C_{M_z} is the amplitude for production of a $J/\psi(\psi')$ with spin projection $J_z = M_z$ in $\bar{p}p$. $B_{\lambda_{e^+}\lambda_{e^-}}$ is the amplitude for the $J/\psi(\psi')$ to decay to e^+e^-. The first D function reduces to $\delta_{M_z,(\lambda_{\bar{p}}-\lambda_p)}$. The electron-positron helicities λ_{e^+} and λ_{e^-} obey the relation $\lambda_{ee} \equiv \lambda_{e^+} - \lambda_{e^-} = \pm 1$ in the limit of the negligible electron mass. Similarly, we define $\lambda_{\bar{p}p} \equiv \lambda_{\bar{p}} - \lambda_p$. These substitutions are made to simplify the notation only. Sums are made over the particle helicities. Summing over $\lambda_{\bar{p}} = \pm\frac{1}{2}$ and $\lambda_p = \pm\frac{1}{2}$ is equivalent to summing over $\lambda_{\bar{p}p} = +1, -1, 0, 0$. Applying these constraints to the matrix element gives

$$\mathcal{M}(\lambda_{\bar{p}p}, \lambda_{ee}) \;\propto\; D^{*(1)}_{\lambda_{\bar{p}p}, \lambda_{ee}}(\phi, \theta, -\phi) B_{\lambda_{ee}} C_{\lambda_{\bar{p}p}}. \tag{2.8}$$

For the general process $a \to b + c$ (or $b + c \to a$) described by helicity amplitude $A_{\lambda_b\lambda_c}$, parity conservation requires

$$A_{\lambda_b\lambda_c} = \eta_a\eta_b\eta_c(-1)^{S_b+S_c-S_a} A_{-\lambda_b-\lambda_c}. \tag{2.9}$$

η_a, η_b, and η_c are the parities of particles a, b, and c. For this case,

$$\begin{aligned} B_{\lambda_{ee}} &= (\eta_{J/\psi(\psi')})(\eta_{ee})(-1)^{S_{J/\psi}-S_{e^+}-S_{e^-}} B_{-\lambda_{ee}} &\Rightarrow B_1 = B_{-1} \\ C_{\lambda_{\bar{p}p}} &= (\eta_{\bar{p}p})(\eta_{J/\psi(\psi')})(-1)^{S_{\bar{p}}+S_p-S_{J/\psi(\psi')}} C_{-\lambda_{\bar{p}p}} &\Rightarrow C_1 = C_{-1}. \end{aligned} \tag{2.10}$$

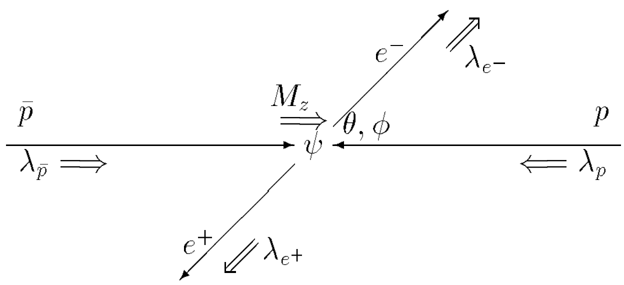

Figure 2.1: Helicity variables for $\bar{p}p \to J/\psi(\psi') \to e^+e^-$.

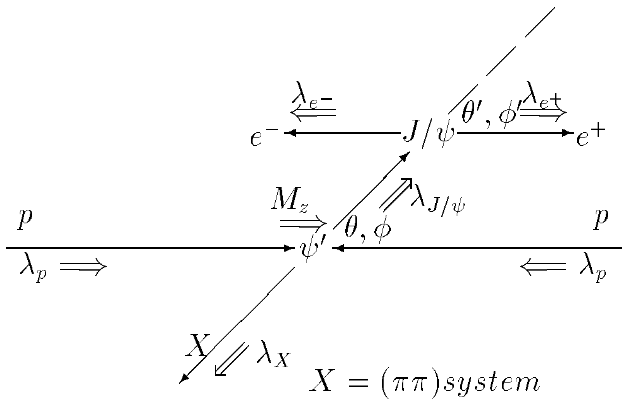

Figure 2.2: Helicity variables for $\bar{p}p \rightarrow \psi' \longrightarrow J/\psi\pi\pi$.

We now square the matrix element, average over initial helicity states and sum over final helicity states to get the form of the angular distribution.

$$\overline{|\mathcal{M}|^2} \propto 1 + \lambda cos^2\theta_e, \qquad \lambda = \frac{(C_1^2 - 2C_0^2)}{(C_1^2 + 2C_0^2)}. \tag{2.11}$$

Note that the value of λ is restricted to range from -1 to 1, and is entirely dependent on the $J/\psi(\psi')$ formation amplitudes C_0 and C_1.

2.3.2 Angular distribution of $\bar{p}p \rightarrow J/\psi\pi\pi \rightarrow e^+e^-\pi\pi$

The $J/\psi\pi\pi$ decay channel represents about 90% of the total inclusive decay width of ψ' to J/ψ. The variables used in this calculation are defined in figure 2.2.

As in the previous section, the general form of the matrix element is a function of the initial state helicities for the protons and the final state helicities for the electrons. The calculation is complicated by the addition of the sum over the J/ψ helicity states. The recoiling $\pi\pi$ system is assumed to have $J^P = 0^+$, and the $\psi' \rightarrow J/\psi\pi\pi$ decay is assumed to produce an isotropic J/ψ distribution. Studies of $\psi' \to J/\psi\pi\pi$ in high statistics experiments at e^+e^- colliders have shown that both of these assumptions are valid [36]. The isotropy of the $J/\psi\pi\pi$ decay is also clearly observable in this experiment, despite a relatively limited data sample.

The $\psi' \longrightarrow J/\psi\pi\pi$ process is assumed to occur via sequential two-body decays:

$$\psi' \to J/\psi X \to e^+e^-\pi\pi, \tag{2.12}$$

where $X = \pi\pi$ system. The general form for the matrix element is

$$\begin{aligned}
&\mathcal{M}(\lambda_{\bar{p}}, \lambda_p, \lambda_{e^+}, \lambda_{e^-}, \lambda_X) = \\
&\quad \sum_{\lambda_{J/\psi}, M_z} C_{M_z} D^{*(J_{\psi'})}_{\lambda_{\bar{p}}-\lambda_p, M_z}(0,0,0) A_{\lambda_{J/\psi}\lambda_X} D^{*(J_{\psi'})}_{M_z, \lambda_{J/\psi}-\lambda_X}(\phi, \theta, -\phi) \\
&\qquad \times B_{\lambda_{e^+}\lambda_{e^-}} D^{*(J_{J/\psi})}_{\lambda_{J/\psi}, \lambda_{e^+}-\lambda_{e^-}}(\phi', \theta', -\phi').
\end{aligned} \tag{2.13}$$

C_{M_z} is the amplitude for ψ' production in $\bar{p}p$, $A_{\lambda_{J/\psi}\lambda_X}$ is the amplitude for ψ' decay to $J/\psi(\pi\pi)$, and $B_{\lambda_{e^+}\lambda_{e^-}}$ is the amplitude for J/ψ decay into e^+e^-. The $\pi\pi$ system is assumed to have quantum numbers $J^P = 0^+$, which requires $\lambda_X = 0$. As in the previous calculation, the electron-positron helicities λ_{e^+} and λ_{e^-} obey the relation $\lambda_{ee} \equiv \lambda_{e^+} - \lambda_{e^-} = \pm 1$, and we define $\lambda_{\bar{p}p} \equiv \lambda_{\bar{p}} - \lambda_p = \pm 1, 0, 0$. The first D function reduces to $\delta_{M_z,(\lambda_{\bar{p}}-\lambda_p)}$. Applying these constraints to the matrix element gives

$$\begin{aligned}
\mathcal{M}(\lambda_{\bar{p}p}, \lambda_{ee}, \lambda_X) \quad \propto \quad & \sum_{\lambda_{J/\psi}, M_z} D^{*(1)}_{M_z, \lambda_{J/\psi}-\lambda_X}(\phi, \theta, -\phi) A_{\lambda_{J/\psi}\lambda_X} \\
& \times D^{*(1)}_{\lambda_{J/\psi}, \lambda_{ee}}(\phi', \theta', -\phi') B_{\lambda_{ee}} C_{M_z} \delta_{\lambda_{\bar{p}p}, M_z}
\end{aligned} \tag{2.14}$$

Parity conservation requires:

$$\begin{aligned}
A_{\lambda_{J/\psi}} &= (\eta_{\psi'})(\eta_{J/\psi})(\eta_X)(-1)^{S_{\psi'}-(S_{J/\psi}+S_X)} A_{-\lambda_{J/\psi}} && \Rightarrow A_1 = A_{-1}, \\
B_{\lambda_{ee}} &= (\eta_{J/\psi})(\eta_{ee})(-1)^{S_{J/\psi}-(S_{e^+}+S_{e^-})} B_{-\lambda_{ee}} && \Rightarrow B_1 = B_{-1}, \\
C_{M_z} &= (\eta_{\bar{p}p})(\eta_{\psi'})(-1)^{(S_{\bar{p}}+S_p)-S_{\psi'}} C_{-M_z} && \Rightarrow C_1 = C_{-1}.
\end{aligned} \tag{2.15}$$

The assumption that the $\pi\pi$ system has J=0 allows us to drop the λ_X subscript from the helicity amplitude for ψ' decay.

Summing over $\lambda_{J/\psi}$ and M_z and squaring the matrix element to gives the angular distribution. The result of the sum is

$$\begin{aligned}
&\mid \mathcal{M}(\lambda_{\bar{p}p}, \lambda_{ee}) \mid^2 \propto \\
&\quad \Big| e^{i(\lambda_{\bar{p}p}\phi - \phi)} d^{(1)}_{\lambda_{\bar{p}p}1}(\theta) A_1 e^{i(\phi' - \lambda_{ee}\phi')} d^{(1)}_{1\lambda_{ee}}(\theta') B_{\lambda_{ee}} C_{\lambda_{\bar{p}p}} \\
&\quad + e^{i(\lambda_{\bar{p}p}\phi)} d^{(1)}_{\lambda_{\bar{p}p}0}(\theta) A_0 e^{i(-\lambda_{ee}\phi')} d^{(1)}_{0\lambda_{ee}}(\theta') B_{\lambda_{ee}} C_{\lambda_{\bar{p}p}} \\
&\quad + e^{i(\lambda_{\bar{p}p}\phi + \phi)} d^{(1)}_{\lambda_{\bar{p}p}-1}(\theta) e^{i(-\phi' - \lambda_{ee}\phi')} d^{(1)}_{-1\lambda_{ee}}(\theta') B_{\lambda_{ee}} C_{\lambda_{\bar{p}p}} \Big|^2,
\end{aligned} \tag{2.16}$$

Where the $d^{(M_z)}_{\lambda_{\bar{p}p},\lambda_{J/\psi}}$ are the d functions [37]. Multiplying this expression out gives

$$\begin{aligned}
&\mid \mathcal{M}(\lambda_{\bar{p}p}, \lambda_{ee}) \mid^2 \propto \\
&\quad \left(d^{(1)}_{\lambda_{\bar{p}p}1}(\theta) d^{(1)}_{1\lambda ee}(\theta') A_1 B_{\lambda_{ee}} C_{\lambda_{\bar{p}p}}\right)^2 + \left(d^{(1)}_{\lambda_{\bar{p}p}0}(\theta) d^{(1)}_{0\lambda ee}(\theta') A_0 B_{\lambda_{ee}} C_{\lambda_{\bar{p}p}}\right)^2 \\
&\quad + \left(d^{(1)}_{\lambda_{\bar{p}p}-1}(\theta) A_1 d^{(1)}_{-1\lambda ee}(\theta') A_1 B_{\lambda_{ee}} C_{\lambda_{\bar{p}p}}\right)^2 \\
&\quad + e^{-i\phi} d^{(1)}_{\lambda_{\bar{p}p}1}(\theta) d^{(1)}_{\lambda_{\bar{p}p}0}(\theta) A_0 A_1 e^{i\phi'} d^{(1)}_{1\lambda_{ee}}(\theta') d^{(1)}_{0\lambda_{ee}}(\theta') B^2_{\lambda_{ee}} C^2_{\lambda_{\bar{p}p}} + c.c. \\
&\quad + e^{-i\phi} d^{(1)}_{\lambda_{\bar{p}p}0}(\theta) d^{(1)}_{\lambda_{\bar{p}p}-1}(\theta) A_0 A_1 e^{i\phi'} d^{(1)}_{-1\lambda_{ee}}(\theta') d^{(1)}_{0\lambda_{ee}}(\theta') B^2_{\lambda_{ee}} C^2_{\lambda_{\bar{p}p}} + c.c. \\
&\quad + e^{-2i\phi} d^{(1)}_{\lambda_{\bar{p}p}1}(\theta) d^{(1)}_{\lambda_{\bar{p}p}-1}(\theta) A_1^2 e^{2i\phi'} d^{(1)}_{1\lambda_{ee}}(\theta') d^{(1)}_{-1\lambda_{ee}}(\theta') B^2_{\lambda_{ee}} C^2_{\lambda_{\bar{p}p}} + c.c.
\end{aligned} \tag{2.17}$$

The J/ψ decay helicity amplitude B_1^2 multiplies each term and therefore is dropped. Averaging over initial states and summing over final states reduces the matrix element to

$$\begin{aligned}
\overline{|\mathcal{M}|^2} \quad \propto \quad & \frac{A_1^2}{2}\left(1 + cos^2\theta'\right)\left[C_1^2\left(1 + cos^2\theta\right) + 2C_0^2 sin^2\theta\right] \\
& + A_0^2 sin^2\theta' \left[2C_0^2 cos^2\theta + C_1^2 sin^2\theta\right] \\
& - 2A_0 A_1 cos(\phi - \phi') \left[cos\theta sin\theta cos\theta' sin\theta'\right]\left[C_1^2 - 2C_0^2\right] \\
& + \frac{A_1^2}{2} cos(2\phi - 2\phi')\left[sin^2\theta sin^2\theta'\right]\left[C_1^2 - 2C_0^2\right].
\end{aligned} \tag{2.18}$$

As we are interested only in the form of the matrix element and not the absolute magnitude, the ratio of the helicity amplitudes is sufficient to describe the angular distribution. This reduces the number of free parameters in this calculation to 2. To reduce the number of free parameters to 1, we exploit the observation that the $\psi' \to J/\psi X$ decay has an isotropic angular distribution in e^+e^- experiments. This constraint is applied by integrating equation 2.19 over the primed variables to get the angular distribution of the ψ' decay and then choosing values for A_1 and A_0 to eliminate angular dependence from the ψ' decay. Integrating over θ' and ϕ' gives

$$\overline{|\mathcal{M}|^2} \propto \left(A_1^2 - A_0^2\right)\left(C_1^2 - 2C_0^2\right)cos^2\theta + \left[A_1^2\left(C_1^2 + 2C_0^2\right) + A_0^2 C_1^2\right]. \tag{2.19}$$

Therefore, observation of an isotropic J/ψ distribution implies $A_1 = \pm A_0$. Inserting this result back into equation 2.19 yields

$$\begin{aligned}
\overline{|\mathcal{M}|^2} \;\; \propto \;\; & \left(1 + cos^2\theta'\right)\left[C_1^2\left(1 + cos^2\theta\right) + 2C_0^2 sin^2\theta\right] \\
+ \;\; & 2sin^2\theta'\left[2C_0^2 cos^2\theta + C_1^2 sin^2\theta\right] \\
\mp \;\; & 4cos\left(\phi - \phi'\right)\left[cos\theta sin\theta cos\theta' sin\theta'\right]\left[C_1^2 - 2C_0^2\right] \\
+ \;\; & cos\left(2\phi - 2\phi'\right)\left[sin^2\theta sin^2\theta'\right]\left[C_1^2 - 2C_0^2\right].
\end{aligned} \tag{2.20}$$

The angular distribution of the electrons can be determined by integrating over θ, ϕ while holding the electron decay direction constant. This calculation is complicated by the fact that for fixed electron direction in the CMS frame θ', ϕ' are functions of θ, ϕ. To simplify the calculation, a new set of variables is introduced to replace θ', ϕ': θ_e, ϕ_e, which describe the electron direction in the center of mass frame with respect to the $\bar{p}$ direction. θ_e, ϕ_e are not functions of θ, ϕ. This allows integration over θ, ϕ holding θ_e, ϕ_e constant. To write the angular distribution in terms of $\theta, \phi, \theta_e, \phi_e$ we must substitute expressions for the primed angles in terms of our set of C.M. frame variables. By applying Euler angle rotations we find the following relationships between θ', ϕ' and the lab frame variables $\theta, \phi, \theta_e, \phi_e$. Neglecting the boost of the J/ψ with respect to the center of mass frame, θ',ϕ' can be expressed in terms of θ,ϕ,θ_e, ϕ_e through the relations:

$$\begin{aligned} sin\theta' cos\phi' &= \left(cos\theta cos^2\phi + sin^2\phi\right) sin\theta_e cos\phi_e \\ &+ (cos\theta - 1)\, sin\phi cos\phi sin\theta_e sin\phi_e \\ &- sin\theta cos\phi cos\theta_e, \end{aligned} \tag{2.21}$$

$$\begin{aligned} sin\theta' sin\phi' &= \left(cos\theta sin^2\phi + cos^2\phi\right) sin\theta_e sin\phi_e \\ &+ (cos\theta - 1)\, sin\phi cos\phi sin\theta_e cos\phi_e \\ &- sin\theta sin\phi cos\theta_e, \end{aligned} \tag{2.22}$$

$$\begin{aligned} cos\theta' &= sin\theta cos\phi sin\theta_e cos\phi_e \\ &+ sin\theta sin\phi sin\theta_e sin\phi_e \\ &+ cos\theta cos\theta_e. \end{aligned} \tag{2.23}$$

Using these expressions, $\overline{|\mathcal{M}|^2}$ is rewritten as a function of $\theta, \phi, \theta_e, \phi_e$. We are now free to integrate over θ and ϕ the get the angular distribution of the electrons. The integration yields

$$\begin{aligned} \overline{|\mathcal{M}|^2} &\propto \left[3cos^2\theta_e + 19\right] C_1^2 + \left[-3cos^2\theta_e + 11\right] 2C_0^2 \\ &+ \left[6cos^2\theta_e - 2\right] \left(C_1^2 - 2C_0^2\right) \pm \left[6cos^2\theta_e - 2\right] \left(C_1^2 - 2C_0^2\right). \end{aligned} \tag{2.24}$$

For the 2 cases, $A_1 = +A_0$ and $A_1 = -A_0$, the electron angular distribution reduces to

$$\overline{|\mathcal{M}|^2} \propto \quad 1 + \lambda cos^2\theta_e, \quad A_1 = +A_0, \tag{2.25}$$

$$\overline{|\mathcal{M}|^2} \propto \quad (4\lambda + 15) + 3\lambda cos^2\theta_e, \quad A_1 = -A_0. \tag{2.26}$$

As before, in each case $\lambda = \frac{C_1^2 - 2C_0^2}{C_1^2 + 2C_0^2}$. Both solutions equally well satisfy initial conditions of the calculation. However, they predict distinctly different angular distributions. For example, when $\lambda = 1$ ($\lambda = 1$ if the ψ' resonance were formed in an e^+e^- annihilation) $A_1 = A_0$ yields a $1 + cos^2\theta_e$ distribution, whereas the alternate solution, with $A_1 = -A_0$, predicts a $1 + \frac{3}{19}cos^2\theta_e$ distribution. Clearly, only one solution is correct. Observations by experiments at e^+e^- colliders rule out the $A_1 = -A_0$ solution. One might expect that the $A_1 = A_0$ solution is correct. The $\pi\pi$ system carries no internal spin ($J_X = 0$) and the $\psi' \rightarrow J/\psi X$ decay is isotopic, which suggests an $l = 0$ decay. If the decay is purely s-wave, the J/ψ carries away the spin of the ψ', and decays with the same angular distribution as $\psi' \rightarrow e^+e^-$, $1 + \lambda cos^2\theta_e$. The origin of the false solution is examined in section 1.4.4.

2.3.3 Angular distribution of $\bar{p}p \rightarrow J/\psi\eta \rightarrow e^+e^-\eta$

The $\psi' \rightarrow J/\psi\eta$ decays are of limited importance in determining the angular distribution of inclusive ψ' decays, because they only represent about 5% of the total inclusive decay fraction. However, the result is important in studying the exclusive $J/\psi\eta$ channel. The variables used in this calculation are defined in figure 2.3

The derivation of the angular distribution for this channel is similar to the $J/\psi\pi\pi$ channel discussed in the previous section. The only difference is that the $\eta(\pi)$ has odd parity, whereas the $\pi\pi$ system in the previous calculation is assumed to have even parity. This difference changes the constraints on the relations between the helicity amplitudes for the ψ' decay from $A_1 = A_{-1}$ to $A_1 = -A_{-1}$, and provides the additional constraint that $A_0 = 0$. Applying these results to equation 2.13 , averaging over initial state helicities and summing over final state helicities gives

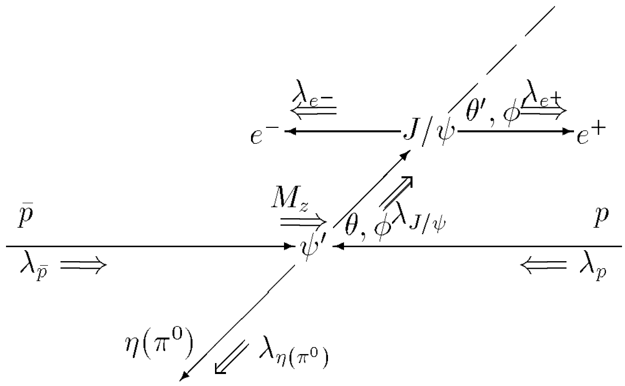

Figure 2.3: Helicity variables for $\bar{p}p \to \psi' \to J/\psi\eta(\pi^0)$.

$$\overline{|\mathcal{M}|^2} \propto \left(1 + cos^2\theta'\right)\left[C_1^2\left(1 + cos^2\theta\right) + 2C_0^2 sin^2\theta\right] - cos(2\phi - 2\phi')\left[sin^2\theta sin^2\theta'\right]\left[C_1^2 - 2C_0^2\right]. \quad (2.27)$$

As before the expressions involving primed variables are rewritten in terms of $\theta, \phi, \theta_e, \phi_e$ and integrated over θ and ϕ to get the form of the electron angular distribution in the center of mass frame. The angular distribution for the electrons in the center of mass frame is

$$\overline{|\mathcal{M}|^2} \propto (5\lambda + 4) - 4\lambda cos^2\theta_e. \quad (2.28)$$

Integration of equation 2.27 over the primed J/ψ decay angles gives the angular distribution of the $\psi' \to J/\psi\eta$ decay. The integration yields

$$\overline{|\mathcal{M}|^2} \propto 1 + \lambda cos^2\theta. \quad (2.29)$$

This result is strikingly different from the result for the $J/\psi\pi\pi$ decay of the ψ' where, based on observation, the J/ψ distribution was explicitly assumed to be isotropic.

2.3.4 Interpretation of extra solution for $\psi' \to J/\psi\pi\pi$

An alternate method of calculating the angular distribution of the process $\bar{p}p \to \psi' \to J/\psi\pi\pi$ is to calculate directly the angular distributions for the allowed orbital angular momenta $l = 0$ (s-wave) and $l = 2$ (d-wave) decays of ψ' to $J/\psi\pi\pi$. Orbital angular momentum greater than $l = 2$ is prohibited by conservation of angular momentum. The $l = 1$ decay is excluded because it violates parity. As before we will assume that the $\pi\pi$ system has spin 0 and the decay proceeds as a series of 2-body decays: $\psi' \to J/\psi X$, $J/\psi \to e^+e^-$, and $X \to \pi\pi$.

Consider the case where the ψ' decay is purely s-wave. The absence of orbital angular momentum demands that the J/ψ carry away the polarization of the ψ'. In this case, the electrons from the J/ψ decay will have the same angular distribution as in the ψ' decay to e^+e^-, $1+\lambda cos^2\theta_e$. This is the $A_1 = A_0$ result from the helicity formalism solution.

Now, consider a coherent superposition of $l = 2$ and $l = 0$. Denote the $J/\psi X$ state arising from the decay of a ψ' with spin projection J_z and the spin state of the J/ψ by χ_m, where $m = S_z$. The normalized superposition of $l = 0$ and $l = 2$ decays is expressed as

$$|1\ J_z> = \frac{1}{\sqrt{1+a^2}}\left(a|1J_z>_{l=0} + |1J_z>_{l=2}\right). \tag{2.30}$$

The final states corresponding to the values $J_z = +1, 0, -1$ are expressed as

$$\begin{aligned}
|1\ 1> &= \frac{1}{\sqrt{1+a^2}}\left(\sqrt{\frac{3}{5}}Y_2^2\chi_{-1} - \sqrt{\frac{3}{10}}Y_2^1\chi_0 + (\sqrt{\frac{1}{10}}Y_2^1 + aY_0^0)\chi_1\right), & (2.31)\\
|1\ 0> &= \frac{1}{\sqrt{1+a^2}}\left(\sqrt{\frac{3}{10}}Y_2^1\chi_{-1} - (\sqrt{\frac{2}{5}}Y_2^0 + aY_0^0)\chi_0 - \sqrt{\frac{3}{10}}Y_2^1\chi_1\right), & (2.32)\\
|1\ {-1}> &= \frac{1}{\sqrt{1+a^2}}\left((\sqrt{\frac{1}{10}}Y_2^0 + aY_0^0)\chi_{-1} + \sqrt{\frac{3}{10}}Y_2^1\chi_0 + \sqrt{\frac{3}{5}}Y_2^2\chi_1\right). & (2.33)
\end{aligned}$$

Squaring these expressions gives the angular distribution for the decay of ψ' for the 3 initial state polarizations. The angular distribution of the J/ψ for ψ' initial states $|1\ 1>$ and $|1\ {-1}>$ is

$$\frac{1}{16\pi(1+a^2)}\left\{(5-2\sqrt{2}a+4a^2)+(-3+6\sqrt{2}a)cos^2\theta)\right\}, \tag{2.34}$$

and ψ' spin state $|1\ 0>$ decays with angular distribution

$$\frac{1}{8\pi(1+a^2)}\left\{(1+2\sqrt{2}a+2a^2)+(3-6\sqrt{2}a)cos^2\theta)\right\}. \tag{2.35}$$

As in the helicity analysis, θ is the the decay angle of the J/ψ in the ψ' center of mass frame. In each case the ψ' decay is isotropic for $a^2 = \frac{1}{8}$. This solution satisfies the conditions imposed in the helicity formalism calculation equally well as the pure s-wave case. However, the e^+e^- angular distribution is quite different in the pure s-wave calculation. The electron angular distribution can be determined by summing the probabilities for each J/ψ spin state, χ_m. For the three ψ' spin configurations, the occupation probabilities of the three J/ψ spin states are

$$|1\,1>:\ P(\chi_{-1}) = \frac{3}{5(1+a^2)},\quad P(\chi_0) = \frac{3}{10(1+a^2)},\quad P(\chi_1) = \frac{\frac{1}{10}+a^2}{(1+a^2)} \tag{2.36}$$

$$|1\,0>:\ P(\chi_{-1}) = \frac{3}{10(1+a^2)},\quad P(\chi_0) = \frac{\frac{2}{5}+a^2}{(1+a^2)},\quad P(\chi_1) = \frac{3}{10(1+a^2)} \tag{2.37}$$

$$|1\,-1>:\ P(\chi_{-1}) = \frac{\frac{1}{10}+a^2}{(1+a^2)},\quad P(\chi_0) = \frac{3}{10(1+a^2)},\quad P(\chi_1) = \frac{3}{5(1+a^2)} \tag{2.38}$$

For J/ψ polarizations χ_{-1} and χ_1 the electron angular distribution is $\frac{1}{2}(1+cos^2\theta_e)$, and the angular distribution of electrons decaying from the χ_0 polarization state is $(1 - cos^2\theta_e)$. Using the notation from the previous section, the ψ' spin states $|1\,1>$ and $|1\,-1>$ are equally populated and the state $|1\,0>$ is produced with frequency $\frac{1-\lambda}{1+\lambda}|1\,1>$. Summing the contributions for from each polarization state, and setting $a^2 = \frac{1}{8}$ to demand J/ψ isotropy yields electron angular distribution

$$(4\lambda + 15) + 3\lambda cos^2\theta_e. \tag{2.39}$$

This is precisely the result obtained for the $A_1 = -A_0$ helicity formalism solution. This solution is a unique coherent superposition of $l = 2$ and $l = 0$ (predominantly $l = 2$) ψ' decays that produces an isotropic $\psi' \to J/\psi X$ decay angular distribution.

Chapter 3

Experimental Apparatus

The E760 experiment was conducted at the Fermi National Accelerator Laboratory (FNAL). The E760 detector is a non-magnetic spectrometer optimized for the detection of high mass 2-body charmonium decays to electromagnetic final states. The apparatus was located in the Fermilab Antiproton Accumulator facility.

3.1 Fermi National Accelerator Laboratory

FNAL was designed and constructed to provide high energy proton beams for fixed target experiments. Expansion has seen the installation of an antiproton production and storage facility and the construction of two large collider experiments. Fermilab maintains the world's highest energy hadron collider facilities and supports a broad experimental and theoretical research program. Figure 3.1 is a diagram of the accelerator beam lines.

3.2 Antiproton Source

The Antiproton Source[39] was designed for production and storage of antiprotons for use by the high energy collider program. The facility was modified to allow

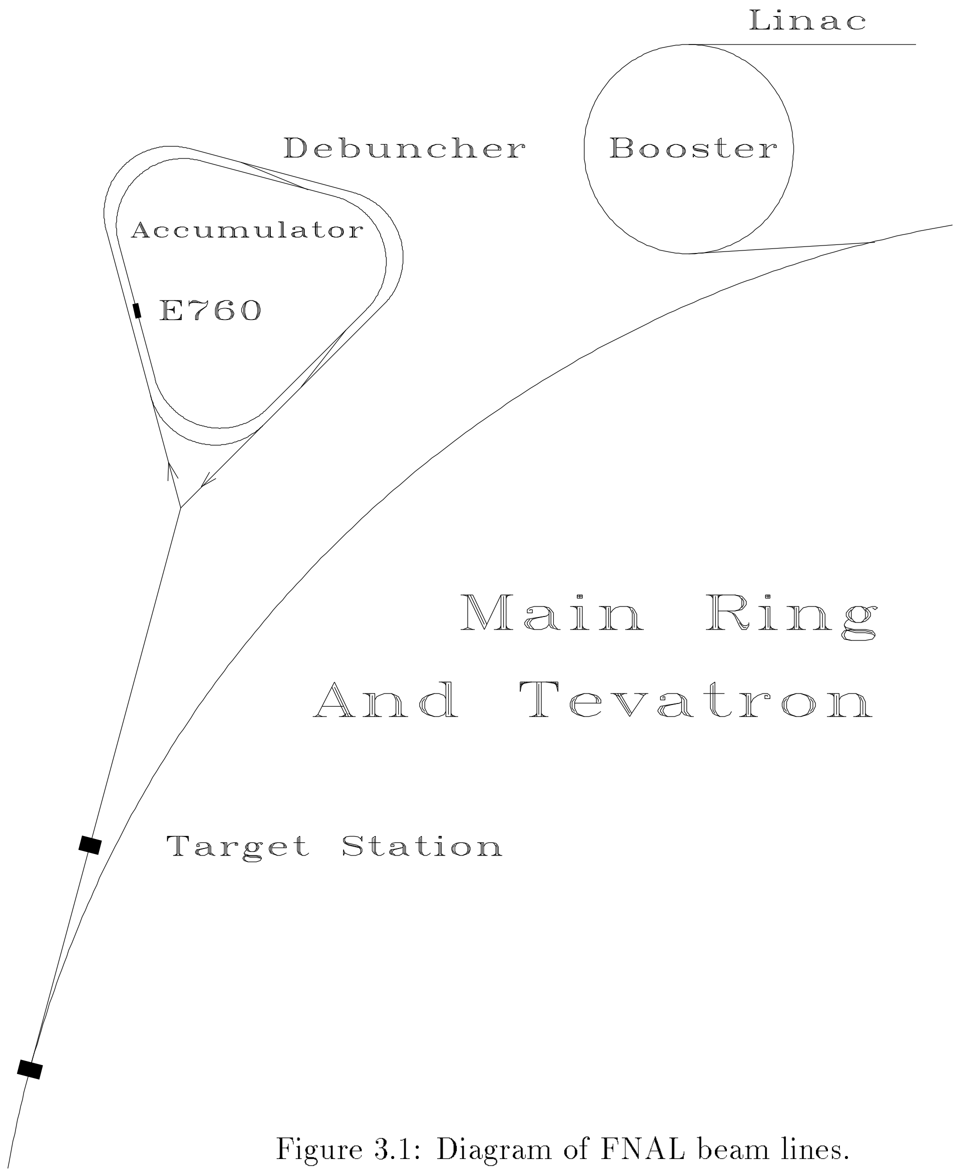

Figure 3.1: Diagram of FNAL beam lines.

deceleration and cooling of the direct current $\bar{p}$ beam for experiment E760.

The process of producing antiprotons begins with a multistage process of producing a high energy proton beam. H^- ions are accelerated to a kinetic energy of 750 keV with a Cockroft-Walton accelerator. The ions are then injected into a linear accelerator where their kinetic energy is brought to 200 MeV. The H^- are then passed through a carbon foil where the electrons are stripped away and the proton is transported to the Booster. The Booster is a proton synchrotron with circumference of 500m. In the Booster the protons are accelerated to 8 GeV and injected into the Main Ring. The Main Ring synchrotron accelerates the protons to 120 GeV.

Antiprotons are produced by extracting bunches of 120 GeV protons from the Main Ring which strike a tungsten/rhenium target. Antiprotons produced in interactions with the target are focused with a lithium lens and transported to the Debuncher. The Debuncher narrows the energy distribution of the antiprotons and broadens the bunch length. The transverse emitence, the phase space area of the beam in the transverse direction, of the beam is also reduced prior to injection into the Accumulator. The Accumulator receives pulses of antiprotons from the Debuncher. The antiprotons are stochastically cooled to the core orbit where they are stored at a total momentum of 8.9 GeV. During the course of this experiment, "stacks" of antiprotons were collected in the accumulator as large as 40 mA or 4×10^{11} antiprotons.

As originally designed, antiprotons are stored in the Accumulator until they are extracted to the Main Ring, accelerated, and injected into the Tevatron for use by colliding beam experiments. Modifications were made in the facility to allow for the deceleration of the beam to energies appropriate for resonant production of charmonium states. The Accumulator is capable of reducing the beam momentum as low as 3.5 GeV/c. This allows access to all charmonium states below the $D\bar{D}$ threshold. After $\bar{p}$ accumulation is complete, the beam is stochastically cooled and decelerated,

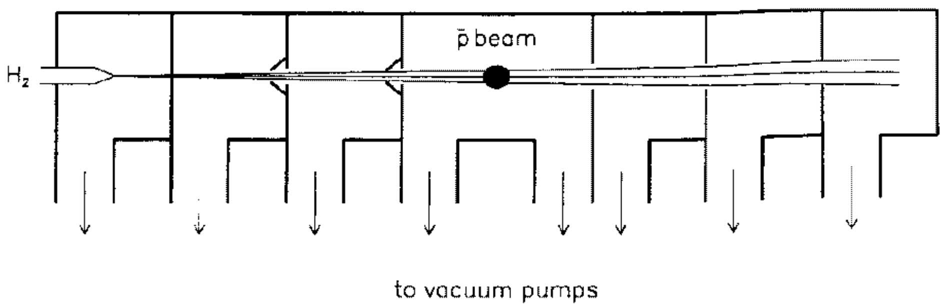

Figure 3.2: Diagram of E760 hydrogen gas jet target.

at about 20 MeV/c per second, to the desired energy. After deceleration and additional stochastic cooling, the beam has an energy spread of about $\frac{\sigma_p}{p} \approx 2 \times 10^{-4}$ and a transverse RMS radius of $\approx 1.2mm$.

3.3 H_2 Gas Jet Target

A hydrogen gas jet target [41] was constructed to provide a high density proton target for the circulating $\bar{p}$ beam. Molecular hydrogen was cooled to liquid nitrogen temperature and injected from a nozzle into the Accumulator vacuum system. A series of "skimmers" kept the jet narrow as it traversed a series of vacuum chambers. In the interaction region the target size was approximately 1 cm^3. A series of vacuum pumps continuously removed the extraneous hydrogen. With the gas jet on, the $\bar{p}$ lifetime ranged from 30-60 hours. Figure 3.3 is a diagram of the gas jet target system.

3.4 Luminosity Monitor

Luminosity measurements for E760 were provided by a high-resolution silicon detector[42] positioned 147 cm below the target region. The 0.5 mm thick instrument had 1 cm $\times$ 5 cm active area and was positioned at an angle of 86.5^o with respect to the $\bar{p}$ direction. Protons with kinetic energy less that 8 MeV will stop in the detector. By utilizing existing measurements of the forward elastic scattering cross section, the Luminosity $\mathcal{L}$ is related to the counts N by

$$\int \mathcal{L} \lceil \sqcup = \frac{N}{\int \frac{d\sigma_{elastic}}{d\Omega} d\Omega}. \tag{3.1}$$

Although the controls for the luminosity monitor were separate from those for the data collection for E760, luminosity runs and data runs were coordinated. Sufficient data were collected in each luminosity run (1-2 hours) to guarantee a negligible ($\approx 0.1\%$) contribution from counting statistics to the measurement error. A systematic error of 2.2% in the absolute luminosity measurement was due to uncertainty in the detector solid angle and the world data for the elastic scattering cross section.

3.5 E760 Detector

The E760 detector was designed for the detection of high invariant mass electromagnetic decays of charmonium resonances, while rejecting large hadronic backgrounds. The detector has full azimuthal coverage and covers laboratory polar angles between 2^o and 70^o. An array of hodoscopes were used for triggering. A threshold gas Čerenkov chamber was employed to identify electrons. Two calorimeters were used to measure the energies of electrons and photons. Figure 3.3 is a diagram of the E760 detector.

3.5.1 Hodoscopes

Three hodoscope arrays, constructed from NE102 plastic scintillator, were used for triggering and tracking. Closest to the interaction region was hodoscope H1. H1 was

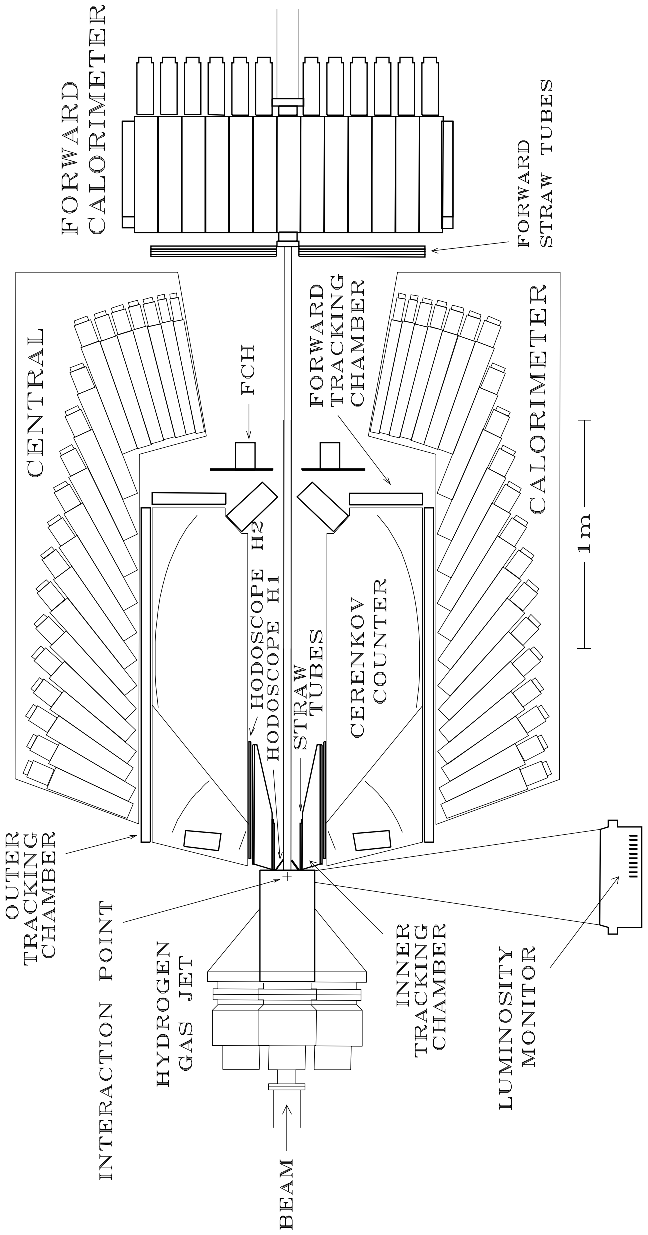

Figure 3.3: E760 Detector.

constructed from eight 2 mm thick azimuthally segmented elements, and positioned immediately outside the 0.2 mm thick stainless steel beam pipe. H1 covers lab polar angles $9^o < \theta_{lab} < 65^o$, and was tapered inward so that tracks of all angles impact the detector approximately perpendicular to its surface.

Hodoscope H2 was constructed of thirty-two 4 mm thick elements. Like H1, H2 was segmented azimuthally and has full azimuthal coverage. H2 is positioned 17 cm from the beam and covers laboratory polar angles $12^o < \theta_{lab} < 65^o$.

The forward charged veto (FCV) covers the polar angle region $2^o < \theta_{lab} < 9^o$. FCV was constructed from eight pie shaped paddles positioned perpendicular to the beam line.

H1 and H2 were used by the charged hardware trigger. The H1 and FCV hodoscopes were employed by the neutral triggers to reject events with charged tracks. In addition to its use in the hardware trigger, the pulse height from H2 was used offline to separate single charged tracks from Dalitz decays and photon conversions.

3.5.2 Charged Particle Tracking

A series of charged particle tracking detectors provided measurement of θ_{lab} and ϕ_{lab} for electrons and pions. In the barrel portion of the detector, working from the beam line outward, a straw chamber[43], a radial projection chamber (RPC)[44] a multi-wire proportional chamber (MWPC) and an outer tracking chamber made from Iarocci tubes, or limited streamer tubes (LST), provide charged particle tracking. In the forward region, a three plane multi-wire proportional chamber positioned perpendicular to the beam provided charged tracking coverage. Downstream of the barrel portion of the detector, prior to the forward calorimeter, a three plane straw chamber (FSTR) provied charged particle tracking in the forward region.

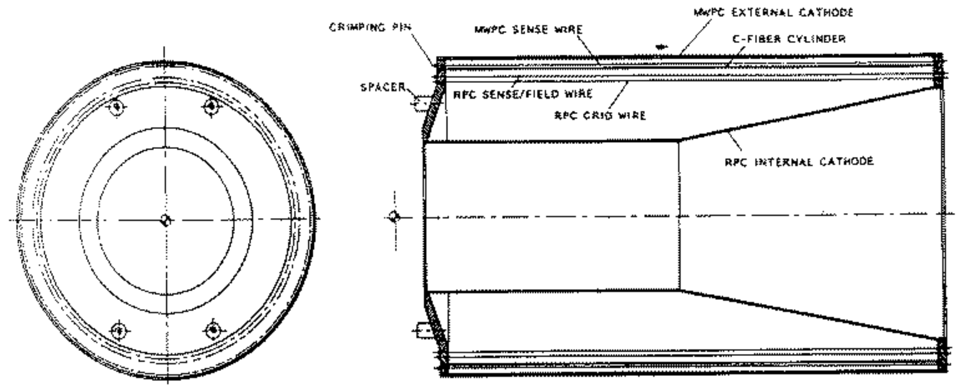

Figure 3.4: MWPC and RPC chamber diagram.

The straw chamber was located immediately outside hodoscope H1. The chamber was made up of two layers of 22 cm long mylar straws positioned 5.52 cm and 6.35 cm from the beam line. A 25 μm diameter wire runs the length of each straw and an Ar-CO_2-CH_4 gas mixture is continuously flowed through the chamber. A resolution of 200 μm in azimuthal track position is achieved by analysis of drift times and a z coordinate resolution of 3 mm was obtained from charge division.

Located between the straws and hodoscope H2 was a single chamber containing both the RPC and the MWPC. The RPC contains 80 sense wires, 20μm in diameter, and 80 field wires, 100 μm in diameter. The sense wires are made of a Fe-Ni-Cr alloy with a resistance of 3300 $\frac{\Omega}{m}$. The multiplication region is separated from the drift volume by a cylindrical grid of 240 100μm wires kept at a lower voltage than the field wires. The cylindrical MWPC is 10 mm thick and contains 320 gold-plated tungsten sense wires, 20μm in diameter. Four MWPC wires cover a single RPC cell. The MWPC removes the left-right ambiguity from the RPC. The RPC provided both tracking and $\frac{dE}{dX}$ data. Figures 3.4 is a diagram of the chamber. Figure 3.5 is a cross section of a drift cell.

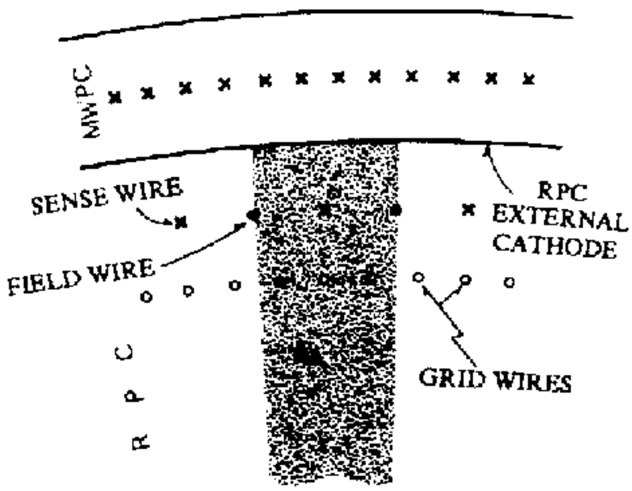

Figure 3.5: Drift cell cross section.

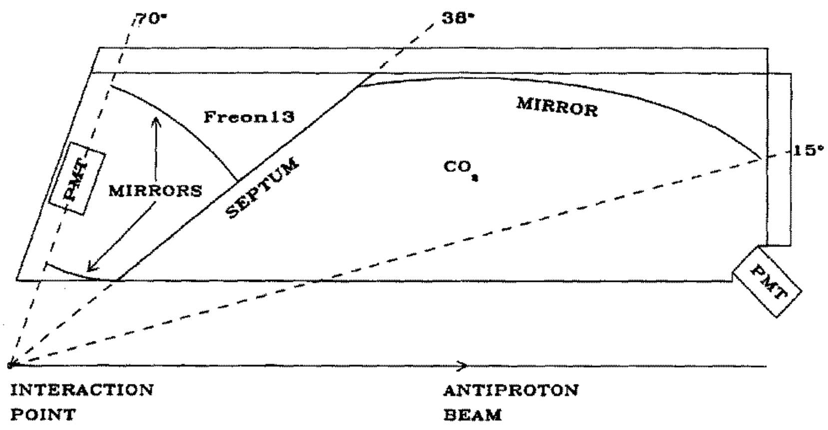

Figure 3.6: Černekov Counter.

3.5.3 Čerenkov Counter

A threshold Čerenkov [45] counter was used for electron/pion separation and triggering. The chamber was segmented into eight azimuthal sectors each containing an independent optical system. An aluminum foil septum divided each sector into a small angle cell ($15^o < \theta < 38^o$) and a large angle cell ($38^o < \theta < 70^o$). The counter was operated at atmospheric pressure with CO_2 in the small angle cell and Freon 13 in the large angle cell. The threshold for Čerenkov light production by pions in the small angle cell was 4.9 GeV/c and 3.7 GeV/c in the large angle cell. Light produced by electrons from the target is reflected by mirrors to 16 photomultiplier tubes located outside the detector's active volume. Figure 3.6 is a diagram of the Čerenkov counter.

3.5.4 Central Calorimeter

The central calorimeter (CCAL) [46] was the primary detector system in the E760 experiment. The CCAL provided energy measurements for electrons and photons as well as measurements of θ and ϕ that rivaled the resolution of the tracking chambers. In addition, the CCAL signals were used in all physics triggers.

The CCAL was designed to distinguish isolated electron and photon showers from π^o decays to two photons. π^0s that decay symmetrically (both photons of equal energy) can produce showers that overlap and can be misidentified as single photon showers if the detector were too coarsely segmented. The granularity of the detector had to be sufficient to recognize such decays. Asymmetric π^0 decays can also mimic single photon showers, if the lower energy photon from a π^0 decay is below the detector threshold. To control these backgrounds a design energy threshold of 50 MeV with an efficiency of 95% was specified. Lead glass was chosen as the detection material because of its low cost, excelent energy resolution and resistance to radiation damage. High energy electrons and photons impacting lead glass produced cascades of secondary electrons and photons called "showers". Čerenkov light emited by electrons in a shower is detected and used to estimate the energy and impact position of the showering particle.

The CCAL consisted of 1280 lead glass blocks, each block pointing toward the gas-jet target. The detector was constructed from 64 identical wedges that provided complete azimuthal coverage. Each wedge contained 20 uniquely shaped blocks that cover $11^o < \theta < 70^o$. Figure 3.7 is a diagram of a wedge assembly. The block were shaped as erect pyramidal frustra with trapezoidal bases. The dimensions and positions of the 20 block shapes are given in table 3.1. F2 lead glass was used because of its superior light production and transmission qualities. F2 lead glass has a density of 3.61 $\frac{g}{cm^3}$, a radiation length of 3.141 cm and a refractive index of 1.651. Each wedge is independent mechanically and electrically. Inside each wedge, the 20 blocks are separated by 0.254 mm stainless steel fins. Structural support was provided by 0.735 mm stainless steel skins that enclosed the counters. Photomultiplier tubes were attached to each of the blocks. Four models of Hamamatsu PMTs (R3036-02,R3345-02,R2154-04,R580-13), ranging in size from 1.5 in. to 3.0 in., were used.

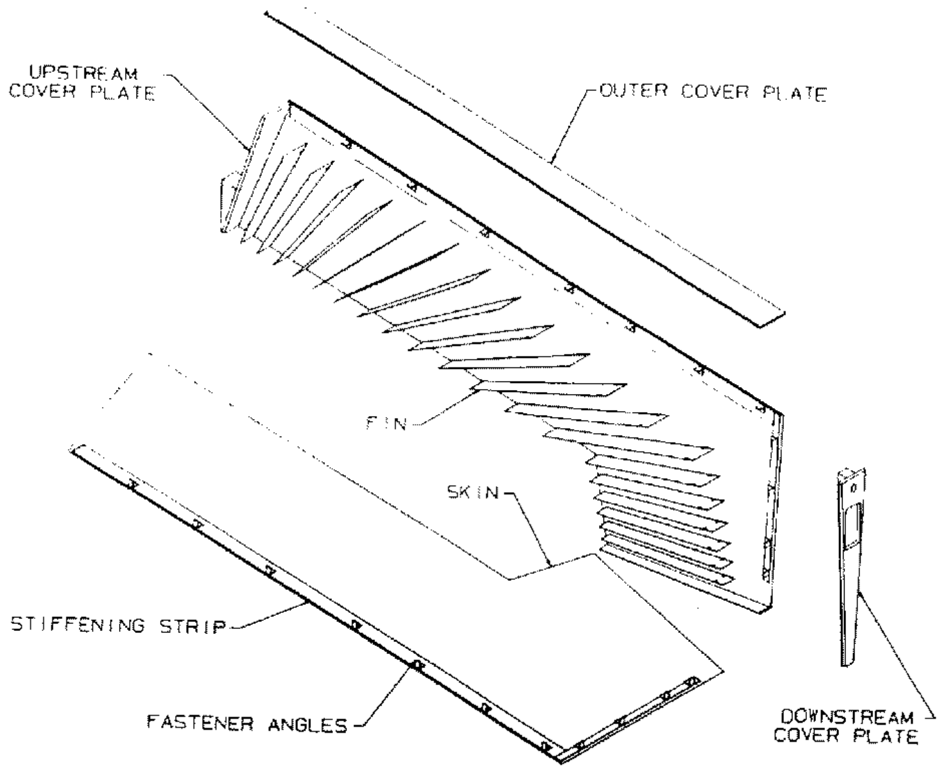

Figure 3.7: CCAL wedge assembly.

Block number	Length (L_R units)	$\Delta\theta$ (deg)	Distance from target (cm)	Fractional PMT coverage
1	12.03	5.226	72.44	0.473
2	12.30	5.031	75.87	0.475
3	12.70	4.803	80.07	0.476
4	13.21	4.552	85.08	0.478
5	13.86	4.284	90.96	0.479
6	14.65	4.007	97.79	0.481
7	15.59	3.728	105.62	0.482
8	15.92	3.451	114.54	0.497
9	15.92	3.183	124.66	0.520
10	15.92	2.925	136.07	0.544
11	15.92	2.679	148.89	0.568
12	15.92	2.449	163.26	0.593
13	15.92	2.233	179.34	0.617
14	15.92	2.033	197.28	0.641
15	15.92	1.848	197.29	0.546
16	15.92	1.678	197.29	0.664
17	15.92	1.522	197.30	0.527
18	15.92	1.380	197.30	0.644
19	15.92	1.250	197.30	0.443
20	15.92	1.131	197.30	0.543

Table 3.1: Dimensions and positions of lead glass blocks.

Discussions of the CCAL event reconstruction and calibration are presented in sections 8 and 9 of this chapter.

3.5.5 Forward Calorimeter

The forward calorimeter (FCAL) [47] consists of 144 lead-scintillator sandwich modules. The modules are arranged in a 13×13 array, perpendicular to the beam axis, with 6 modules removed from each corner and the center module removed to

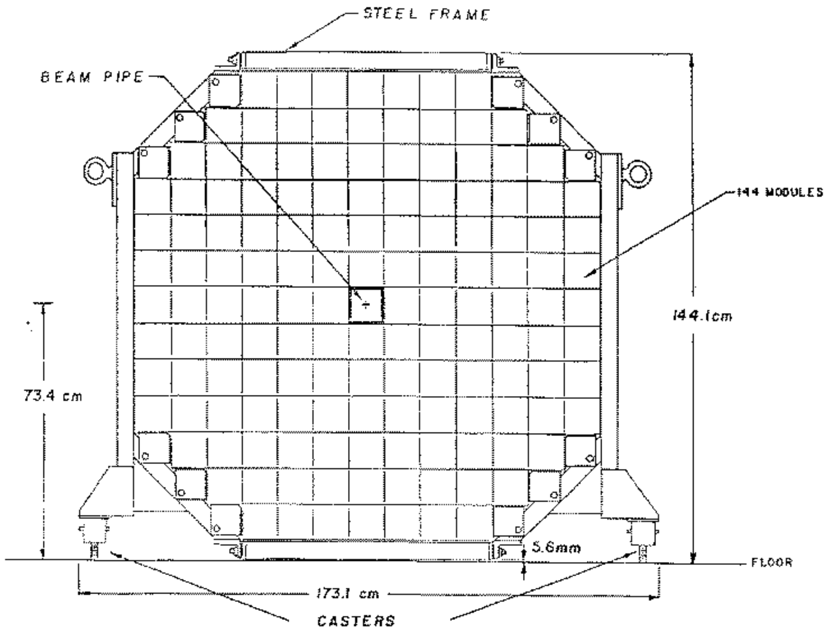

Figure 3.8: Forward Calorimeter.

make room for the beam pipe. The detector was located 340 cm downstream from the target. The FCAL covers polar angles $2^o < \theta < 12^o$. Each 10 cm $\times$ 10 cm module consists of 148 layers of alternating lead and plastic scintillator. Light from the scintillators was collected by a wavelength shifter plate along one side of each module. The wavelength shifter plate was attached to a light guide that transmits the light to a PMT. The energy resolution of the FCAL was $\frac{\sigma_E}{E} = \frac{19\%}{\sqrt{E}}$. The spatial resolution was $\sigma_x = \sigma_y = 3$ cm at the face of detector. Figure 3.8 and 3.9 are diagrams of the FCAL and an FCAL module assembly.

3.6 Data Acquisition System

The E760 data acquisition system was required to separate charmonium decay candidates from a large $\bar{p}p$ direct annihilation background. Annihilation rates within

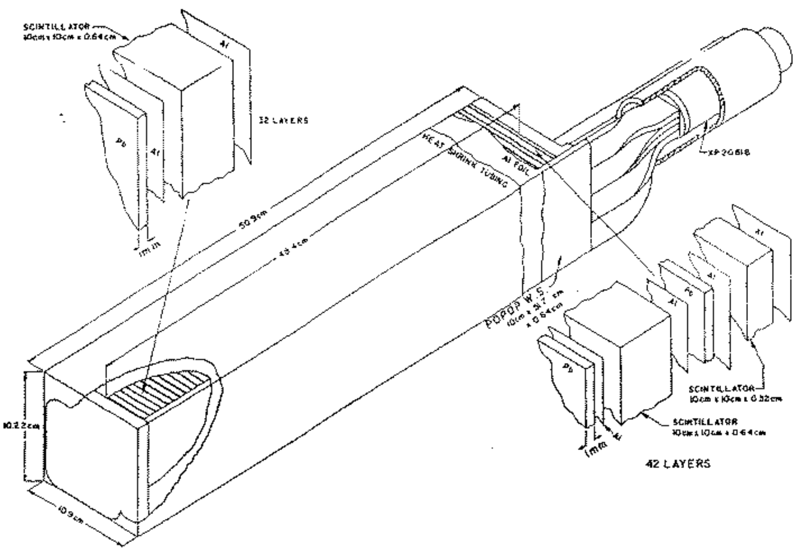

Figure 3.9: FCAL module assembly.

the detector ranged as high as 700 KHz, while the maximum readout rate for the charged trigger was about 100 Hz and for the neutral trigger readout was about 1000 Hz. For this reason, a high bandwidth data acquisition system was required and several very selective triggers were designed to separate the charmonium signals from the sea of background.

3.6.1 CCAL Trigger Hardware

The calorimeter trigger [48] provided high speed identification of patterns consistent with two back-to-back, or nearly back-to-back, energy deposits consistent with two body decays such as $J/\psi \rightarrow e^+e^-$ or $\psi' \rightarrow e^+e^-$.

Signals from the 1280 photomultiplier tubes were split in the experimental hall at the level I summer. 97% of the charge from each PMT is transmitted through a delay cable to a FERA ADC. The remaining 3% is directed to the level I summer. In each of the 20 rings, signals from sets of 9 adjacent blocks were summed to form a single signal. The 9 block sums overlap so that blocks at the edge of one sum were also members of the adjacent sum (figure3.10b). The signals from the "super-wedges" were transported to the level II summer located in the counting room. At this stage the CCAL segmentation has been reduced to 20 ring $\times$ 8 super-wedge = 160 channels.

At the level II summer, the 160 signals were again split. A portion of each signal is passed to 160 discriminator modules with a common threshold. The logical OR of the discriminators forms the timing signal for the CCAL readout gate. The remaining portion of the 160 signals is summed along the polar axis. 5 super-rings were formed from the 20 signals from each super-wedge. As in the summation over the azimuthal axis, adjacent super-rings overlap by one block. Table 3.2 gives the summing pattern for the twenty rings. The summation forms forty (5 super-ring $\times$ 8 super-wedge)

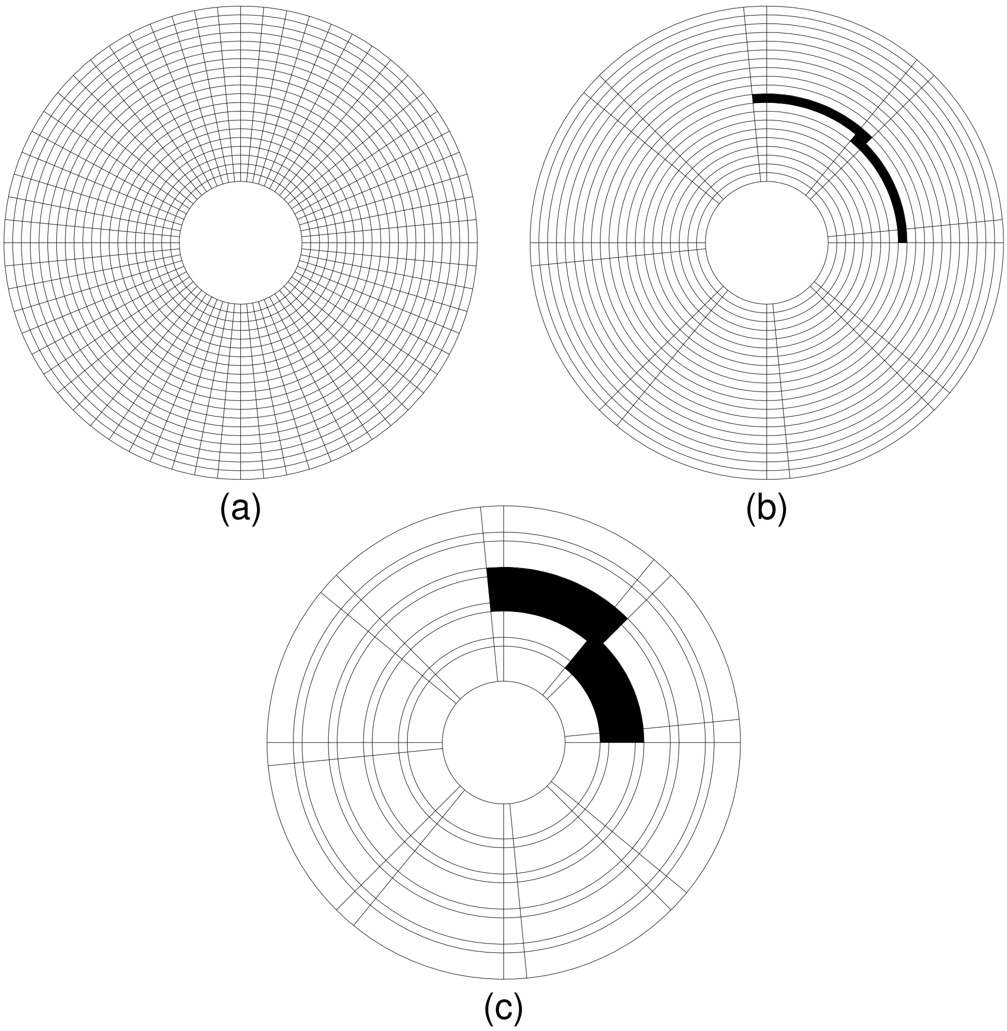

Figure 3.10: CCAL trigger segmentation diagram. (a) CCAL block segmentation, (b) Super-wedge segmentation, (c) Super-block segmentation. Adjacent regions are highlighted in figures (b) and (c) to illustrate the overlap.

super-block signals. Each of the 40 outputs is divided yet again into three signals. One set of forty signals is passed to the CCAL trigger logic and the remaining two were used to determine shower timing. Figure 3.10c is a diagram of the super-block segmentation.

super-ring	ring numbers
1	1-4
2	4-8
3	8-12
4	12-16
5	16-20

Table 3.2: Super-ring summation pattern.

The PBG1 trigger was formed when two of the forty super-blocks were above a discriminator threshold and were either back-to-back in ϕ or were within one super-wedge of being back-to-back. The discriminator thresholds were roughly equal to $\frac{2}{3}$ of the expected pulse height produced by an electron shower from the the reaction $\bar{p}p \to e^+e^-$. The discriminator thresholds therefore gradually increased for each of the five super-rings as θ decreases and also increased with beam energy.

3.6.2 Triggers

The trigger system was divided into three levels. The level 1 triggers form electronic logic elements from pulse height and topological hit patterns in the hodoscopes, the Čerenkov counter, and the calorimeters. The level 2 trigger combines the logic elements generated at level 1 and determines whether or not the event is to be read out. Events passing level 2 were read out into a memory buffer of a real time computing system. There, the level 3 trigger software reconstructs the event and decides whether or not to write the event to tape.

Level 1

At level 1 the following logical trigger elements were formed:

H1OR - Hit detected in the hodoscope H1.

H2OR - Hit detected in the hodoscope H2.

$\mathbf{N_{H1}}$ - H1 Multiplicity. Number of H1 modules hit.

$\mathbf{N_{H2}}$ - H2 Multiplicity. Number of H2 modules hit.

FCVOR - Hit detected in the forward charged veto hodoscope.

CCAL - Hit detected in Central Calorimeter.

PBG1 - Two large deposits detected in central calorimeter super-blocks that are loosely consistent with high invariant mass decays to two body final states. Coincidence between a super-block and one of the three modules azimuthally opposite is required.

PBG2 - The same as **PBG1** except one-to-one coincidence between azimuthally opposite super cluster hits is required.

ETOT - Total energy, as measured by an analog sum of all central calorimeter channels, greater than about 85% of the total lab energy.

FCAL - Hit detected in the forward calorimeter.

h-1991 - Hadron Tag. Coincidence detected between a hit in hodoscope H1 and a hit in any of the 4 modules of

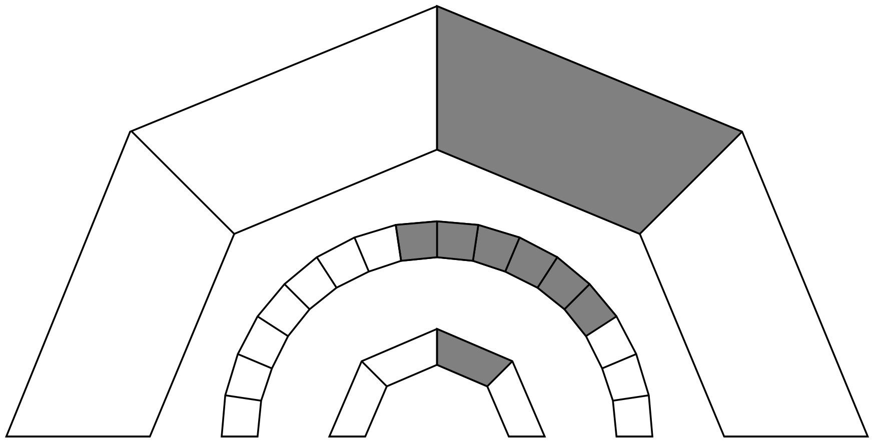

Figure 3.11: Diagram of H1, H2, and Čerenkov elements available to form a hadron or electron tag with 1991 trigger configuration.

hodoscope H2 that subtend the same azimuthal angle or a hit in either of the two adjacent modules. See figure 3.11.

h-1990 - Hadron Tag. Same as **h**-1991 except only the central 4 elements of H2 are included in the coincidence.

e - Electron Tag. A hadron tag detected in coincidence with a hit in the associated Čerenkov counter module.

2h - Two or more hadron tags.

2e - Two or more electron tags.

COPL - Coplanarity. Two hits detected in H2 separated by no more than 17 and no less than 19 counters.

Level 2

The level 2 triggers received as input the logical trigger element generated at level 1. There were four level 2 physics triggers:

MLU1 - Charged Trigger. Identifies candidate events for decays of J/ψ or ψ' to e^+e^-.

MLU2 - Charged Trigger. Identifies candidates events for 2 charged hadron final states such as $\bar{p}p \rightarrow \bar{p}p$ or $\pi^+\pi^-$.

MLU3 - Test trigger.

MLU4 - Neutral trigger. Identifies events with final states containing only γ's.

Events with MLU1, MLU2, or MLU3 triggers would read out all detector elements to the memory buffers. Readout of all detector elements takes about 1 ms. The neutral trigger, MLU4 , only reads out the the hodoscopes and the Calorimeters. Restricting the element readout by the neutral trigger reduces the dead time to 0.1 ms. The MLU2 trigger was prescaled, typically by a factor of 200, due to its high rate.

The MLU1 charged trigger was defined as a logical OR of three groups of level 1 trigger logic elements. The groups were distinguished by the number of Čerenkov counter hits associated with charged tracks. The three trigger groups were defined as follows:

2 Čerenkov - $(\mathrm{PBG1}) \otimes (\mathrm{N_{H1}} \leq 4) \otimes (\mathrm{N_{H2}} \leq 4) \otimes (2\mathrm{h}) \otimes (2\mathrm{e})$

1 Čerenkov - $(\mathrm{PBG1}) \otimes (\mathrm{N_{H1}} = 2) \otimes (\mathrm{N_{H2}} = 2) \otimes (2\mathrm{h}) \otimes (1\mathrm{e}) \otimes (\mathrm{COPL})$

0 Čerenkov - $(\mathrm{PBG1}) \otimes (\mathrm{N_{H1}} = 2) \otimes (\mathrm{N_{H2}} = 2) \otimes (2\mathrm{h}) \otimes (\mathrm{COPL}) \otimes (\overline{\mathrm{FCVOR}})$

Three triggers were implemented to compensate for the low efficiency of the Čerenkov counter in the region of the septum that separates the upstream and downstream cells. A fourth trigger was employed to evaluate the efficiency of the (PBG1) trigger element. This trigger was defined as

2 Čerenkov / No CCAL - $(\mathrm{N_{H1}}=2) \otimes (\mathrm{N_{H2}} = 2) \otimes (2\mathrm{h}) \otimes (2\mathrm{e}) \otimes (\mathrm{COPL}) \otimes (\overline{\mathrm{FCVOR}})$

and was only implemented during running at the J/ψ resonance.

The MLU4 neutral trigger was defined as the logical OR of two level 1 trigger element groups:

Two body - $(\mathrm{PBG1}) \otimes \overline{(\mathrm{H1OR})} \otimes \overline{(\mathrm{FCVOR})}$

Total Energy - $(\mathrm{ETOT}) \otimes \overline{(\mathrm{H1OR})} \otimes \overline{(\mathrm{FCVOR})} \otimes \overline{(\mathrm{FCAL})}$

The first of the two triggers was designed to detect neutral events containing two energy deposits in the CCAL with a high invariant mass, consistent with final states such as $\pi^o\pi^o$ or $\gamma\gamma$. The second of the two triggers detects those events in which most of the available energy was detected by the CCAL.

3.7 Central Calorimeter Gain Monitor

A gain monitoring system [49] was employed to study the drift of the CCAL gain constants between calibrations. A Xenon flash lamp was used to transmit an optical pulse through fiber optic cables to each of the 1280 blocks in the central calorimeter. The output of the flash lamp was monitored with a photomultiplier tube normalized with a ^{207}Bi pulser. The system was triggered at a rate of $\frac{1}{6}$ Hz continuously when the detector was operating.

3.8 Central Calorimeter Reconstruction

The CCAL measures the energy and position of electromagnetic showers produced by high energy electrons and photons. Showers were almost always completely contained within a 3×3 block grid. Each 3×3 grid containing a single shower is called a "cluster".

The offline clustering algorithm searched the CCAL hit map for blocks that contain more energy than each of their neighbors. These blocks defined cluster centers. Each cluster center must have at least 25 MeV and the sum of the cluster center and the eight neighboring blocks must be greater than 50 MeV in order to be reconstructed. In some analyses, the thresholds were lowered to 15 MeV and 25 MeV respectively, but the higher thresholds were used in the analysis presented in this dissertation.

The algorithm loops over the cluster centers and estimates the shower energy as the sum of the energy deposits in each of the nine blocks and the shower position is estimated as the weighted position sum in the ring and wedge directions:

$$r = \frac{\sum_{i=1}^{9} E_i x_i}{\sum_{i=1}^{9} E_i}, \tag{3.2}$$

$$w = \frac{\sum_{i=1}^{9} E_i y_i}{\sum_{i=1}^{9} E_i}. \tag{3.3}$$

In these expressions, E_i is the energy in block i and x_i and y_i are the block numbers in the ring and wedge directions respectively. The block numbers take the values -1, 0 and 1 only. Variables r and w are a measure of the position of the shower center within the central block. $r = 0$ and $w = 0$ corresponds to the block center, and the block edge was defined as r or $w = 0.5$.

Examination of the data reveals that shower position distributions were strongly peaked at block centers, although electrons and photons were smoothly distributed throughout the detector. The energy weighted positions were modified with the functions

$$|r'| = A_r(1 - e^{-\frac{|r|}{r_A}}) + B_r(1 - e^{-\frac{|r|}{r_B}}) \tag{3.4}$$

$$|w'| = A_w(1 - e^{-\frac{|w|}{w_A}}) + B_w(1 - e^{-\frac{|w|}{w_B}}) \tag{3.5}$$

Parameters A_r, r_A, B_r, r_B, A_w, w_A, B_w and w_B were determined by studying test beam data and $J/\psi \to e^+e^-$ decays.

The energy measurement for showers centered near block boundaries was found to be underestimated by simply summing the energy in each of the nine blocks that form the cluster. This was because energy absorbed by the steel fins that separate the blocks within each wedge and the steel skins that separate the wedges was undetected. The energies were corrected based on the position of the shower center with the formula

$$E_{corrected} = \frac{E_{measured}}{(1 - C_{r\pm} e^{-\frac{|r''|}{r_{C\pm}}}).(1 - C_w e^{-\frac{|w''|}{w_C}} - D_w e^{-\frac{|w''|}{w_D}})} \tag{3.6}$$

In this expression, r'' and w'' are the positions of the shower center measured from the edge of the block rather than the block center. The parameters $C_{r\pm}$, $r_{C\pm}$, C_w, w_C, D_w and w_D were determined, as with the position correction parameters, through the study of test beam data and J/ψ decays. To account for the effect of the staggering of the blocks two sets of ring position energy correction parameters were employed. C_{r+} and r_{C+} are used for showers centered upstream of the block center and C_{r-} and r_{C-} are used for showers centered downstream of the block center. All the parameters for both the position and energy correction function are given in table 3.3.

The resolution of the CCAL was determined through the study of data. The RMS energy resolution was estimated to be

$$\frac{\delta E}{E} = \frac{0.05}{\sqrt{E}} + 0.005 + 0.30(E_{corrected} - E_{measured}). \tag{3.7}$$

The RMS resolution of the detector in angles θ and ϕ were parameterized as

$$\delta\theta = (3.67 + 1.63R)\frac{126.46cm}{R_{CCAL}\sin\theta} \qquad mrad, \tag{3.8}$$

Parameter	value	Parameter	value
A_r	0.2601	A_w	0.3138
r_A	0.0321	w_A	0.0397
B_r	0.2574	B_w	0.1969
r_B	0.0397	w_B	0.1715
C_{r-}	0.0614	C_w	0.1474
r_{C-}	0.1357	w_C	0.0204
C_{r+}	0.0857	D_w	0.1594
r_{C+}	0.0508	w_D	0.0784

Table 3.3: Parameters of CCAL reconstruction algorithm.

$$\delta\phi = (5.90 + 2.62W)\frac{78.74cm}{R_{CCAL}} \qquad mrad. \tag{3.9}$$

In these expressions, R and W are the distances from the shower centers to the block boundaries in centimeters in the ring and wedge directions respectively and R_{CCAL} is the distance from the interaction point to the front face of the central block of the cluster. Showers detected only by blocks contained within a single wedge or a single ring were assigned a ϕ or θ error equivalent to a position error of 0.3 times the dimension of the block face.

3.9 Central Calorimeter Calibration

For the 1990 data, the CCAL gain constants were determined by studying showers from $J/\psi \to e^+e^-$ events. For this 2-body decay, energy of an electron is exactly determined by the particle's polar angle which was measured by the tracking chambers. With knowledge of the impact position and energy of the showering electron, the expected energy deposited in each of the nine blocks in the cluster was estimated. Comparison of the predicted energy with the measured ADC channel provided a measurement of the gain constant for each CCAL block illuminated by electrons from J/ψ decays (rings 1-14). Unfortunately, the gain constants could only be measured for data collected at the J/ψ. The gain constant drift in subsequent data runs at other energies was corrected using the gain monitoring system, but errors in normalization of the gain monitor led to a degradation of the detector calibration over time. Furthermore, The accuracy of the gain constants was limited by the number of J/ψ events available. Only about 4000 $J/\psi \to e^+e^-$ events were recorded during the 1990 running period.

In the 1991 data, the CCAL gain constants were measured using $\bar{p}p \to \pi^o\pi^o \to 4\gamma$ events. $\pi^o\pi^o$ events are copiously produced at all beam energies, so the calibration procedure could be repeated with each stack. The calibration procedure was more complex for $\pi^o\pi^o$ events because the shower positions and energies can not be predicted using the tracking chambers. An iterative procedure was developed that approximated the gain constants, calculated the shower energies and positions, and then used the calculated shower energies to reestimate the gain constants. The procedure was repeated until the gains stabilized.

The $\pi^o\pi^o$ calibration procedure could not be used with the 1990 data, because the neutral trigger used to collect $\pi^o\pi^o$ events gated the CCAL with a different timing signal than the charged trigger used to collect $J/\psi \to e^+e^-$ events. The neutral trigger's gate signal was poorly timed and subject to a jitter that often truncated the leading edge of pulses from the calorimeter. The neutral data collected in the 1990 run was unusable. For the 1991 data run, the timing problem was corrected, and a single timing signal was used for both the charged and neutral triggers.

3.10 Central Calorimeter Pile-up

The $\bar{p}p$ annihilation rate ranged as high as 700 kHz during the 1991 data run. At this rate, nearly 10% of the time an uncorrelated $\bar{p}p$ annihilation will occur within a 150 ns CCAL readout gate. Additional backgrounds were present from annihilations prior to the CCAL gate with tails that extend into the gate region. We call showers produced by events not correlated with the event satisfying the trigger "pile-up" showers.

To identify the spurious pile-up clusters, a system of overlapping gates was devised. Two sets of forty signals from the level II summer were passed to a bank of 80 FERA ADCs. The first set was gated with the timing signal used by the CCAL readout gate, the second set was gated 100ns prior to the CCAL trigger gate (figure 3.12). "On-time" clusters can be separated from pile-up clusters by the measurement of the ratio of the charge collected in each of the two gates. Clusters produced by annihilations prior to the trigger were identified by the larger than expected deposit in the early gate, and clusters from late annihilations produced larger than expected deposits in the on time gate. The pile-up identification system was implemented for the 1991 data run only. The pile-up system was able to identify 97 % of pile-up clusters with energies in excess of 150 MeV.

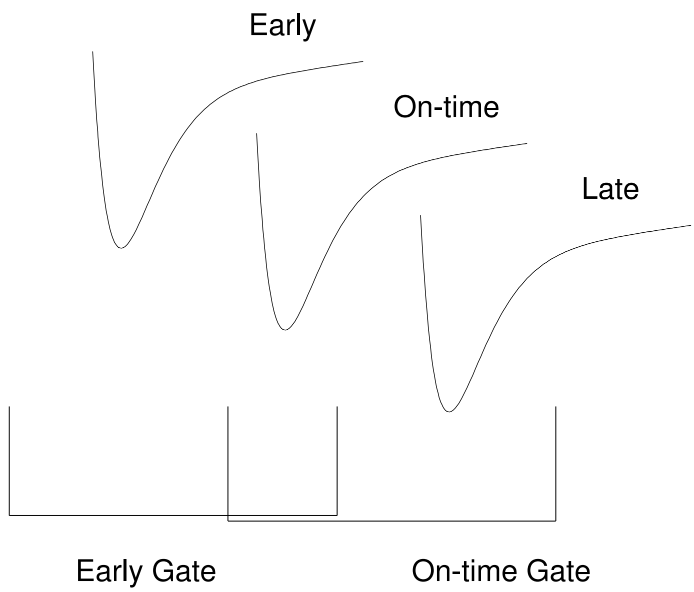

Figure 3.12: Diagram of overlapping gates used to determine cluster timing.

Chapter 4

Charged Trigger Simulation

In this experiment, extremely high interaction rates required that the charged (MLU1) trigger be very selective. The background rate from $\bar{p}p$ annihilations ranged up to 700 kHz while the data acquisition system could only read out about 100 charged trigger events per second. Because the trigger was highly selective the efficiencies for recording J/ψ and ψ' decays to various channels required considerable study.

A charged trigger simulation was developed to evaluate the efficiencies of the MLU1 triggers for various decay channels. The charge trigger was described in chapter 3. The simulation does not "track" particles through the detector in steps as a GEANT[50] simulation, but rather assumes straight trajectories and uses empirical data from detector studies to simulate the response of each of the detector subsystems to simulated event topologies. A simulated hit map is constructed, the selection criteria of each of the MLU1 triggers is applied and the event's trigger status is evaluated. Of particular importance were the multiplicity cuts imposed on the hodoscopes in the charged triggers (2Č: $N_{H1} \leq 4$ and $N_{H2} \leq 4$; 1Č,0Č: $N_{H1} = N_{H2} = 2$). A channel of great importance is the ψ' decay to $J/\psi\pi^+\pi^-$ where the J/ψ decays to an electron positron pair. About 60% of ψ' decays to $J/\psi X$ proceed through this channel. If all four charged tracks in the final state are within the fiducial volume subtended by the hodoscope arrays, then the 1Č and 0Č triggers will reject the event, and if a spurious extra hit is present in either array, the 2Č trigger will reject the event. To correctly determine the trigger efficiency for each channel, the kinematics of the decays were accurately simulated, photon conversion rates in the beam pipe and inner detectors were studied, Dalitz decays of π^o's included, and the efficiencies of each of the detector subsystems and their backgrounds were investigated.

4.1 Hodoscope Simulation

Hodoscopes H1 and H2 were designed to have a uniform efficiency of 1.0 for minimum ionizing particles traversing the scintillator paddles. The principal source of background in H1 is δ-rays from beam target interactions. Electrons scattered through the process $\bar{p}e^- \rightarrow \bar{p}e^-$ have barely sufficient energy to penetrate the beam pipe and reach the H1 hodoscope. H2 is positioned too far from the interaction point (IP) for δ-rays from the IP to contribute a significant background. However, δ-rays from the interaction of electrons and charged pions from charmonium decays with the beam pipe and detector materials contributes a significant background.

The rate for δ-ray production from the beam target interaction can be directly calculated. The distribution of electrons scattered with kinetic energy T is given by[51]

$$\frac{d^2N}{dTdx} = \frac{2\pi N_A r_e^2 m_e c^2}{\beta^2 T^2}(1-\beta^2\frac{T}{T_{max}})\Phi_{\bar{p}}\rho_{H_2}. \tag{4.1}$$

N_A is Avogadro's number, r_e is the classical electron radius and m_e is the electron mass. Inserting typical values for the $\bar{p}$ flux, $\Phi_{\bar{p}}$, target density, ρ_{H_2}, antiproton velocity β, target size Δx, and electron kinetic energy, T, and integrating the expression over the range of values of T associated with the angles subtended by H1 and with sufficient energy to penetrate the beam pipe gives an expected spurious hit rate in H1 of $\approx$ 5 MHz. This represents a 10% pile-up rate with the 30 ns hodoscope gate.

Data Run	H1 extra hit rate
1990 J/ψ	0.0093 ± 0.0006
1991 J/ψ	0.0190 ± 0.0008
1990 ψ'	0.0056 ± 0.0021
1991 ψ'	0.0113 ± 0.0031

Table 4.1: Estimated rate for an extra hit in a H1 hodoscope module due to δ-rays from the target.

This is approximately the rate observed in the data. Although the target density and the beam current are very well known, it is difficult to calculate precisely the rate for spurious H1 hits in this manner because the scattered electrons have very low energies and non-uniform efficiency for detection.

The pile-up rate for H1 can be directly measured by selecting a clean sample of J/ψ and ψ' decays to e^+e^- collected with the 2Č trigger. The 2Č trigger allows up to four H1 hits or up to two extra hits in this two charged track decay. The frequency and distribution of extra H1 hits was studied for each data set collected at the J/ψ and the ψ'. The distribution of these extra hits with respect to the primary electrons is shown in figure 4.1a. There is a excess in the modules adjacent to the modules hit by primary electron tracks. This is evidence that that although the primary source of extra hits in H1 is δ-rays from the target, δ-rays from the interaction of the event primaries with the beam pipe also make a non-negligible contribution. In plot 4.1a the contents of bins 2 and 6 are interpreted as coming from δ-rays from the target, and the excess in bins 1,3,5,7 is interpreted as coming from δ-rays from interactions of charmonium decay electrons with the beam pipe. The rate for spurious hits in H1 from δ-rays produced by beam target interactions are given in Table 4.1.

Unlike H1, H2 is not exposed to δ-rays from the target. This can be calculated

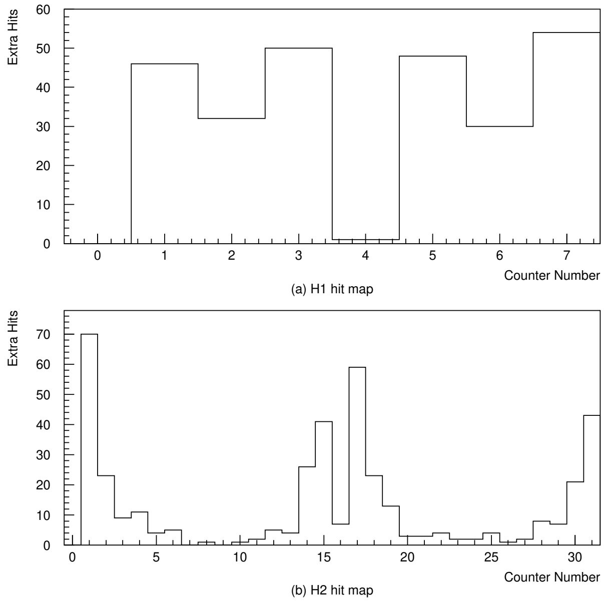

Figure 4.1: Distribution of Spurious hits in H1 and H2. Plotted is the distribution of extra hits (hits not associated with a primary electron track) for a cleanly selected sample of J/ψ events from the 1991 data set. Module 0 is the hodoscope module associated with the electron track with the lowest value of ϕ

directly by summing the materials prior to H2 or more simply by examining figure 4.1b. A significant contribution from δ-rays from the target would manifest itself as a large number of hits in modules at right angles to the event primaries, modules 7-9 and 23-25. The paucity of events in this region indicates that the spurious hits in H2 are entirely from δ-rays produced by event primaries interacting with detector materials.

Unlike event primary electrons, there is no clean sample of charged pions with which to study the extra hit rate due to pion interactions with detector materials. Photon conversion rates are also difficult to study with the data alone. For this reason, a GEANT simulation of the inner detectors was developed to study these backgrounds. Extra hit rates for charged pions and electrons were simulated. Because the rates for spurious H1 and H2 triggers strongly depend on the sensitivity of the hodoscopes, the rates for all processes involving δ-rays are normalized to the observed rates in the data for H1 and H2 for electrons. Figure 4.2 shows the distribution of extra hits from an electron. Notice the consistency between the data (4.1)b and the simulated distribution (4.2)b. The extra hit distribution for charged pions is shown in figure 4.4. The θ_{lab} dependence of the extra hit rate is shown for electrons and pions in figures 4.3 and 4.5. Using the same simulation, the conversion rates for photons prior to H1 and H2 are determined as a function of θ_{lab} (figure 4.6).

By including all the measured and predicted rates and distributions for δ-ray production, both in the target and in the detector materials, the rate for detection of extra hits in hodoscopes H1 and H2 is accurately simulated. Because these rates are not specific to particular charmonium states, but rather to the specific particle species that populate ψ' and J/ψ decays, each decay channel is treated separately.

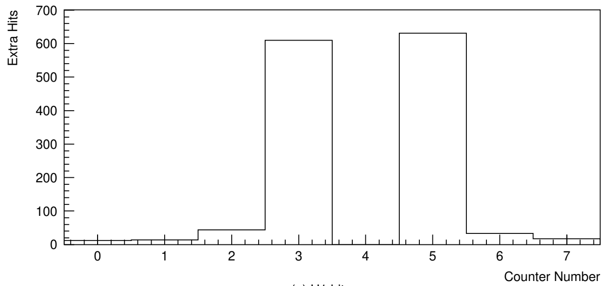

(a) H1 hit map

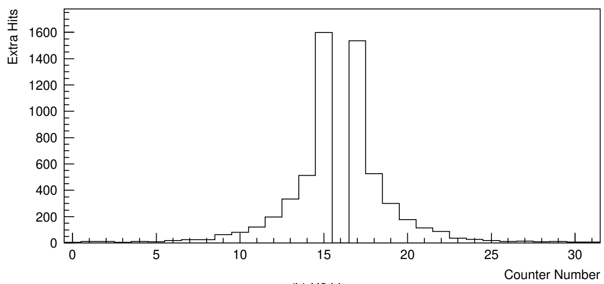

(b) H2 hit map

Figure 4.2: Simulated distribution of extra hodoscope hits produced by a single electron. In figure (a) module 4 is the module hit by the high energy electron. In figure (b) module 16 is hit by the electron.

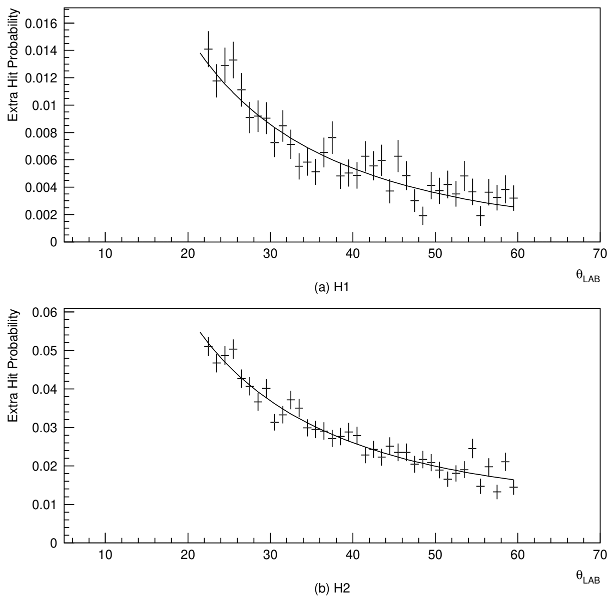

Figure 4.3: Simulated rate for extra H1 and H2 hits due to δ-rays from interactions of electrons from charmonium decays with the material in the inner detectors plotted vs θ.

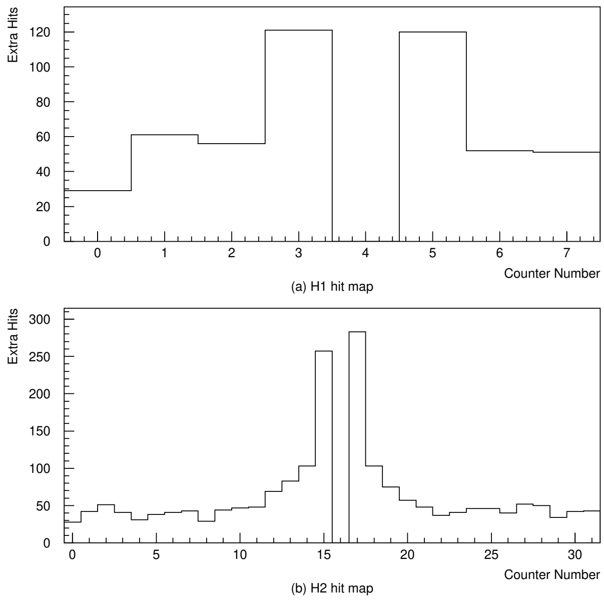

Figure 4.4: Simulated distribution of extra hodoscope hits produced by a single relativistic charged pion.

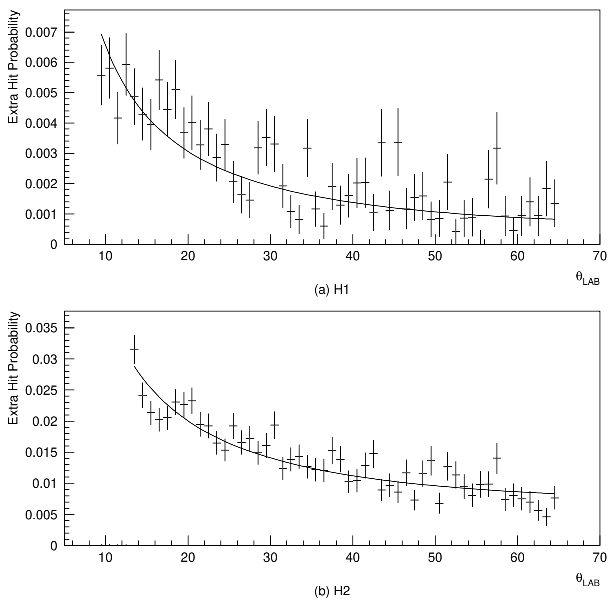

Figure 4.5: Simulated rate of extra hits in H1 and H2 produced by a charged pion plotted as a function of θ_{lab}

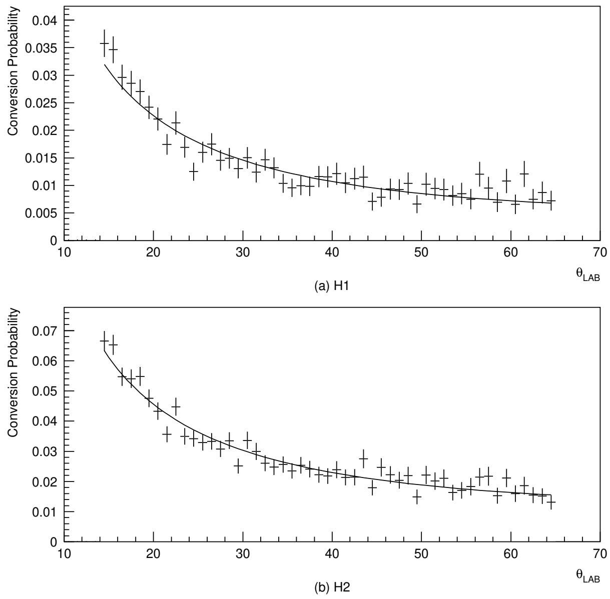

Figure 4.6: Simulated photon conversion rate prior to H1 and H2 plotted vs θ.

Fit Parameter	1990 data	1991 data
A	0.994	0.997
B	0.454	0.517
θ_{septum}	37.6	37.1
σ_1	2.42	2.16
σ_2	0.56	0.94

Table 4.2: Parameters used in simulation of Čerenkov counter trigger efficiency.

4.2 Čerenkov counter efficiency

The efficiency of the Čerenkov counter as a function of θ_{lab} is directly measured by selecting a sample of J/ψ decays with $N_{H1} = 2$, $N_{H2} = 2$, the COPL condition satisfied, and one or both of the electrons is detected by the Čerenkov counter trigger logic. With this selection criteria, if the first electron is detected by the Čerenkov counter, the second electron need not be detected in order for the event to be recorded. The Čerenkov counter trigger efficiency is simply the efficiency for detection of the second electron. Figure 4.7 shows the efficiency of the Čerenkov counter during the 1991 J/ψ data run. The efficiency drop at $\theta \approx 37^o$ is due to the poor optics in the region of the septum that separates the upstream and downstream regions of the chamber. The shape of the distribution is parameterized as

$$\begin{aligned}
\epsilon &= A - Be^{\frac{1}{2}\frac{(\theta-\theta_{septum})^2}{\sigma_1^2}} && \theta < \theta_{septum} \\
&= A - Be^{\frac{1}{2}\frac{(\theta-\theta_{septum})^2}{\sigma_2^2}} && \theta > \theta_{septum}. \qquad (4.2)
\end{aligned}$$

The values for fit parameters A, B, θ_{septum}, σ_1, and σ_2 for the 1990 and 1991 data runs are given in table 4.2.

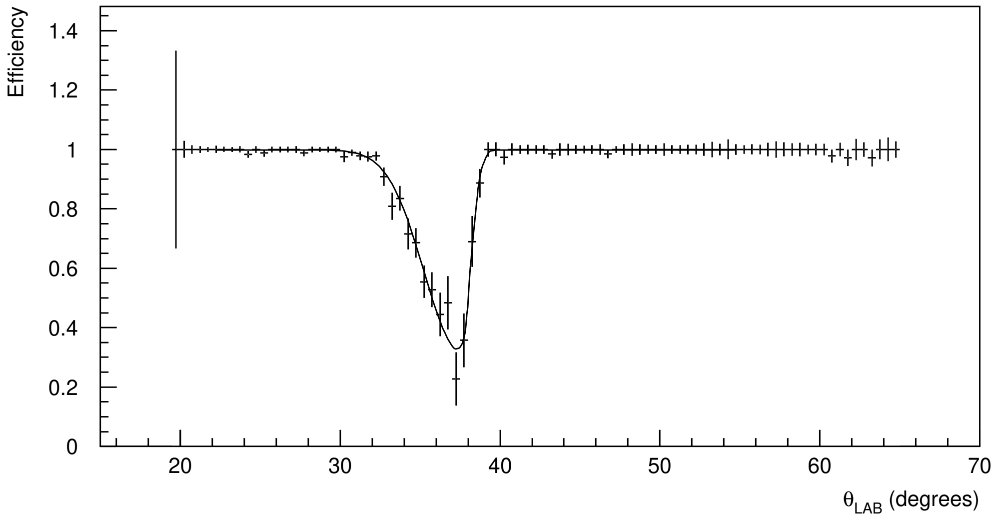

Figure 4.7: Efficiency of Cerenkov counter as a function of θ_{lab} determined from the 1991 J/ψ data.

Data Run	FCV spurious hit rate
1990 J/ψ	0.029 ± 0.003
1991 J/ψ	0.034 ± 0.003
1990 ψ'	0.038 ± 0.013
1991 ψ'	0.049 ± 0.013

Table 4.3: Rate for spurious hits in the forward charged veto.

4.3 CCAL and FCV

The efficiency of the central calorimeter trigger (PBG1) requirement was measured by examining a sample of J/ψ events selected by hodoscope and Čerenkov counter signals alone. In a sample of 2786 events from the 1991 data run, all were found to satisfy the PBG1 requirement. This trigger element was excluded from the trigger Monte Carlo simulation.

The forward charged veto (FCV) suffers backgrounds from the same sources as the other hodoscopes. Spurious hits in the FCV will reject events that would have otherwise satisfied the 0Č trigger. The rate for spurious FCV hits was measured by examining clean samples of J/ψ and ψ' decays to e^+e^- collected through the 1Č and 2Č triggers. The rates for spurious hits in the FCV are given in table 4.3. Detailed studies of the photon conversion rates and δ-ray production rates due to interaction of charge particles with detector materials in the forward region were not performed because of the relative unimportance of the 0Č trigger.

4.4 The Simulation

Event generators are used to simulate the distribution of final state particles for decays of J/ψ and ψ' resonances to e^+e^- and e^+e^-X. For each event, H1, H2, FCV and Čerenkov counter hit maps are constructed with the appropriate probabilities for extra hits in the hodoscopes and the efficiency of the Čerenkov counter. From the detector hit maps, the level 1 trigger elements are reconstructed and event is determined to either pass of fail each of the available triggers.

Examination of the distribution of $J/\psi \to e^+e^-$ events plotted as a function of ϕ shows dips in the regions near the edges of the H1 modules (figure 4.8). This reduction of efficiency has been interpreted as "cracks" in the H1 hodoscope[49, 52]. Presumably, events were lost because particles slipped undetected between H1 modules. This simulation demonstrates that there is another explanation. Because of the finite size of the interaction region and small radius of H1, the triggered H1 module is not always in the same octant as the triggered Čerenkov counter element. Only H1 and Čerenkov counter hits within the same octant are identified as "electron" tracks by the trigger. With only one of the two tracks identified as an "electron", the 2Č trigger can not be satisfied. The presence of an additional spurious H1 or H2 hit will demand the rejection of the event by all triggers. Figure 4.9 is an example of an event topology that would be rejected by all charged triggers.

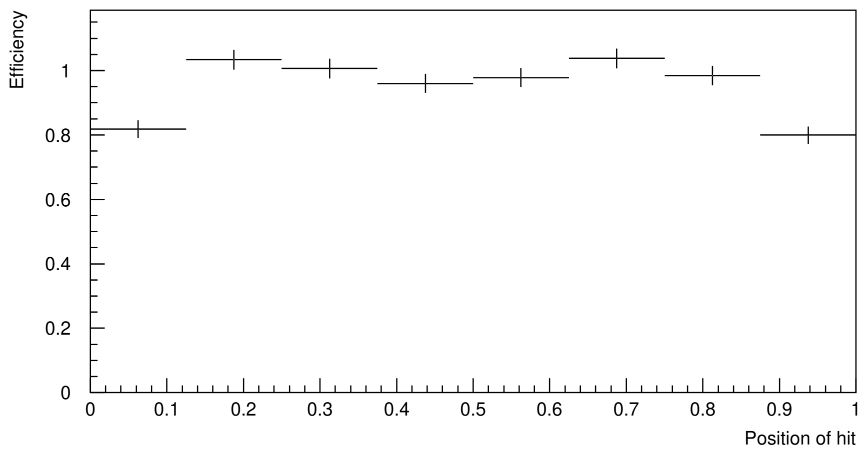

Figure 4.8: Efficiency for the detection of J/ψ events vs ϕ_e. Hit position 0 represents the minimum ϕ covered by an H1 module and 1 represents the maximum value. Data from all eight modules have been combined. The efficiency has been normalized so that the average of the central six bins is 1.0.

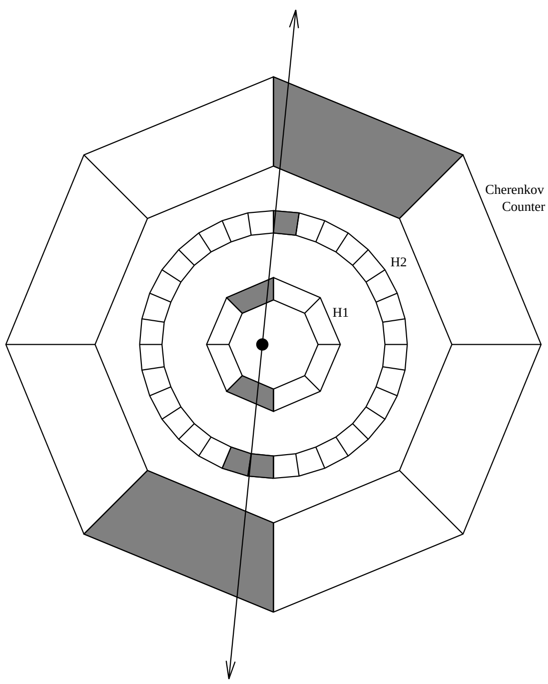

Figure 4.9: An example of a rejected $J/\psi \to e^+e^-$ event topology.

Chapter 5

Central Calorimeter Simulation

5.1 Introduction

The optimal method of selecting events by their kinematical topologies is by means of a kinematical fit. Fits of this sort invariably assume Gaussian distributed errors and understanding of correlations between measured variables. In application the energy and angular error distributions typically have non-Gaussian features, usually long tails, and the correlations between kinematic variables are seldom well understood. By only approximating the error matrix in a kinematic fit, the calculated χ^2 of fit cannot be expected to be distributed as predicted. Long non-Gaussian tails give rise to a larger than expected number of events with a large χ^2. For this reason, a GEANT[50] based Monte Carlo simulation has been developed that simulates the response of the central calorimeter to evaluate event selection efficiencies for kinematical cuts. The simulation reads data files output from the event generators in the charged trigger simulation. Event primaries are tracked through the inner detectors where interaction with material is simulated and secondary showering particles are produced and tracked as well. In the CCAL, the production of Čerenkov light is estimated and converted into a an ADC channel number. The hit maps are then reconstructed by the offline CCAL software used to reconstruct data and treated from that point on as actual

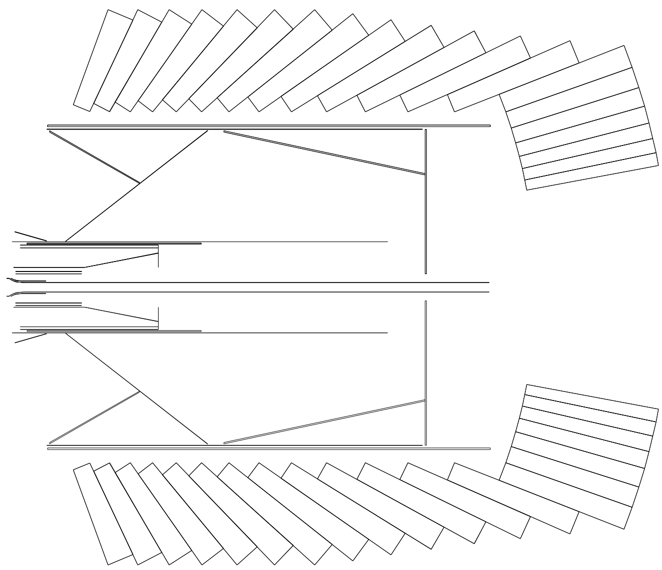

Figure 5.1: Cross section of E760 detector.

data.

5.2 The Detector Geometry

Great effort was made to include a detailed description of the central calorimeter and the inner detectors. Although, the latter are not "active" elements in the simulation, correct representation of the distribution of mass in the inner detectors is required in order to correctly simulate energy loss and scattering processes that will effect the eventual shower distributions in the central calorimeter. Figures 5.1 and 5.2 display a cross section of the E760 detector and the inner detectors as described within the simulation.

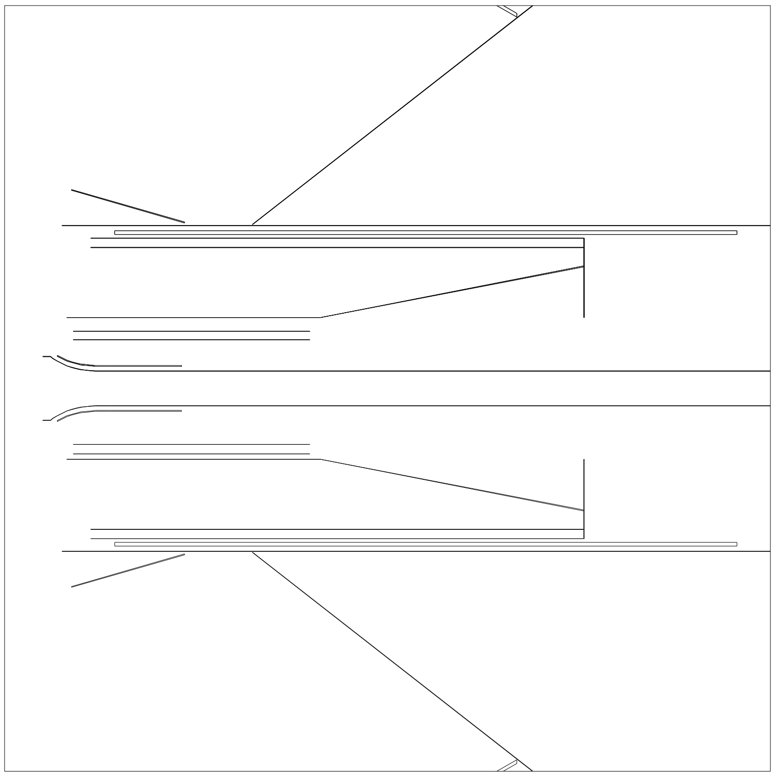

Figure 5.2: Cross section of inner detectors.

5.3 Shower Simulation

When charged particles pass through lead glass at high velocities ($\beta > \frac{1}{n}$), Čerenkov radiation is produced. The radiation is emitted in a cone with $cos\theta = \frac{1}{\beta n}$. This radiation is the principal source of light detected by the PMT. A complete simulation of the detector response would require not only the tracking of high energy showering particles, but also the generation and tracking of Čerenkov photons. The photons would need to be tracked from production to absorption by either the photocathode of a PMT or other material. At each interface the reflection probability would need to be calculated. This would require not only the knowledge of the photon's momentum, but also its polarization and the reflective characteristics of each surface would need to be understood. The choice was made to not track Čerenkov photons, but simply record the number of photons produced. There were two reasons for this: 1) The computing time required to reconstruct each event is dramatically reduced; and 2) Studies have demonstrated that the number of photons detected by the PMT is $\approx 4000\frac{\gamma}{GeV}$[52], but the energy resolution of a 1 GeV shower is about 5%. If photon statistics dominated the energy measurement, the error would be much smaller. In fact, it is fluctuations in the development of the electromagnetic shower that limits the energy resolution. Čerenkov photon tracking is complex and time consuming and would not significantly improve the performance of this simulation.

5.3.1 Light Production

The Čerenkov light production distribution of number[37], N, photons is

$$\frac{d^2N}{dxd\lambda} = \frac{2\pi\alpha}{\lambda^2}\left(1 - \frac{1}{(\beta n)^2}\right). \tag{5.1}$$

The number of photons produced by a charge particle in traversing distance dx is proportional to $(1-\frac{1}{(\beta n)^2})dx$. In the simulation, with each step that a charged particle makes a modified path length is recorded that is proportional to the the length of the step times $(1-\frac{1}{(\beta n)^2})$. The sum of the contributions from each step of each charged particle gives a modified path length proportional to the Čerenkov light produced by the showering particles. A 1 GeV shower has an effective path length of about 100 cm.

Simply summing the modified path length of charged particles within each block leads to a transverse shower shape that is broader than observed in the data. The origin of this is easy to understand. Relativistic electrons and positrons with $\beta \approx 1$ radiate Čerenkov light in a cone with an opening angle of 53^o. Electrons and positrons near the shower core typically have a smaller transverse momentum than those particles in the lateral fringes of the shower. Because of the pointing geometry of the CCAL, less light is detected from particles with a large transverse momentum, because the Čerenkov radiation is less likely to be emitted in the direction of the PMT. The remedy for this problem was to weight the path length sum by a geometric factor,$G(\theta_{PMT})$, so only Čerenkov photons with initial momentum toward the PMT are considered by the simulation. The new modified path length is expressed as

$$\sum_{particles} \int (1-\frac{1}{(n\beta)^2}) G(\theta_{PMT}) dx. \tag{5.2}$$

$$G(\theta_{PMT}) = \begin{cases} 1 & \theta_{PMT} < \frac{\pi}{2} - \theta_C \\ \frac{1}{\pi}[\pi - cos^{-1}(\frac{tan(\frac{\pi}{2}-\theta_{PMT})}{tan\theta_C})] & \frac{\pi}{2} - \theta_C < \theta_{PMT} < \frac{\pi}{2} + \theta_C \\ 0 & \theta_{PMT} > \frac{\pi}{2} + \theta_C \end{cases} \tag{5.3}$$

In this expression, the θ_{PMT} is the angle between the particle momentum and the direction to the PMT and θ_C is the angle of the Čerenkov cone. The additional term simply modifies the path length sum to only include light emitted in a direction that is within 90^o of the direction to the PMT. The additional term reduces the effective path length to about $\frac{70cm}{GeV}$. Clearly, it is possible for Čerenkov photons with initial momentum moving away from the PMT to reflect off the front face of the block and be detected, and likewise it is possible that photons produced moving toward the PMT might escape detection. However, this simple modification, in practice, reproduces the transverse shape observed in the data adequately.

5.3.2 Building a Monte Carlo Event

The GEANT simulation records the modified path lengths for each block and divides each by 70 $\frac{cm}{GeV}$ to convert from path length to energy. Each block energy is then smeared by $\frac{1}{\sqrt{4000 E_{block}(GeV)}}$ percent to account for the statistical error in the number of photoelectrons collected by the PMT. The energy is then converted to an ADC channel number using a set of CCAL gain constants and pedestals taken from the offline analysis code library. Dead channels are set to zero. Channels with counts less than threshold (typically 5-15 MeV above pedestal) are also set to zero. The data acquisition system only reads those channels greater than 2-6 count above the pedestal. By not reading out small energy deposits, significant dead time is avoided at the expense of sensitivity. The final step is to multiply the ADC counts by the gain constants to recover measured block energies. The block energies are then saved for later analysis.

A subroutine within the offline reconstruction program reads in the simulated block energies. The simulated block energies are further smeared to account for the uncertainty in the knowledge of detector gain constants. In the 1991 data, the gain constant resolution was determined by requiring that the width of the J/ψ electron pair mass distribution be equal in the data and in the simulation. The gain constant resolution was determined to be $2.3 \pm 0.5\%$.

In the 1990 data, the stack to stack calibration quality varied. The charged and neutral triggers were gated by different timing signals, and the neutral trigger's gate was poorly timed and subject to a jitter that truncated a portion of some PMT pulses. Different gain constants were required for data collected by the charged and neutral triggers. The separation of gain constants meant that the calibration method employed in the 1991 data using $\pi^o\pi^o$ events could not be used in the 1990 data. Instead, calibration was done using electrons from J/ψ decays. This method worked well enough, but calibration could not be performed on a stack to stack basis. There was significant drift in the gain constants between stacks, so the gain constant resolution must be determined separately for each data set. Fortunately, this simulation was only required to evaluate data collected at the ψ' resonance in the 1990 data. The number of ψ' events was calculated by subtracting the estimated background from the number of candidates in the ψ' data sample. All ψ' events observable by this experiment decay by one of two channels: $\psi' \to e^+e^-$ or $\psi' \to J/\psi X \to e^+e^-X$. Kinematical fits were used to identify events from the two decay channels. Because all the candidates decay to one of the two channels, it must be true that

$$N_{\psi'} = \frac{N_{ee}}{\epsilon_{ee}} + \frac{N_{J/\psi X}}{\epsilon_{J/\psi X}}, \tag{5.4}$$

where $N_{\psi'}$ is the number of ψ' events, N_{ee} and $N_{J/\psi X}$ are the number of events identified by kinematical fit as coming from each of the two available decay channels and ϵ_{ee} and $\epsilon_{J/\psi}$ are the efficiencies for the two kinematical fits as determined by the simulation. The resolution of the gain constants was modified so that the above condition was satisfied. The gain constant resolution for the 1990 ψ' data was conservatively estimated to be $5.0 \pm 2.0\%$.

Finally, the hit CCAL channels were reconstructed with the offline software and fed through the analysis pipeline used to identify various final states.

5.4 Comparison with Data

Performance of a simulation of this sort can be evaluated by examination of the energy distribution and the spatial distribution of showers. The simulation is best evaluated by comparison of $J/\psi \rightarrow e^+e^-$ events. This channel can be cleanly reconstructed without cuts on calorimeter signals. Figure 5.3a is a plot of the "cluster mass" of $J/\psi \rightarrow e^+e^-$ showers. The "cluster mass" is defined as

$$CM = \sqrt{\left(\sum_{i=1}^{N_{blocks}} E_i\right)^2 - \left(\sum_{i=1}^{N_{blocks}} E_i cos\theta_i\right)^2}. \tag{5.5}$$

In this expression, E_i is the energy in block i and $cos\theta_i$ is the angle between the center of block i and the reconstructed shower center; the interaction region defines the origin. The sum is performed over a 5×5 grid centered on the block containing the shower center. This variable is a direct measure of the transverse shower shape. There is good agreement between the simulation and the data.

Figure 5.3b is a plot of the invariant mass distribution for the e^+e^- produced in J/ψ decays. The data again shows good agreement with the simulation.

Figure 5.4 is a cross section of the detector with a simulated J/ψ decay. The charged tracks are shown. Studies have shown that the expected 95% shower energy containment is consistent with the results of the simulation. However, most of the escaping energy is in the form of soft gammas with insufficient energy to pair produce or Compton scatter an electron to a velocity high enough to produce Čerenkov radiation. The containment of particles capable of producing Čerenkov radiation is nearly 100%. The shower maximum for high energy showers is only about one third of the way into the block and only varies weakly with shower energy. One would expect that

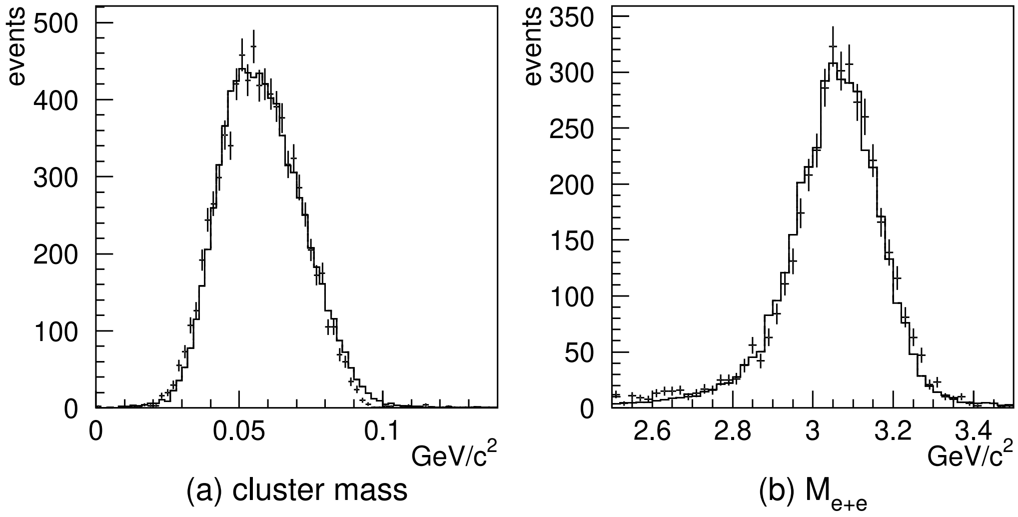

Figure 5.3: Comparison of simulation (histogram) and data (+). Figure (a) is the shower mass distribution for showers from $J/\psi \to e^+e^-$ events. Figure (b) shows the electron-positron invariant mass distribution

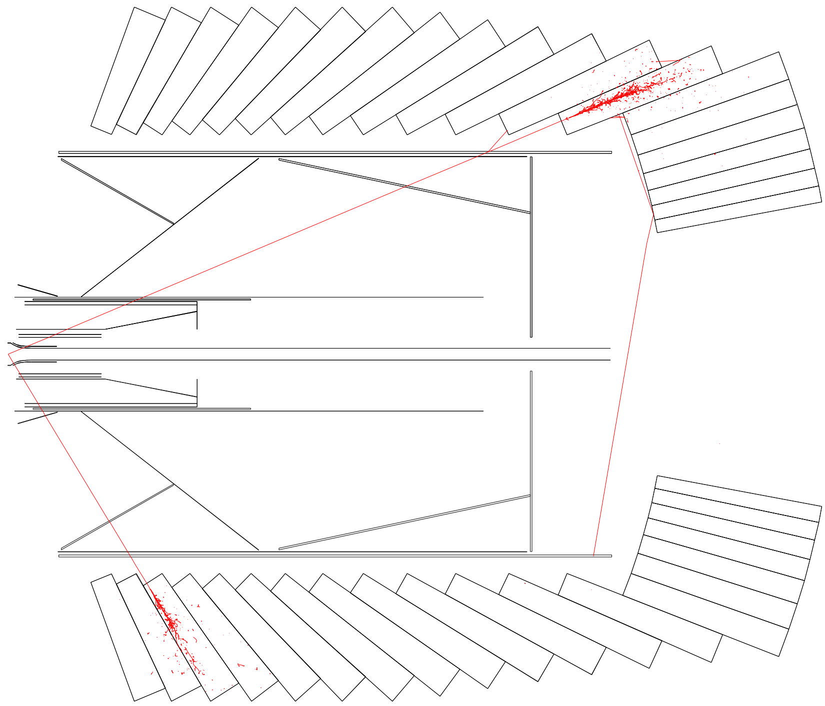

Figure 5.4: A simulated $J/\psi \to e^+e^-$ event.

any nonlinearity due to attenuation of Čerenkov photons is a small effect. However, if further studies revealed otherwise, it would be a simple matter to include the effect in this simulation.

5.5 Calorimeter studies

The simulation allows for detailed studies of detector performance in energy domains that are not easily accessible through study of the data. One must not lose sight of the fact that no simulation is complete. However, the simulation does include the fundamental physics that governs electromagnetic showers in lead glass, and therefore the characteristics that it illuminates are almost certainly real.

The simulation was calibrated using data from J/ψ decays to electron positron pairs. Electromagnetic showers from this source range in energy from about 1.5 GeV to 3.5 GeV. In this section, the calorimeter performance for low energy showers is examined.

5.5.1 Calorimeter Linearity

The linearity of the energy measurements by the central calorimeter can be calculated directly by studying the process $\bar{p}p \to \pi^o X$. Events collected by the neutral trigger are mostly composed of neutral pions that are detected by their decays to $\gamma\gamma$. In each event, the electromagnetic showers were divided into two groups: Those showers with energies above 1 GeV and those showers with energy below 400 MeV. Showers with energy between 400 MeV and 1 GeV were excluded. The invariant masses of all the possible pairs including a low energy shower and a high energy shower were calculated. Plotting the mass distribution for all the shower combinations which include a low energy shower from a narrow energy window reveals a clear π^o mass peak near $M_{\gamma\gamma} = 135\frac{MeV}{c^2}$. Deviation from the exact π^o mass is an indication that the energies of the low energy gammas were systematically mismeasured. The invariant mass of the shower pair is proportional to $\sqrt{E_{high}E_{low}}$, so the ratio of the π^0 mass and the measured mass gives

$$\frac{E_{actual}}{E_{measured}} = \sqrt{\frac{M_{\pi^o}}{M_{\gamma\gamma}}}. \tag{5.6}$$

Figure 5.5 compares actual and measured energies as a function of measured gamma energy. The measurements using π^os are indicated by the open circles, and the solid

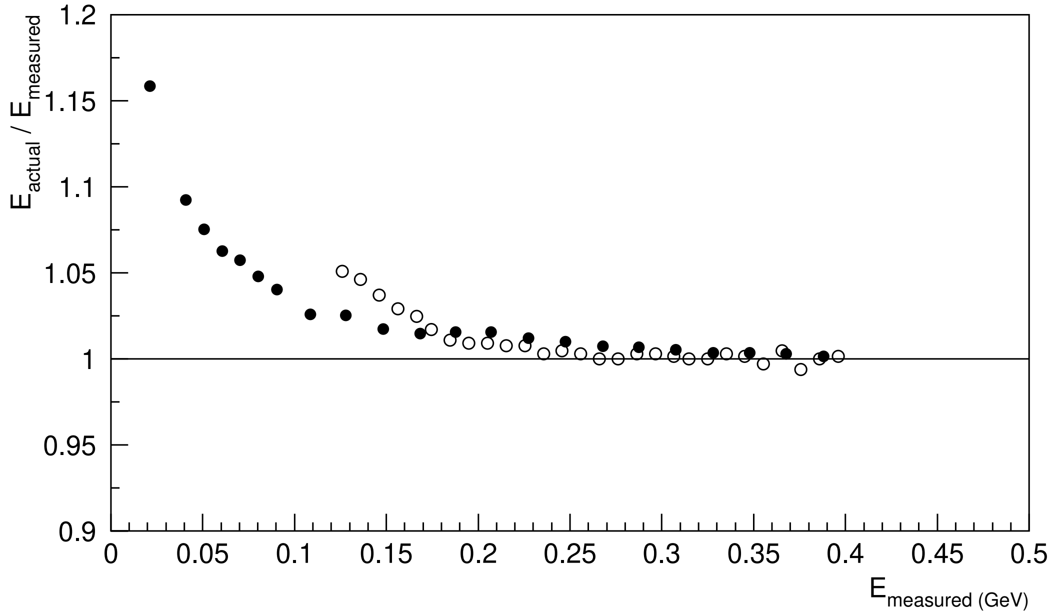

Figure 5.5: CCAL linearity. The open circles are from linearity measurements from data and the solid circles indicate the prediction made by the Monte Carlo simulation.

circles indicate the prediction by the simulation. For data below about 125 MeV it is difficult to clearly distinguish the position of the π^o mass peak with the precision necessary for this measurement. In the region between 100 and 200 MeV, the data shows a larger increase than does the simulation. The source of this discrepancy is not clear. Below 100 MeV, the simulation shows a rapid increase as the energy drops.

The principal source of the nonlinearity in the simulation is understood. As mentioned before, the individual calorimeter block thresholds are set on average about 4 ADC counts above the pedestal. This was done to reduce the number of CCAL channels read out to reduce detector dead time. The average block threshold was about 10 MeV. Low energy showers are often not completely sampled because not all the blocks that contain the shower are read out. For example, consider a 50 MeV gamma

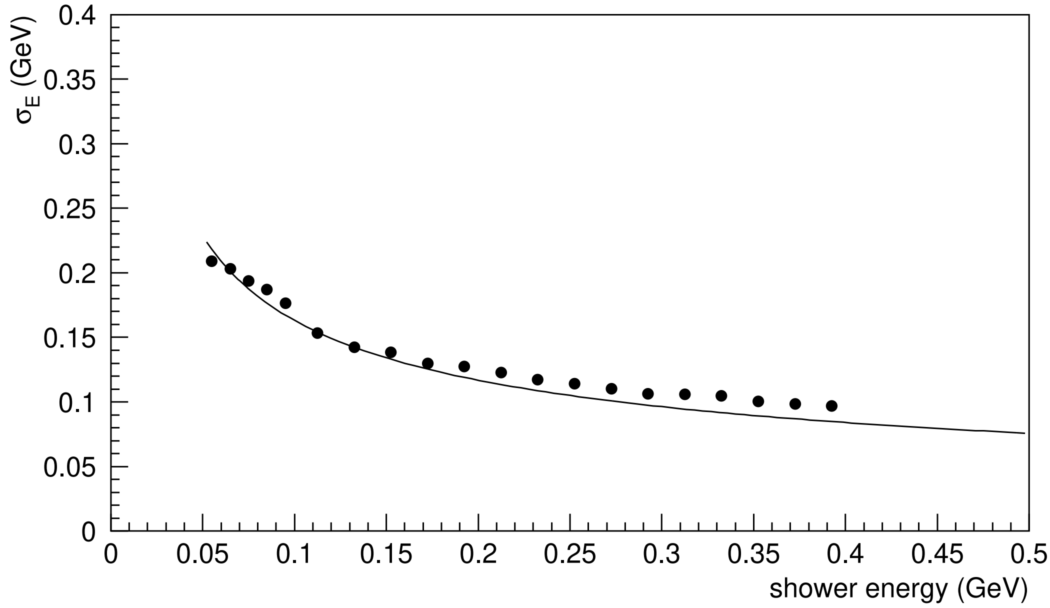

Figure 5.6: Average CCAL resolution for simulated showers. The superimposed curve is the energy resolution parameterization $\sigma_E = 0.05\sqrt{E} + 0.005$.

that deposits 40 MeV in one block and 10 MeV in an adjacent block. If the threshold of the latter block is set above 10 MeV, than only the 40 MeV deposit is read out by the data acquisition system. The shower is reconstructed as being the result of a 40 MeV incident gamma, 20% lower than the actual energy. The effect clearly becomes more severe for lower shower energies.

5.5.2 Calorimeter energy resolution

The simulation's prediction for the average energy resolution of the central calorimeter for showers with energies below 400 MeV is plotted in figure 5.6. The curve superimposed on the plot is the estimated calorimeter resolution, parameterized as $\frac{\sigma_E}{E} = \frac{5.0\%}{\sqrt{E}} + 0.5\%$. The simulation is in good agreement with the predicted resolution.

The shower energy resolution is a function of the position of the shower on the block face. Showers near block boundaries are measured more poorly than showers near block centers because energy is lost in the structural support materials that separate the blocks. The parameterization used in the offline CCAL reconstruction program to describe the energy resolution is

$$\frac{\sigma_E}{E} = \frac{0.05}{\sqrt{E}} + 0.005 + .3 \times E_{corr} \tag{5.7}$$

where E_{corr} is the energy crack correction described in chapter 3. To study the energy resolution as a function of block face position, an ensemble of showers, of energies 100 MeV, 500 MeV and 3 GeV, were generated with ϕ uniformly distributed and $\theta = 30.27389^o$, the center of ring 10. A second data set was generated with ϕ restricted to block centers and θ allowed to vary within the angles subtended by ring 10. Figures 5.7 and 5.8 show the uncorrected and corrected energy distributions as a function of shower block face position (plots a, c and e) and the energy resolution as a function of the block face position (plots b, d and f). Also shown is the average energy error predicted by the offline from equation 5.7. The crack energy correction algorithm reasonably accounts for lost energy near the block boundaries for the 3 GeV shower data, but does a poorer job on the 500 MeV shower sample and is poorer still for 100 MeV showers. The lower energy showers have a smaller transverse size, so a larger percent of the energy in low energy showers centered near block boundaries is absorbed by the metal structural supports between the blocks than is absorbed in high energy showers. The energy correction algorithm adds a fixed percent to the measured shower energy based on the position of the shower center (equation 3.7). The algorithm does not vary with shower energy. The shower energy resolutions also agree well for the high energy showers, and less well at lower energies. The resolution of simulated showers near the block centers is better than predicted by the energy resolution function, but

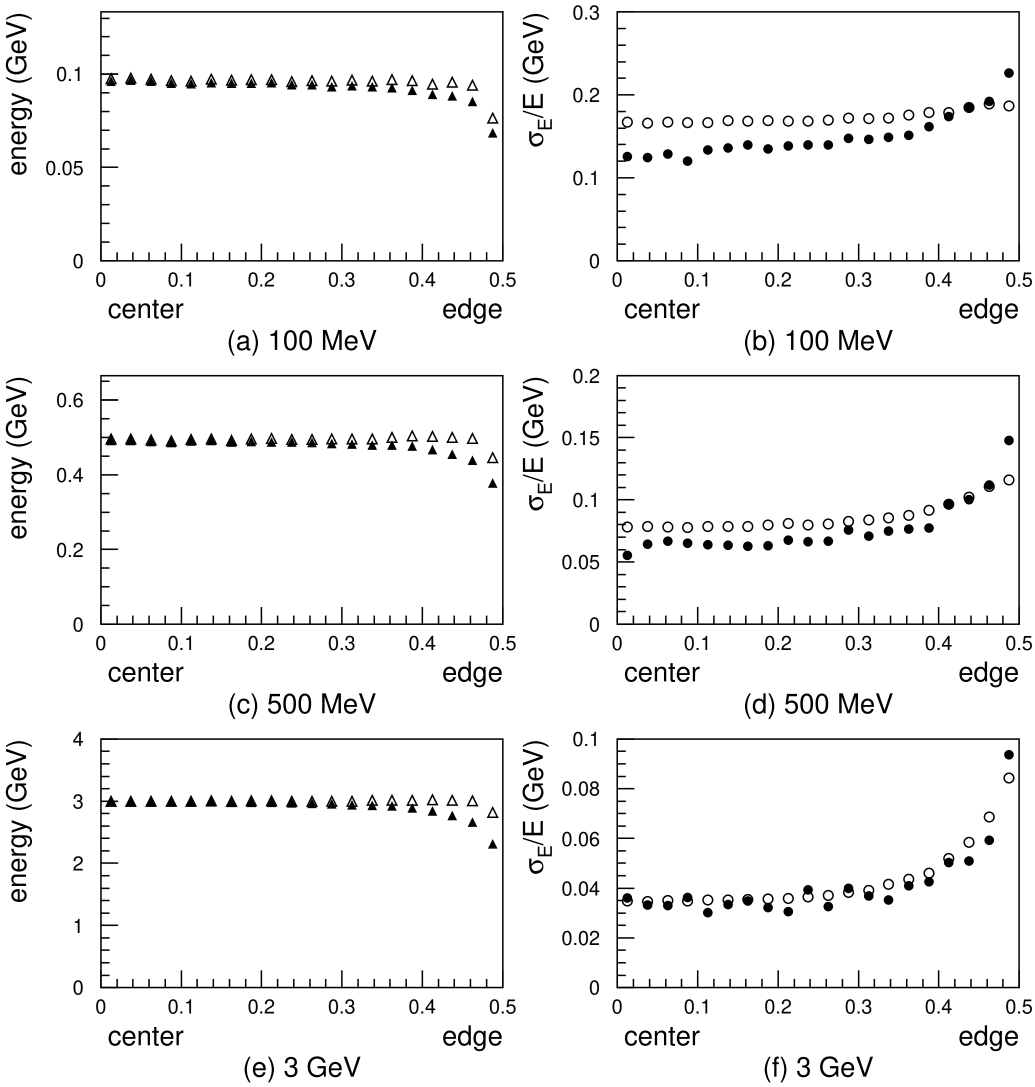

Figure 5.7: Block energy resolution as a function of block position in wedge direction for 100 MeV, 500 MeV and 3 GeV simulated showers. Plots a,c,e show the corrected (open triangle) and uncorrected (filled triangle) energies as a function of wedge position. Plot b,d,f show the energy resolution as a function of block position (filled circle) and the average energy resolution assigned by the offline (open circles). Block position 0.0 is the block center and block position 0.5 is the inter-wedge boundary. These data are for showers in ring 10.

near the block edges, the opposite is true. This is likely due to the underestimation of the block crack correction for low energy showers.

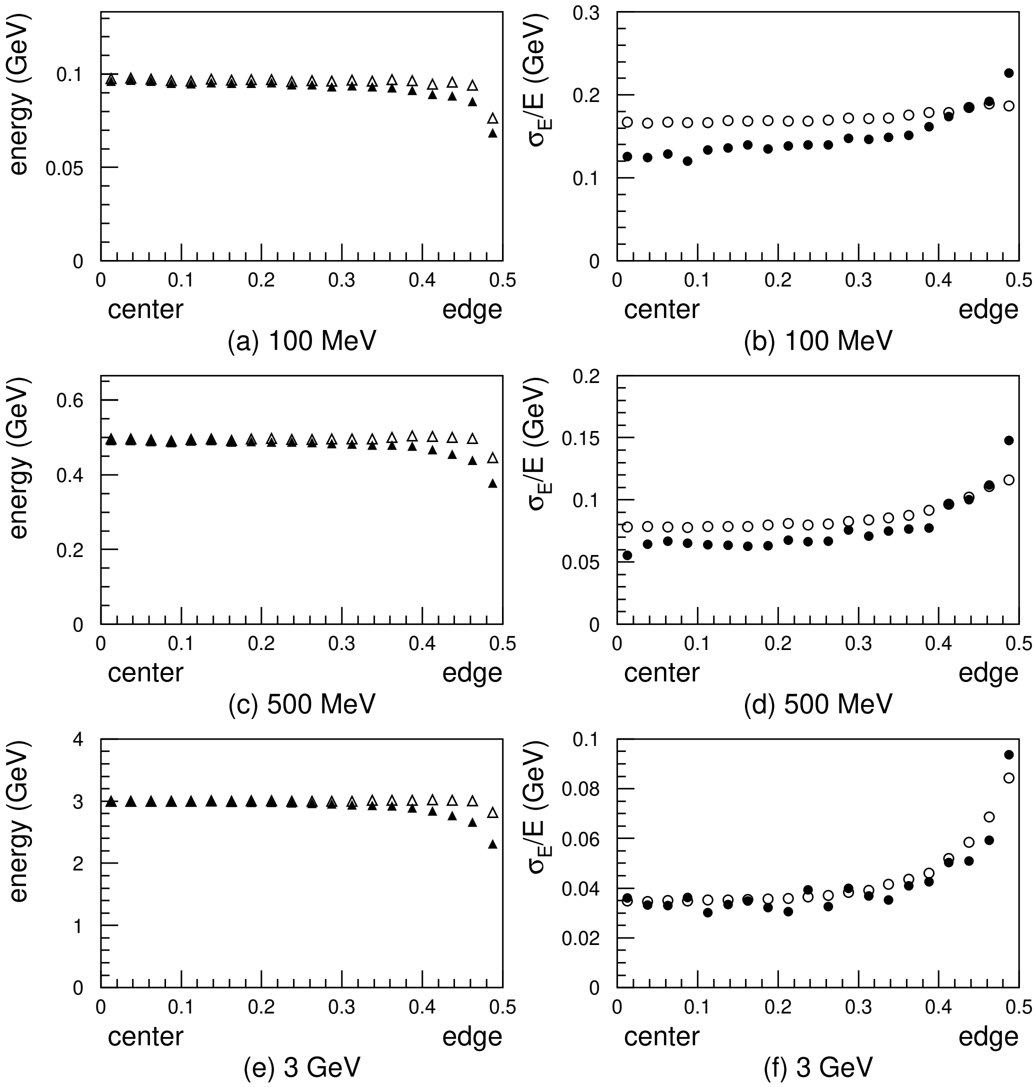

Figure 5.8: Block energy resolution as a function of block position in ring direction for 100 MeV, 500 MeV and 3 GeV simulated showers. Plots a,c,e show the corrected (open triangle) and uncorrected (filled triangle) energies as a function of ring position. Plot b,d,f show the energy resolution as a function of block position (filled circle) and the average energy resolution assigned by the offline (open circles). Block position 0.0 is the block center and block position 0.5 is the inter-ring boundary. These data are for showers in ring 10.

5.5.3 Calorimeter angular resolution

Using the same data generated for the estimation of energy resolution, the shower angular resolution was studied. Figure 5.9 shows the angular resolution as a function of the block position in the ring direction (plots a,c and e) and the wedge direction (plots b, d and f). There is good agreement between the shower simulation and the value predicted by the offline for 3 GeV showers except for near the block boundary where the simulation predicts superior resolution than the offline. However, the simulation does not include the nonnegligible contribution to the angular resolution from vertex position fluctuations. An interaction region with $\sigma_r = 2mm$ and $\sigma_z = 3mm$ adds non-correlated angular errors $\delta_\phi = 2.5mr$ and $\delta_\theta = 1.5mr$. For blocks closer to the target, the uncertainty in the vertex position is the dominant source of error in the angles of incident high energy showering particles that impact near block boundaries. For 100 MeV showers, the simulation predicts that the shower angular resolution is superior near the block centers than near the boundaries. This is not really the case. Showers of energies 100 MeV and below typically are only detected by a single CCAL block, so the offline simply assigns the block center as the best estimate of the shower's position. The offline reports that almost all low energy showers are positioned at block centers; therefore, it is not surprising that the shower resolution at the block centers is higher than near the boundaries.

5.6 Comment on simulation calibration

The simulation has only one free parameter for calibration, the estimated error in the knowledge of the CCAL gain constants. However, an estimate of the number of photoelectrons per GeV is also used in the simulation. These two sources of error scale

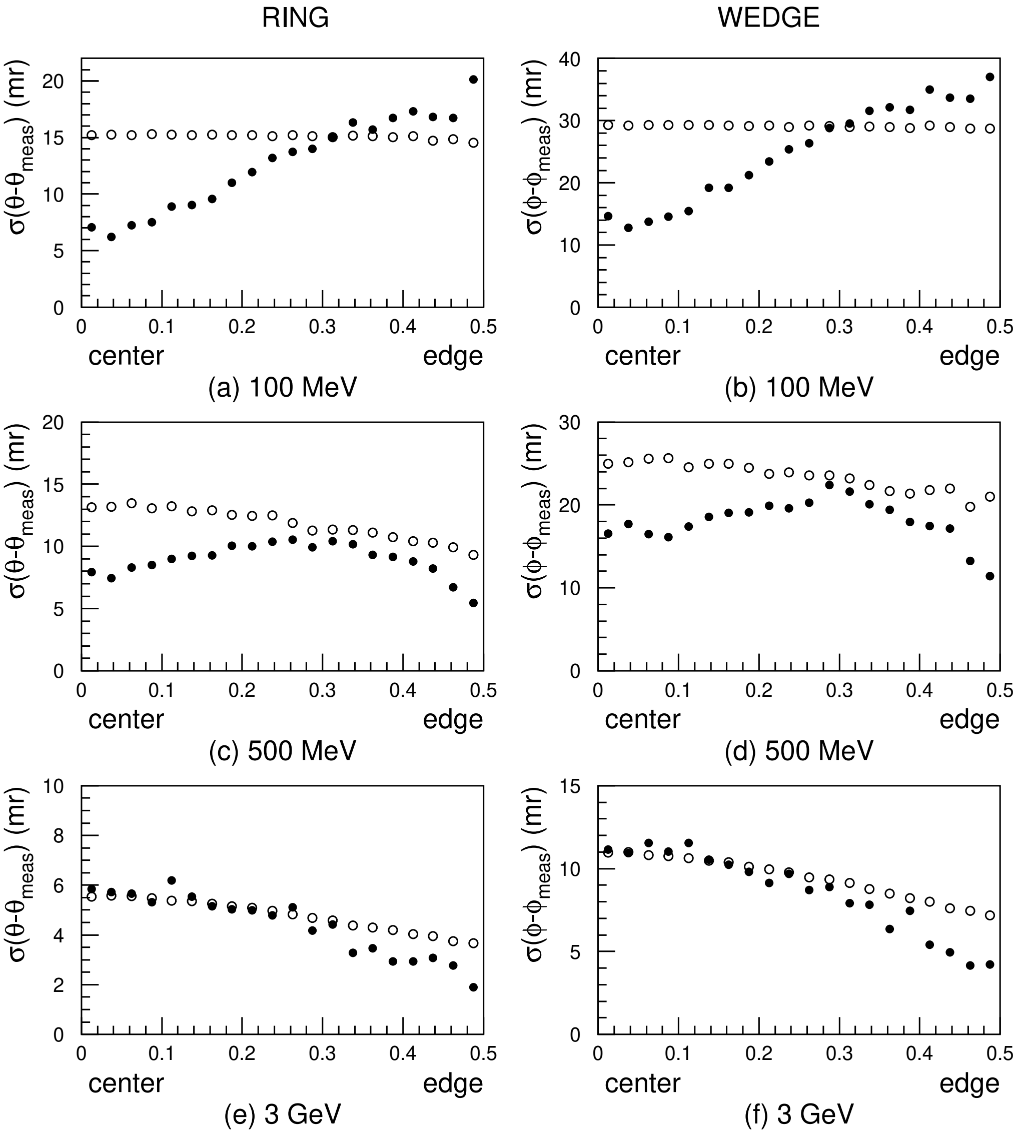

Figure 5.9: Angular resolution as a function of block position for 100 MeV, 500 MeV and 3 GeV simulated showers. Plots a,c,e show the angular resolution of simulated showers (filled circles) and the average shower angular error assigned by the offline (open circles) as a function of block position in the ring direction. Plots b,d,f show the angular resolution of simulated showers as a function of block position in the wedge direction.

differently with energy. CCAL calibration errors scale like $\delta_E \propto E$ and the statistical error in the number of photoelectrons detected scales like $\delta_E \propto \sqrt{E}$. It is likely that other sources of error not considered in this simulation scale in one of these two ways. A more systematic approach to the estimation of the contributions from all sources of error would not label the errors by their source (CCAL gain constant resolution or photo electron counting statistics), but rather label them by how they scale with energy. One could parameterize the error sources as $\delta_E = AE + B\sqrt{E}$. The two parameters, A and B, could be reduced to one by demanding that the energy resolution of electrons from J/ψ decays be reliably reproduced, but a second measurement is required at a different energy scale to isolate the second free parameter. Unfortunately, there is no clean source of low energy photons of known energy to use to calibrate the simulation.

Chapter 6

Cluster Fitting

An effort was undertaken to develop a new method to estimate the best values of energy and position of showers in the E760 lead glass calorimeter. The method described here takes a radical departure from the approach described in chapter 3, where initial estimates of shower energy and shower position (derived from weighted sums) are corrected through study of the data. In this chapter, a general method for calorimeter reconstruction is presented in which the probability for the hypothesis that a shower has a given energy and position is evaluated. Parameterizations and correction functions are excluded from the analysis. All the information about the detector's geometry and resolutions is contained in a single probability function.

6.1 Limitations of the Offline Calorimeter Reconstruction Algorithm

In chapter 3, the E760 offline reconstruction algorithm was described. This algorithm is based on general studies of lead glass calorimeters [53]. In this method the energy of the incident showering particle is estimated to be the sum of the energies in the blocks containing the shower, and the shower position is estimated to be the energy weighted center of mass of the deposits. The energy is known to be underestimated near the block boundaries, where a portion of the shower is absorbed by the steel structural supports, and the position measurement are strongly peaked near the block centers. Both distributions are "corrected" with functions determined by studying the data. Similarly, the functional forms of the error in the energy and shower position are deduced from the data. This approach is quite reasonable and pragmatic, but there is no simple way to expand it to lower energies where a source of electrons or gammas of known energy and trajectory is not available. Furthermore, it is not typically possible to understand the correlations between the measured variables. In the E760 detector there is a strong correlation between energy and position measurements for showers near block boundaries. Listed below are several of the cases in which the E760 offline reconstruction algorithm can return an incorrect result:

- For showers near the edge of the fiducial volume (rings 1 and 20), energy is lost from the detector. In such cases, the shower energy is typically underestimated. Furthermore, the position of the shower is poorly estimated, because the energy weighted center of mass includes no contribution from the lost energy.

- Showers near dead blocks have the same characteristics as showers near the detector boundary. Dead blocks are treated as measurements of zero energy, rather than non-measurements. This leads to an underestimation of the shower energy and a systematic offset in the estimate of the showers position.

- The energy and position correction functions, derived from data at high energies, are assumed to hold for low energy showers as well. In the previous chapter, energy and position correction functions and the position resolution functions were demonstrated to represent poorly simulated data at low energies.

- When a cluster contains only a single hit block, the position resolution is estimated to be 0.3 times the block diameter. This is probably a reasonable estimate for low energy showers, but if a shower of energy in excess of about 500 MeV is only detected by a single block, the estimated error in the shower position should be smaller. If a shower of such high energy was not exactly centered on the central block, it would certainly have been detected by more than 1 block.

In theory, each of these phenomenon could be accounted for by a more complex parameterization of the energy and position correction and resolution functions, but simply parameterizing observed discrepancies between the data and the reconstruction algorithm is not a statistically rigorous approach.

6.2 Cluster Fitting

Consider an electromagnetic shower in a segmented electromagnetic calorimeter of arbitrary geometry and resolution. Define e_i^m as the measured energies in the calorimeter elements containing the shower. If one were to know the functions describing the expected energy deposited by an incident showering particle of energy, E, and spatial coordinates (x,y), $e_i^p(E,x,y)$, and the covariance matrix of the expected energy deposits, $\mathbf{M}_{ij}(E,x,y)$, then one can evaluate the probability of any set of measured energies occuring as result of any specific hypothesis for (E,x,y). The probability is related to the variable χ^2, which is defined as

$$\chi^2(E,x,y) = \sum_i \sum_j (e_i^p - e_i^m)\mathbf{M}_{ij}^{-1}(e_j^p - e_j^m). \tag{6.1}$$

The minimum value of χ^2 with respect to parameters (E,x,y) represents the best estimate of the parameters and the curvature of χ^2 near the minimum describes the covariance matrix of the three parameters.

Using this method, the problem of converting a set of measured energies, e_i^m, into an estimate of the incident particle's energy and impact position is reduced to the determination of e_i^p and $\mathbf{M}_{ij}$ for all possible values of (E,x,y). These functions could be determined by scanning the detector with a variable energy beam. However, testing a detector over its entire range of energy sensitivity and shower position is difficult and expensive. An alternative method is to develop a Monte Carlo simulation of the detector, and use the simulation to map out the predicted energies and the covariance matrix. In this analysis, a simulation similar to the GEANT central calorimeter simulation described in the previous section is employed to estimate e_i^p and $\mathbf{M}_{ij}$.

In order to apply this method, the measured energies must be Gaussian distributed for the statistical approximations to be valid. However, measured energy distributions by electromagnetic showers in lead glass blocks are not Gaussian. The restriction that all measurements be positive skews the shape of small energy deposits. Figure 6.1 is a plot of simulated shower energy deposit in a 3×3 array of lead glass blocks. Although the energy distributions are not normally distributed, the log(energy) distributions are a good approximation of a normal distribution. l_i^p, the expectation value of the log(energy) distribution for block i, and l_i^m, the log of the measured in block i, are therefore substituted for e_i^m and e_i^p, and the covariance matrix is a measure of the correlations and variances of the energy logarithms. Henceforth, χ^2 is defined as

$$\chi^2(E,x,y) = \sum_i \sum_j (l_i^p - l_i^m)\mathbf{M}_{ij}^{-1}(l_j^p - l_j^m). \tag{6.2}$$

6.2.1 Estimation of e_i^p and $\mathbf{M_{ij}}$

Each of the twenty rings in the E760 central calorimeter was constructed with blocks of unique geometry. The largest of the blocks has a face size nearly twice that of the smallest of the blocks. The different geometries certainly affect the energy sharing

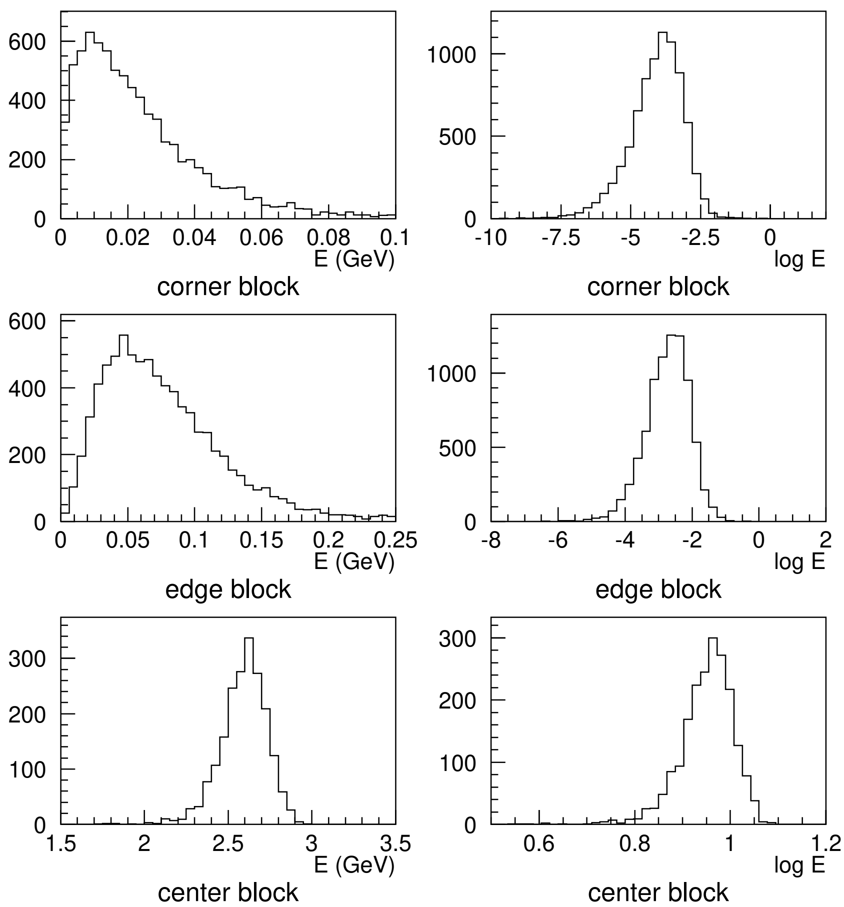

Figure 6.1: Block energy distributions for a 3 GeV shower incident on the center of a simulated 3×3 block grid.

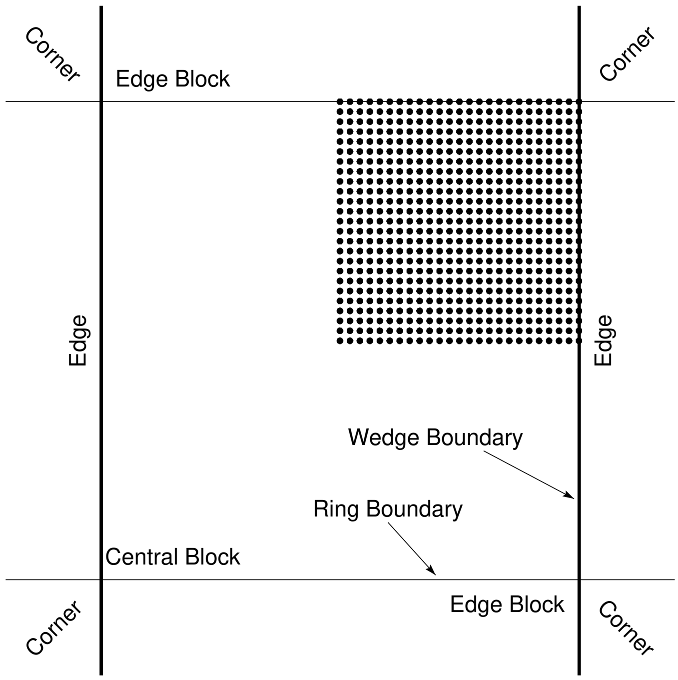

Figure 6.2: Diagram showing pattern of simulated shower positions.

between neighboring blocks and cannot be ignored. However, separate consideration of each of the twenty block geometries was judged to be too time consuming. Instead, two simpler geometries were considered. Two 3×3 arrays of rectilinear blocks were simulated, one with the block face dimensions and length of the largest block in the CCAL and the second with the dimensions of the smallest block. The functions l_i^p and $\mathbf{M_{ij}}$ were obtained by simulating electromagnetic showers at a variety of energies and positions. The predicted energies and covariance matrix elements for the blocks of intermediate dimensions are obtained through linear interpolation.

The predicted energies and covariance matrix elements were estimated by simulating an ensemble of showers at each of 625 points that describe a 25×25 grid in the first quadrant of the two arrays (figure 6.2). The geometry is symmetric under

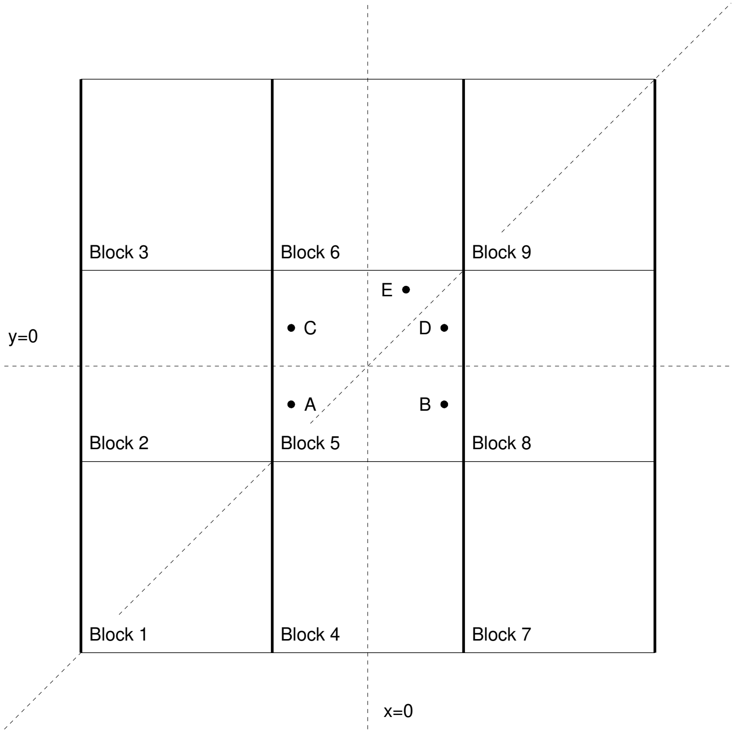

Figure 6.3: Diagram of 3 block grid. The expected energy in block 1 for a shower at point A is equal to the expected energy in block 7 for a shower centered at point B, block 3 at point C or block 9 at point D. Note that there is no diagonal symmetry. The expected energy deposited in block 8 for a shower centered at point D is not the same as the expected energy in block 6 for a shower centered at point E.

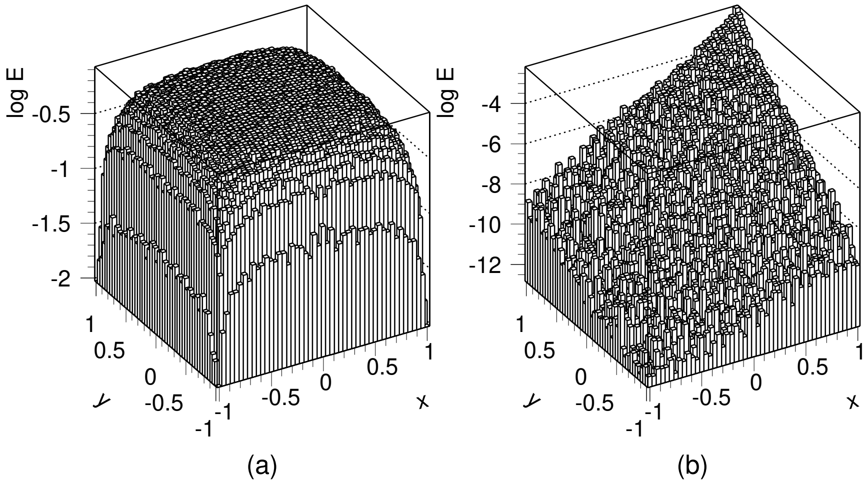

Figure 6.4: Expected l^p distribution for simulated 1 GeV showers for (a) the central block and (b) a corner block (block 9) plotted as a function of the location of the shower center. Position (0,0) is the center of the central block, and x=±1 and y=±1 represents the boundary between the central block and the surrounding 8 blocks.

reflections in the x and y directions, so examination of the first quadrant is sufficient to deduce the expected energies and the covariance matrix for the showers centered throughout entire central block (figure 6.3). Notice that there is no $(x, y) \rightarrow (y, x)$ symmetry in the grid, because the steel separator that divides the lead glass blocks in the wedge direction is thicker than the separator that divides the blocks in the ring direction. Showers were simulated at nine different energies spanning the range of sensitivity of the detector: 31.25 MeV, 63.5 MeV, 125 MeV, 250 MeV, 500 MeV, 1 GeV, 2 GeV, 4 GeV and 8 GeV. Figure 6.4 is a sample of the two typical simulated log(energy) distributions.

Reflection symmetries are exploited to reduce the number of unique block energy maps from nine to four. The center block is unique, but only two maps are required to describe the four edge blocks and each of the corner blocks can be described by a single map. For example, in figure 6.3, The energy deposited in block 1 by a shower

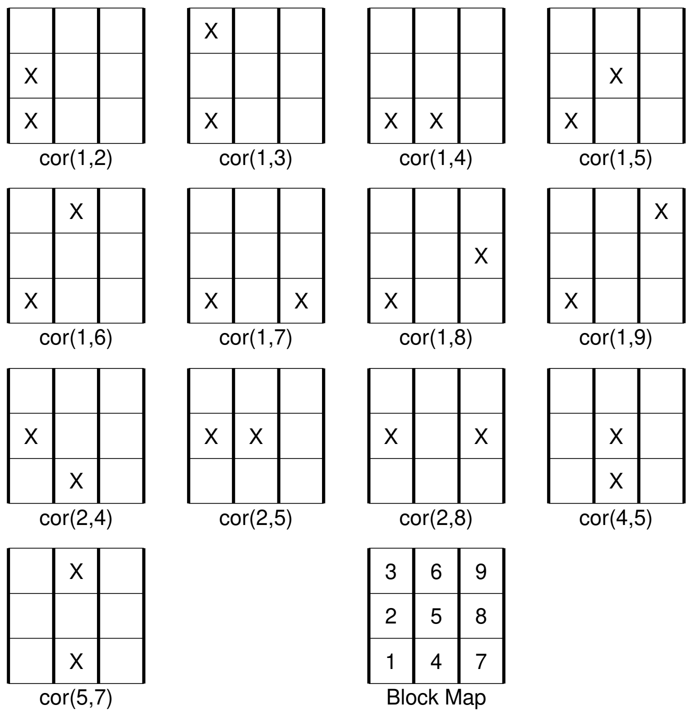

Figure 6.5: List of 13 unique correlations.

at point A is equal to the energy deposited in block 7 at point B, block 3 at point C and block 9 at point D. l_i^p and variance maps for blocks 1, 2, 4 and 5 are sufficient to describe the entire 9 block grid. The number of correlation distributions can be be similarly reduced. In general, a 9×9 covariance matrix has 36 unique off diagonal elements, but the inherent symmetries in the grid are exploited to reduce the number of unique correlations to the 13 listed in figure 6.5.

6.2.2 Smoothing

Because the energy and covariance distributions are so finely sampled in shower position, the distributions describing l_i^p and $\mathbf{M_{ij}}$ are quite rough. These distributions must vary smoothly, so that the χ^2 varies smoothly, otherwise, there is a danger that the numerical minimization routine will find a local minimum, or fail to find a minimum at all. Figure 6.6a is a plot of a variance distribution prior to smoothing. The 49×49 energy and covariance matrix element distributions were smoothed with the formula

$$a'_{ij} = \frac{\sum_{k=-d_k}^{d_k} \sum_{l=-d_l}^{d_l} \frac{a_{i+k,j+l}}{(3^2+k^2+l^2)^2}}{\sum_{k=-d_k}^{d_k} \sum_{l=-d_l}^{d_l} \frac{1}{(3^2+k^2+l^2)^2}}. \tag{6.3}$$

a'_{ij} is the smoothed distribution element and $a_{i+k,j+l}$ is the unsmoothed element. d_k and d_l define the distance of the smoothing. To avoid smoothing away the rapidly varying features near the edge of the energy and covariance distributions, d_k and d_l are reduced near the block boundaries. The values of d_k and d_l are functions of i and j and are given in table 6.1. Figure 6.6b is a plot of the variance distribution

$d_k(i)$, $d_l(j)$	i or j
0	-24, -23, -22, 22, 23, 24
1	-21, 21
2	-20, 20
3	-19, 19
4	-19, 18
5	-17, 17
6	-16, 16
7	-15 to 15

Table 6.1: Smoothing distance for various block positions.

shown in plot (a) after smoothing. Examples of a l_i^p, and covariance matrix element distributions are shown in figures 6.7,6.8,6.9, 6.10. The square root of the variances are shown and the correlation coefficients, defined as $cor(i,j) = \frac{\mathbf{M_{ij}}}{\sqrt{\mathbf{M_{ii}M_{jj}}}}$, are shown instead of the covariances. The correlations between the edge blocks and the central block is nearly always negative and in some cases ranges as low as -0.8 near the block

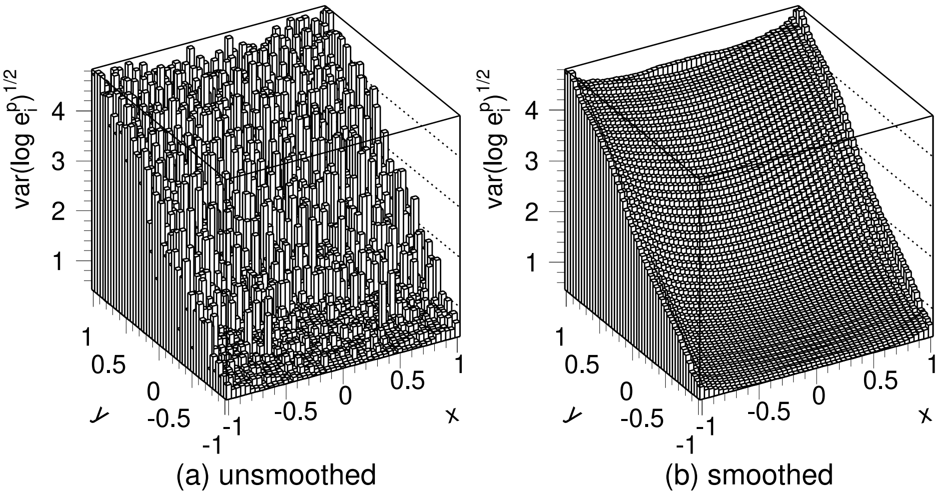

Figure 6.6: Smoothed and unsmoothed plot of the variance in block 4 for 1 GeV showers in the large 3×3 grid.

boundaries. This purely due to energy conservation. If fluctuations in the spatial development of the shower lead to a smaller than expected deposit in the central block, then the lost energy is necessarily deposited in the surrounding blocks. Correlations between neighboring edge blocks (eg. cor(1,2)) are typically positive; blocks on opposite sides of the array (eg. cor(2,8)) have negative correlations.

No smoothing is performed with respect to the energy dimension.

6.2.3 Tricubic Spline

The smoothed energy and covariance matrix element distributions are translated into functions by means of a three dimensional cubic spline interpolation, or tricubic spline. Cubic spline interpolation[54] is a method of approximating a distribution by a series of cubic functions. Because a cubic is used, the function and its first derivative are smooth and its second derivative is continuous. This is precisely the requirement necessary for a numerical minimization program to accurately and quickly locate the

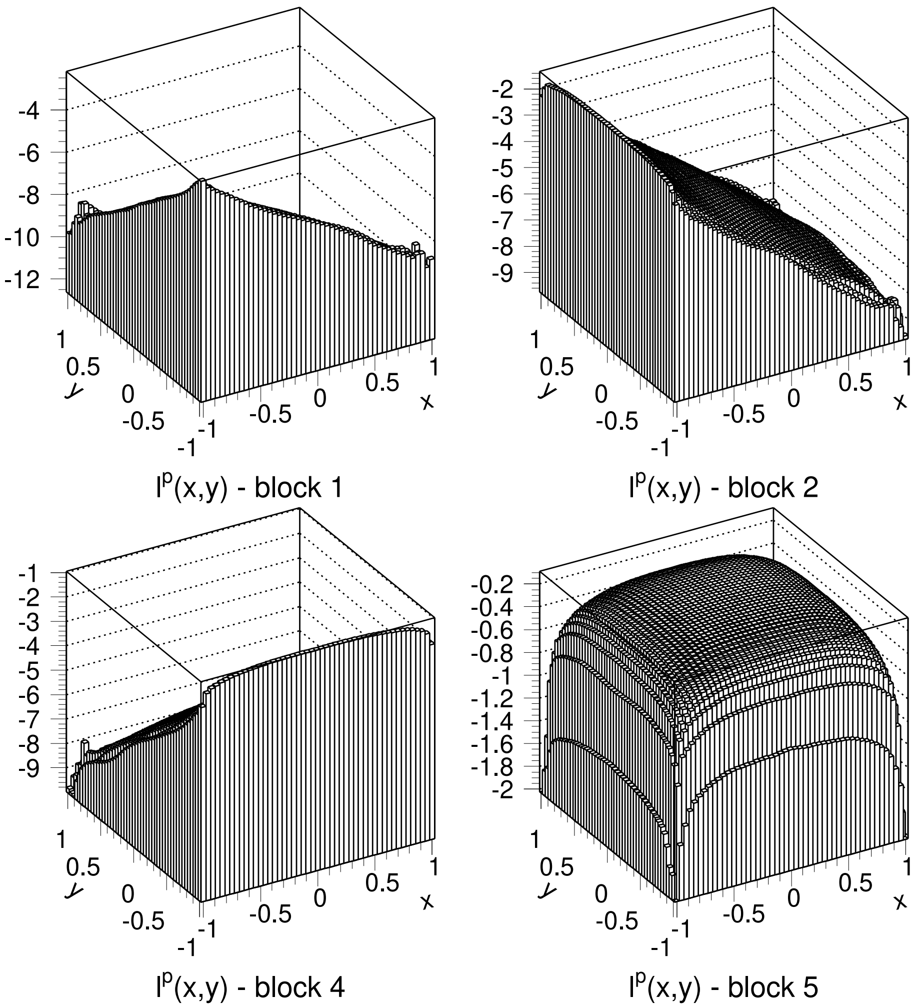

Figure 6.7: Predicted shower log energy distributions for 1 GeV showers in the large block array for blocks 1, 2, 4 and 5.

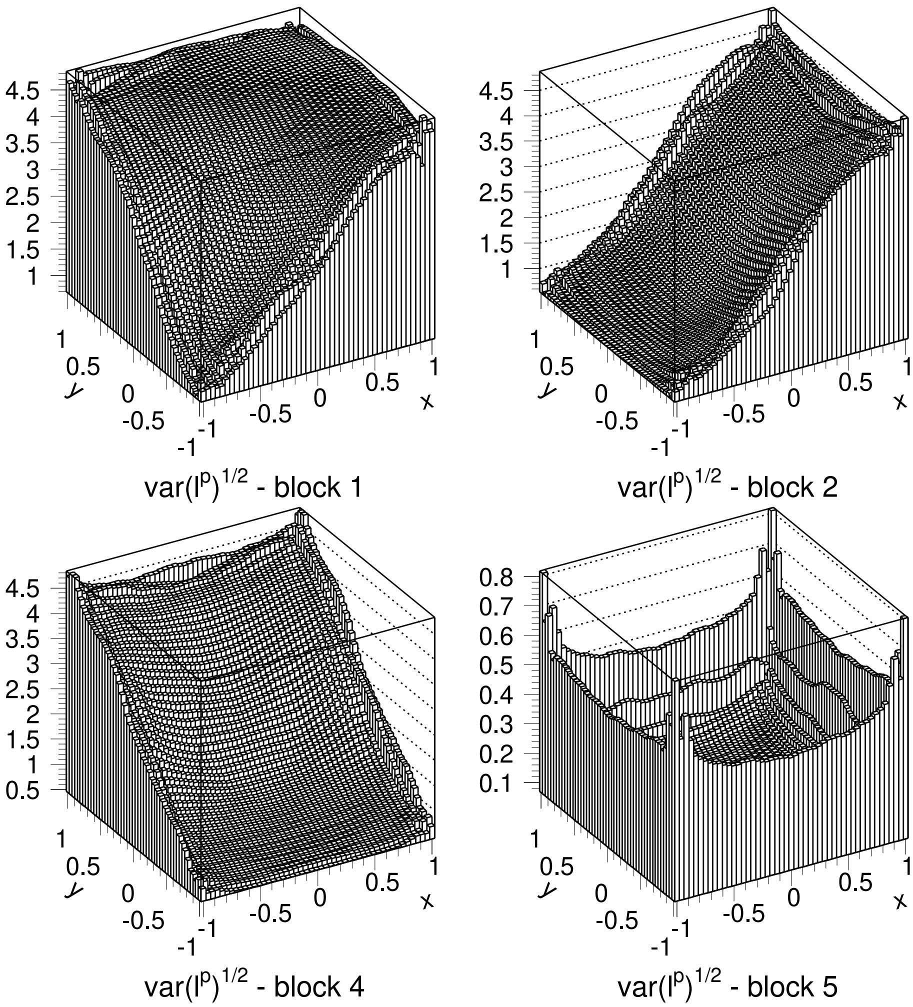

Figure 6.8: Variance of the predicted shower log energy distributions for 1 GeV showers in the large block array for blocks 1, 2, 4 and 5.

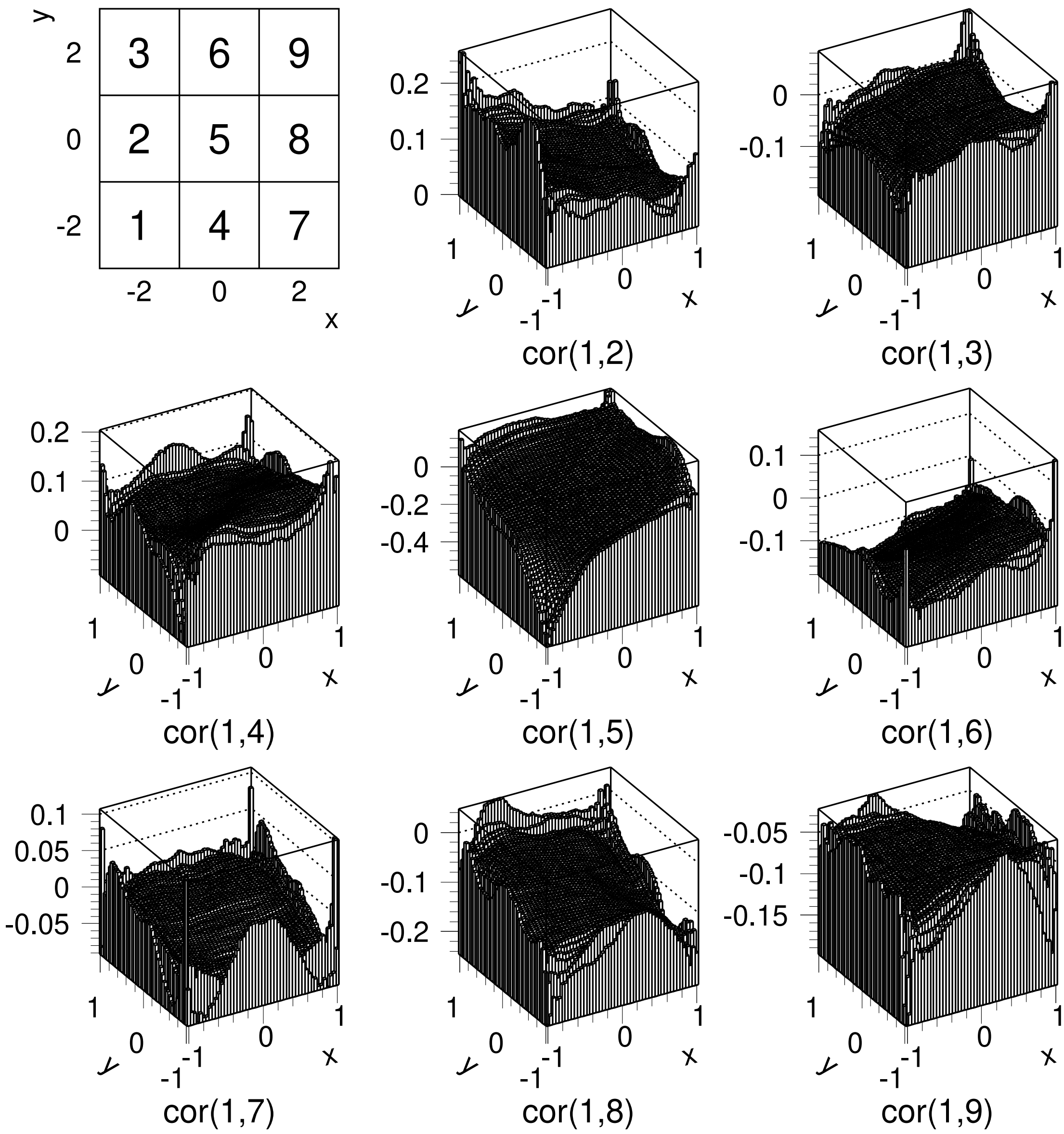

Figure 6.9: Correlation coefficient distributions for 1 GeV showers in the large 3×3 grid.

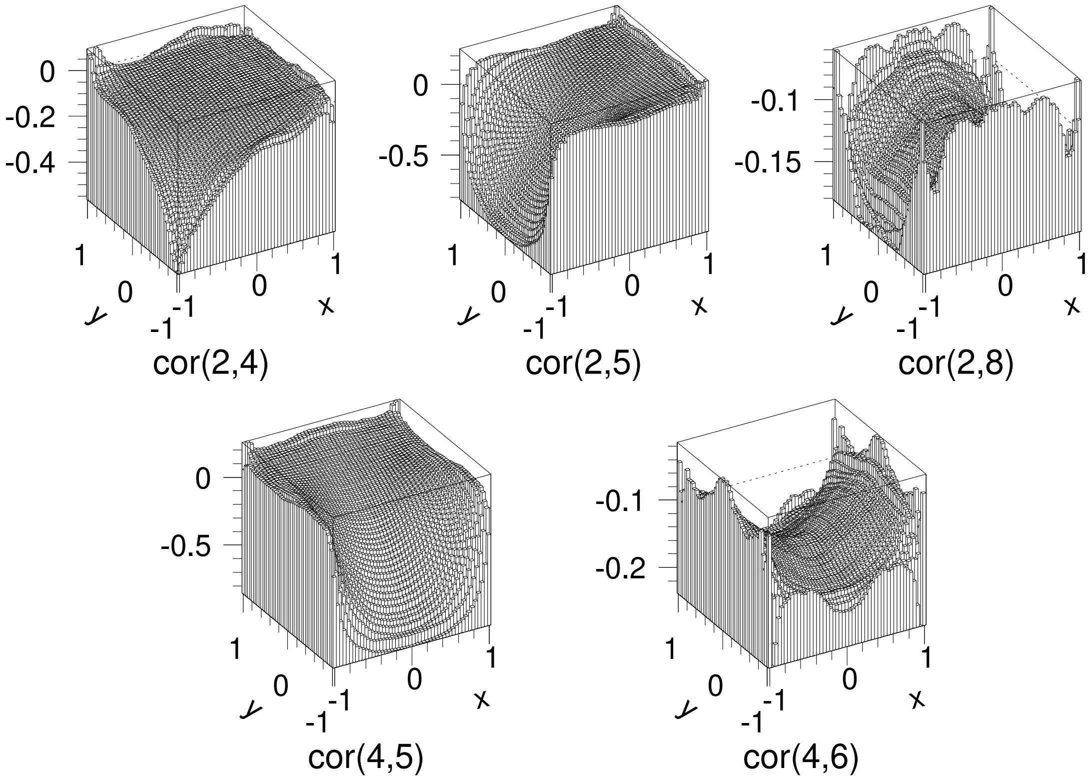

Figure 6.10: Correlation coefficient distributions for 1 GeV showers in the large 3×3 grid.

minimum of a function.

For tabulated function of one variable $f_i = f(x_i)$, $i = 1...N$, the value of $f(x)$ in interval $x_i < x < x_{i+1}$ can be approximated as

$$f(x) = Af_i + Bf_{i+1} + \frac{1}{6}(A^3 - A)(\Delta x)^2 f_i'' + \frac{1}{6}(B^3 - B)(\Delta x)^2 f_{i+1}'', \tag{6.4}$$

$$A = \frac{x_{i+1} - x}{\Delta x}, \tag{6.5}$$

$$B = \frac{x - x_i}{\Delta x}, \tag{6.6}$$

$$\Delta x = x_{i+1} - x_i. \tag{6.7}$$

The second derivatives f_i'' are determined numerically.

The cubic spline can be generalized to three dimensions by a series of one dimensional spline interpolations. Because the spline is a cubic, its second derivative has the form $f''(x) = mx + b$. The second derivative at any point in the domain $x_i < x < x_{i+1}$ can be obtained by linear interpolation. When the method is expanded to three dimensions, the approximation is made that all three of the second derivatives can be obtained by linear interpolation in each of the three dimensions, not only the dimension of the derivative. For example, in figure 6.11, the second derivative with respect to x at point (x_i, y, z_k) is estimated to be

$$\frac{\partial^2 f(x_i, y, z_k)}{\partial x^2} = \left(\frac{y_{j+1} - y}{\Delta y}\right) \frac{\partial^2 f(x_i, y_j, z_k)}{\partial x^2} + \left(\frac{y - y_j}{\Delta y}\right) \frac{\partial^2 f(x_i, y_{j+1}, z_k)}{\partial x^2}. \tag{6.8}$$

This method effectively ignores the mixed second derivatives ($\frac{\partial^2 f}{\partial x \partial y}$, $\frac{\partial^2 f}{\partial x \partial z}$ and $\frac{\partial^2 f}{\partial y \partial z}$). Certainly this reduces the accuracy of the method, but recall that the purpose for using a tricubic spline is to provide a functional representation of a discrete data set. Any errors introduced by ignoring the contribution of the mixed derivatives is small compared with the statistical error in the estimation of the predicted log(energy) and covariance matrix element distributions. Inclusion of the mixed derivatives would not improve the performance of the cluster fitting algorithm.

The procedure for estimating the value of function f at point (x, y, z) proceeds as follows (See figure 6.11):

- Determine f using spline interpolation at points (x_i, y, z_k), (x_i, y, z_{k+1}), (x_{i+1}, y, z_k) and (x_{i+1}, y, z_{k+1}),
- Determine f_{xx} and f_{zz} by linear interpolation at points (x_i, y, z_k), (x_i, y, z_{k+1}), (x_{i+1}, y, z_k) and (x_{i+1}, y, z_{k+1}),
- Use results from first two steps to obtain f by spline interpolation at points (x, y, z_k) and (x, y, z_{k+1}),
- Determine f_{zz} by linear interpolation at points (x, y, z_k) and (x, y, z_{k+1}),
- Use results of previous two steps to determine $f(x, y, z)$ by spline interpolation.

Tricubic spline interpolation is used to estimate l_i^p and $\mathbf{M_{ij}}$ as a function of the three shower parameters (E,x,y). The second derivatives with respect to E, x and y for the four predicted log(energy) distributions, the four associated variances and the 13 unique correlation coefficient distributions are estimated numerically and saved in an array along with the functional values at each point. The array is of dimension $9 \times 49 \times 49 \times 21 \times 4 \times 2$ for 9 block energies, a 49×49 spatial grid, 4 unique block positions + 17 unique covariance matrix elements, function value + 3 derivatives, and 2 block sizes. With each number consuming 4 bytes, the entire array is 14.5 Mbytes. This is not a small array size by any means, but modern computers have no problem handling it. However, expanding the simulation to use the 20 CCAL block shapes (instead of approximating the intermediate sizes by linear interpolation of the small and large block simulations) would increase the array size by a factor of 10. Computers used for high energy physics analysis are not typically equipped with enough memory to deal effectively with arrays in excess of 100Mb.

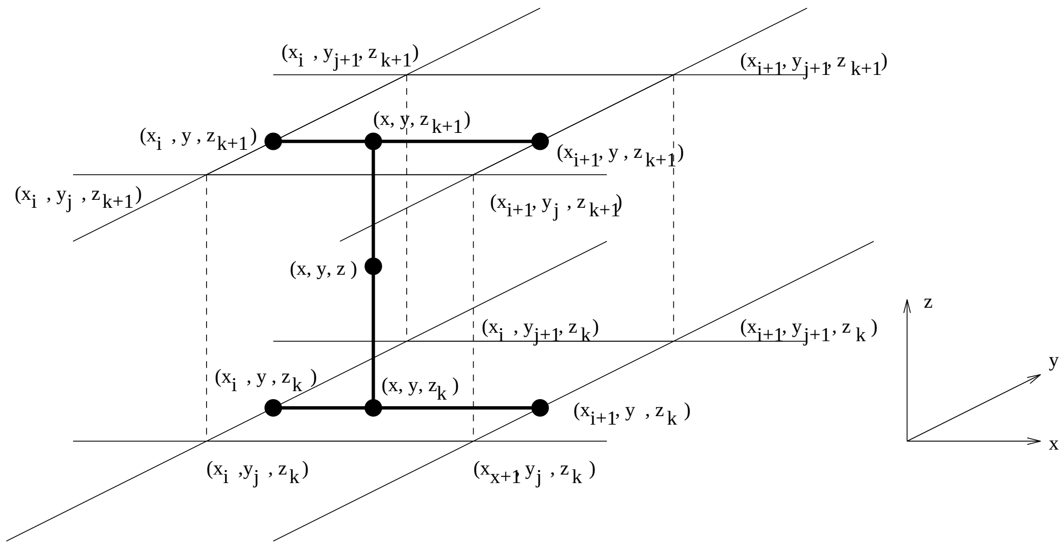

Figure 6.11: Diagram of tricubic spline interpolation.

6.2.4 Fitting

With tricubic spline interpolation, the functions $l_i^p(E,x,y)$ and $\mathbf{M}_{ij}(E,x,y)$ are estimated. For each hypothetical shower energy and position, (E,x,y), the contributions from non-correlated errors are added to the diagonal elements of the covariance matrix. The non-correlated errors include measurement errors due to the limited number of photoelectrons detected by each PMT, the uncertainty in the CCAL gain constants, and the precision of the ADC. The covariance matrix is then inverted and χ^2 is calculated. The minimum value of $\chi^2(E,x,y)$ is obtained numerically with the MINUIT [55] functional minimization program. MINUIT locates the minimum value of χ^2 and uses the curvature of $\chi^2(E_{min},x_{min},y_{min})$ to estimate the covariance matrix of the fit parameters.

Because the calculation of χ^2 is performed using the logs of the measured energies, blocks with zero measured energy must be handled specially. Blocks that record no signal cannot be said to have zero energy, but rather the energy deposited in those blocks can only be said to be below the detection threshold. Prior to the calculation of χ^2, measured block energies below threshold are set to be equal to the threshold energy. If both the predicted and measured energies are below the block threshold, both the predicted and measured energies are set equal to the block threshold energy. Nothing can be deduced about the consistency of the measurement when both predicted and measured energies are below threshold, so the block is effectively excluded from the calculation.

The fitter fails to find a minimum for only 0.2% of the clusters.

6.3 Results

The shower fitter was tested using simulated showers generated by the CCAL Monte Carlo simulation described in the previous chapter. Figures 6.12 and 6.13 show the energy and position resolution for reconstruction of 3 GeV showers in rings 10 and 19. Rings 10 and 19 were chosen because they represent the extremes in CCAL block sizes. The reconstructed shower energies and positions for the cluster fitting algorithm and the offline cluster reconstruction algorithm are compared. Also shown are the position and energy errors reported by the cluster fitting algorithm.

The energy resolution of the cluster fitting algorithm is comparable to the offline. There is a tendency for the cluster fitter to overestimate the energies of showers near the block boundary. This effect is due to a small systematic error introduced by the smoothing algorithm. The expected energy in the central block has a sharp decline for showers centered at the block boundaries. The smoothing causes the decline in shower energy to be averaged over a wider area, reducing the expected energy distribution for showers centered near the boundary and increasing the expected energy for showers centered at the boundary. Reducing the smoothing can eliminate the effect, but will also reduce the speed and efficiency of the cluster fitting program. The energy error estimated by the cluster fitting program is a good approximation of the measured energy resolution, for showers in block 10, but overestimates the energy error for showers in block 19.

The angular resolution of the shower fitter is comparable, and in some regions superior, to the resolution of the offline algorithm. Both methods reproduce the shower position with minimal systematic offset. The angular error calculated by the cluster fitter slightly underestimates the measured resolution.

The application of the cluster fitting algorithm to low energy showers is problem-

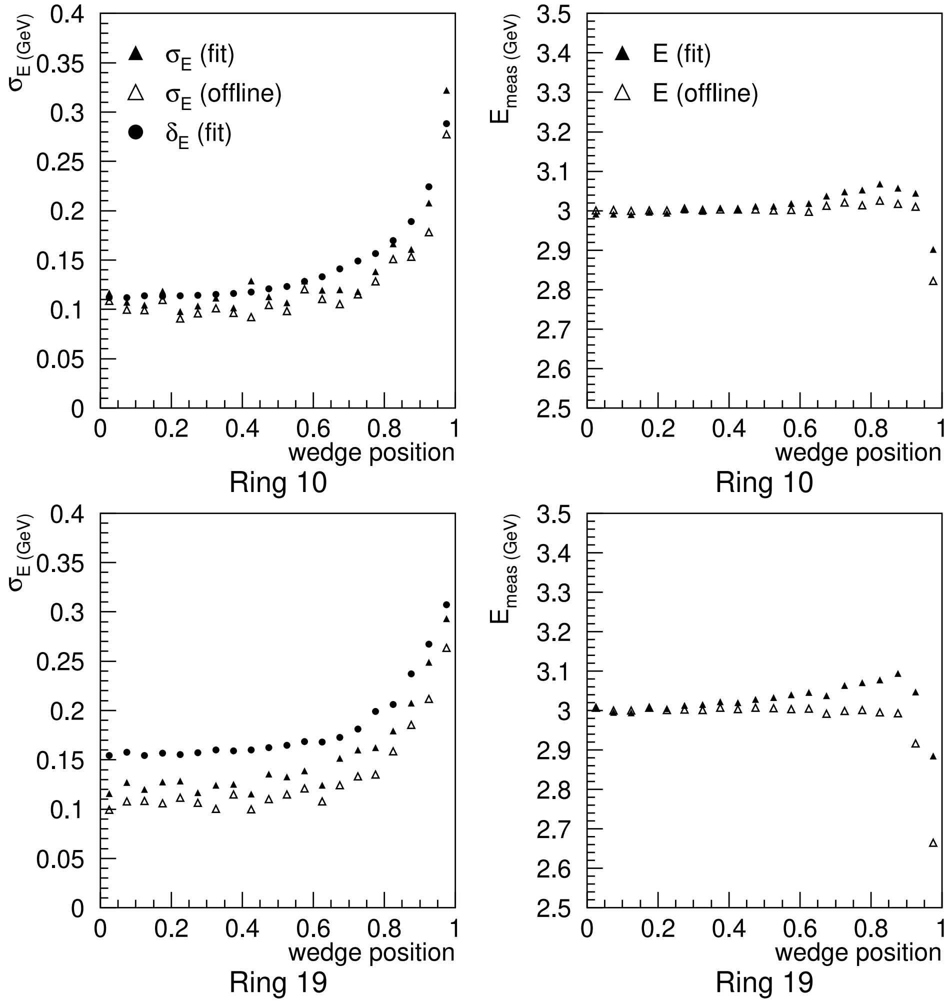

Figure 6.12: Comparison of cluster fitting algorithm with the offline reconstruction algorithm. The energy resolutions and the average measured energies for simulated 3 GeV showers are plotted as a function of wedge position. Wedge position 0 represents the block center, and wedge position 1 represents the block boundary in the azimuthal direction.

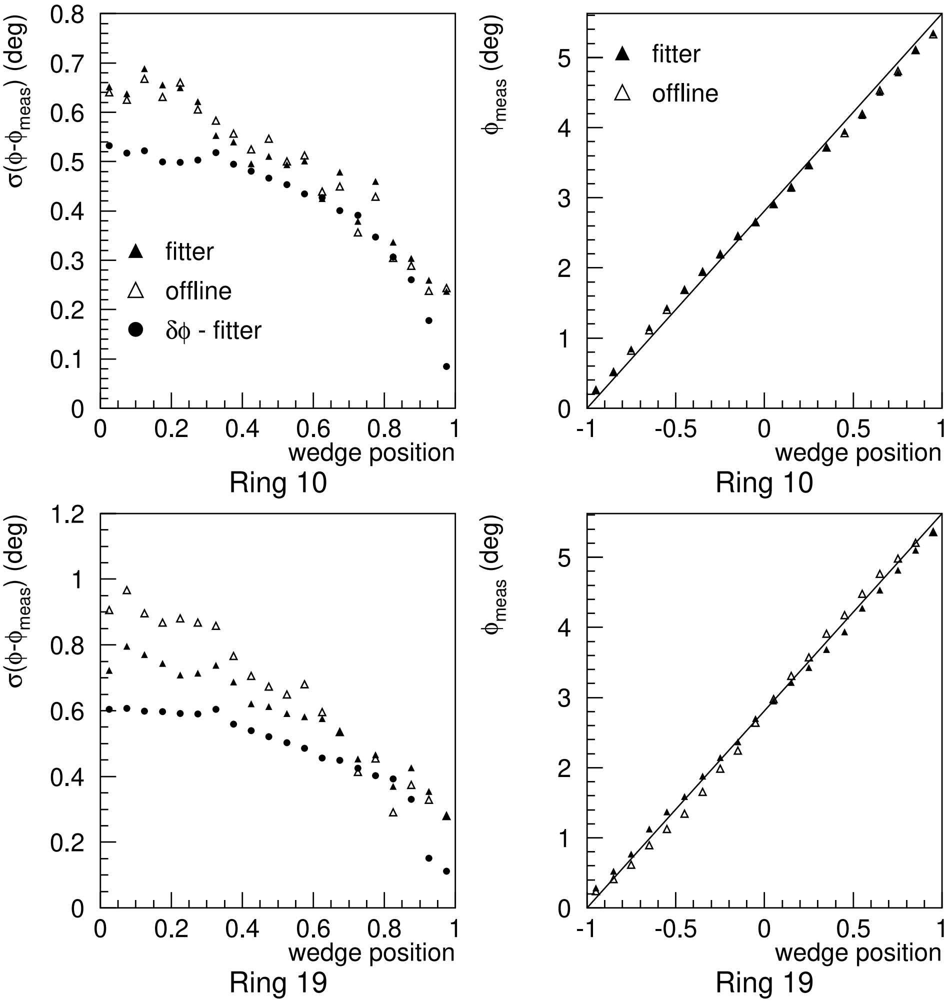

Figure 6.13: Comparison of cluster fitting algorithm with the offline reconstruction algorithm. The σ_ϕ and ϕ for simulated 3 GeV showers are plotted as a function of wedge position. Wedge position 0 represents the block center, and wedge position 1 represents the block boundary in the azimuthal direction.

atic. Low energy showers typically only deposit energy in one or two blocks. It is usually possible for the minimization routine to locate a set of parameters (E,x,y) for which the χ^2 goes to zero. This is possible because blocks with both measured and predicted energies below threshold are effectively eliminated from the χ^2 calculation. If six of the nine blocks can be eliminated, and three or fewer points contribute to the fit, then the fit is underconstrained, and χ^2 can shrink to zero. If fewer than three measurements contribute to the χ^2, then a range of (E,x,y) points can produce a zero χ^2. In such cases, the curvature of the χ^2 function near the minimum is zero and therefore the estimates of the errors in the fit parameters diverge. This result is not unexpected. After all, if a 100 MeV deposit is detected in a single block with all the surrounding blocks recording no measured energy deposits above their thresholds, all shower positions away from the block boundaries are of roughly equal likelihood. The position of such showers is effectively unmeasured. The same is not true for a large energy shower that is recorded by a single block. For large energy showers, the expected energy deposited in the surrounding blocks is above the block thresholds making it possible to include the contributions from the surrounding blocks in the calculation of χ^2. In the case that a high energy shower is only detected by a single block, the position of the shower can be quite well constrained to the block center. Figure 6.14 shows the 1 sigma contours for a cluster containing only a single hit block for a variety of measured energies. The 100 MeV deposit is merely restricted to be centered somewhere in the central block, while the 1.5 GeV deposit is constrained to be near the block center.

For showers near block boundaries, the shower position errors deduced from the curvature of the χ^2 function at the minimum are typically not accurate. In fact, there is no way for them to be accurate, because the position errors for showers near block boundaries are highly asymmetric. Figure 6.15 shows the 1 sigma contour plot for a

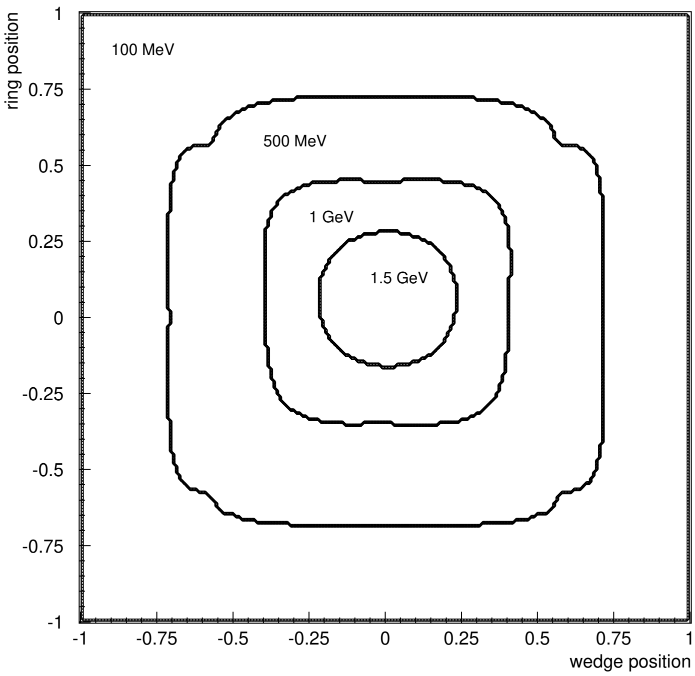

Figure 6.14: Plot of 1 sigma contours for clusters with only one hit block.

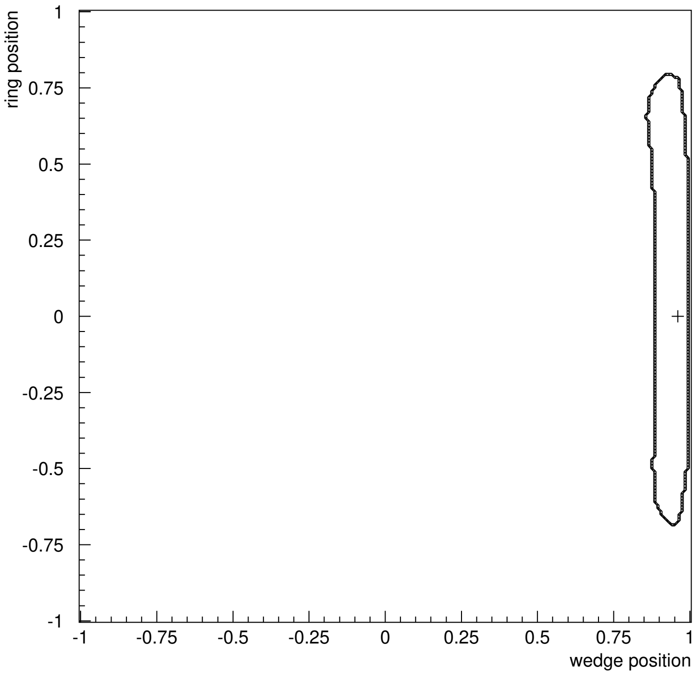

Figure 6.15: The probability contour for a simulated shower near a block boundary. Deposits of 450 MeV and 50 MeV are simulated in the central block and in a block in an adjacent wedge respectively. The (+) indicates the position for which the χ^2 is a minimum, and the contour is the 1 sigma probability contour where the energy is held constant and equal to the energy at the minimum χ^2.

typical medium energy shower near a block boundary. In this case, the central block contains a 450 MeV deposit and a single edge block contains 50 MeV. The + indicates the best estimate of the shower center. The contour extends more than twice as far to the left as to the right from the best estimate of the shower position. In cases such as this one, the position measurement is highly asymmetric and it is unreasonable to expect that the shower position error could be represented by a single variance.

Figure 6.16 is a plot of the correlations between the energy and position measurements plotted vs the position of the shower in the ring and wedge directions for simulated 3 GeV showers in rings 10 and 19. The correlation between energy and ϕ is

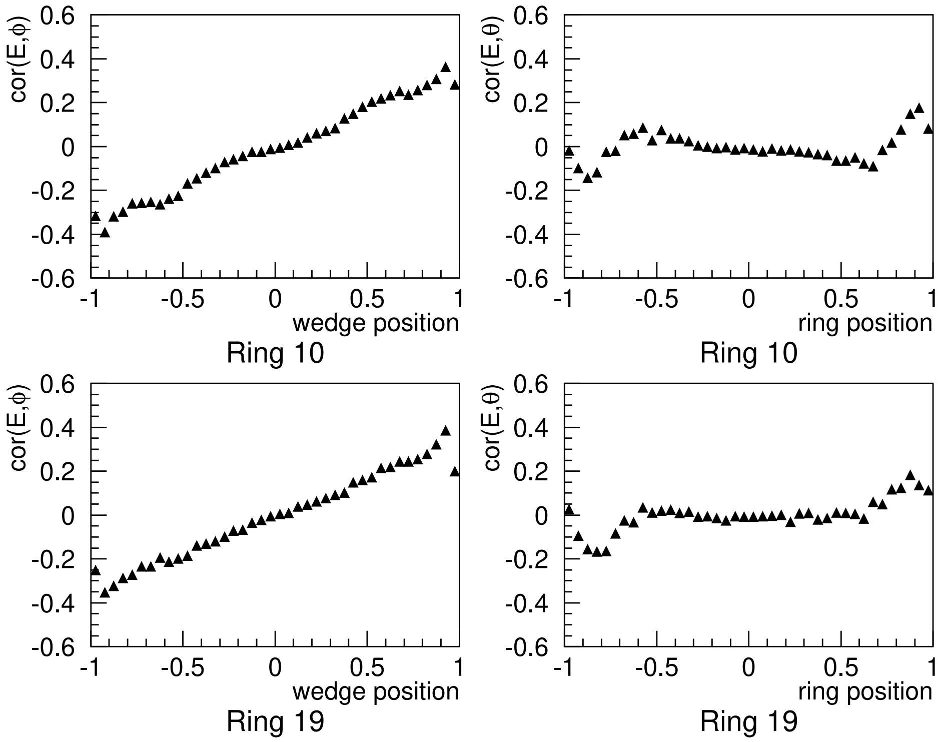

Figure 6.16: Correlation coefficients between measured energies and angles. Block positions -1 and 1 represent block boundaries, and block position 0 represents the block center. In the azimuthal direction, larger wedge position represents a larger value of ϕ. In the ring direction, a larger ring position represents a smaller value of θ.

large near the wedge boundaries. The effect is much smaller near the ring boundaries, but a correlation is still present. The offline cluster reconstruction algorithm makes no estimate of correlations between the angles and the energies.

As mentioned in section 2, the offline algorithm does a poor job estimating the energies and positions for showers near the edge of the CCAL volume. Figure 6.17 shows the reconstructed energy and position distributions for the cluster fitter and the offline algorithm for showers in block 20. The offline algorithm severely mismeasures both the energy and position of showers in block 20. The shower fitter shows smaller systematic offsets, and seriously mismeasures energy and position only for those

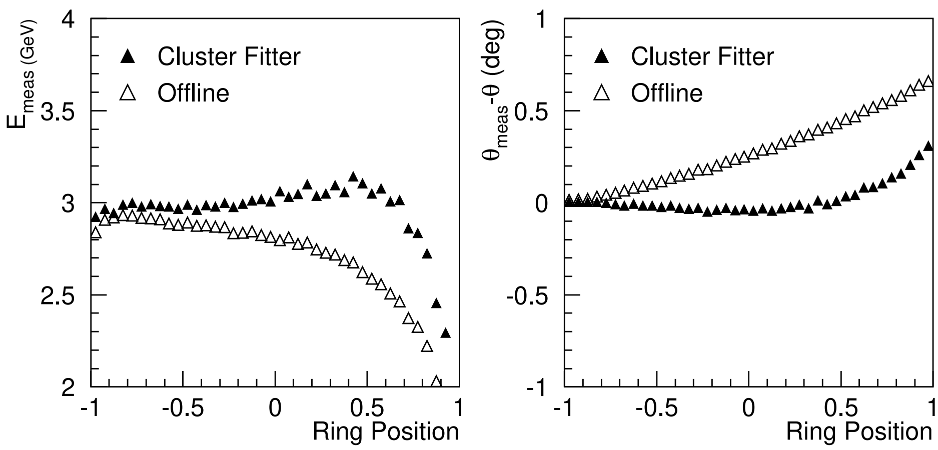

Figure 6.17: Comparison of the offline cluster algorithm and the cluster fitter for simulated 3 GeV showers in ring 20. Ring position -1 is the boundary between rings 19 and 20 and ring position 1 is the edge of the CCAL volume.

showers near the edge of the detector. The simulation estimates the expected energy detected by the blocks in the cluster as if the region beyond ring 20 were lead glass. The region is empty, so the energy absorbed by the CCAL is overestimated, because there is no back scattering. This overestimate leads to the observed deviation from the expected energy and position for showers near the edge of the detector.

6.4 Conclusions

Although this method has a number of attractive features, there are still several problems that need to be overcome before it would be practical to use this method on data.

It is not clear to what degree approximating the twenty uniquely shaped blocks that populate the CCAL with two simplified 3×3 arrays limits the accuracy of the shower reconstruction algorithm. The staggering of the blocks in the central part of the detector is not accounted for. The actual CCAL blocks are not rectilinear, they are frustra and taper outward from their block faces. Unfortunately, a more accurate simulation of the error matrix is beyond the reach of available computing resources.

The algorithm is too slow for use on large data sets. The evaluation of a 3×3 block grid containing a single shower takes approximately 1 second on a 100 SPECfp92 computer. An event with several clusters might take as long as 5-10 seconds to reconstruct. This is too slow to be practical for an experiment that collects millions of events. The inversion of the covariance matrix constructed for each hypothesis is the slowest step in the reconstruction process, and there is no foreseeable way to speed it up significantly.

Low energy showers and showers near block boundaries have complex probability contours. There is no way to represent such showers accurately by a simple best estimate for (E,x,y) and the covariance matrix in the three fit parameters. This limitation is inherent to the cluster reconstruction process. There is no getting around it.

This algorithm lacks the facility for reconstructing overlapping showers. Even if the covariance matrix for a two shower system could be estimated somehow, the process of inverting the larger error matrix would be so slow as to make the method unfeasible.

Chapter 7

Measurement of Select decays of ψ'

In this chapter a measurement of the angular distributions of ψ' and J/ψ decays formed in $\bar{p}p$ annihilation is described. Additionally, new measurements of $Br(\psi' \to e^+e^-)$, $Br(\psi' \to J/\psi\pi^+\pi^-)$, $Br(\psi' \to J/\psi\pi^0\pi^0)$ and $Br(\psi' \to J/\psi\eta)$ are reported.

7.1 The Data

During two separate running periods in 1990 and 1991, experiment E760 recorded approximately 8000 J/ψ decays and 3000 ψ' decays. During the 1990 running period, the J/ψ and ψ' were revisited several times, while the 1991 data comes entirely from two resonance scans. Tables 7.1 and 7.2 lists the number of events collected and the integrated luminosity collected at each resonance. In addition to data collected at the energy of the ψ' resonance, data were collected away from the ψ' to provide an estimate of backgrounds.

7.2 Data Filtration

In the charged trigger, "tracks" are reconstructed from hit patterns in hodoscopes H1 and H2. The hodoscopes cannot measure the incident charged particle's polar

Resonance	E_{CM} (MeV)	$\int \mathcal{L}dt$ (nb^{-1})	N_{events}
J/ψ (1990)	3095-3098	260	≈4000
J/ψ (1991)	3095-3098	661	≈4000

Table 7.1: J/ψ and background event samples.

Resonance	E_{CM} (MeV)	$\int \mathcal{L}dt$ (nb^{-1})	N_{events}
ψ' (1990)	3685-3687	1494	≈1600
ψ' background (1990)	3655	184	
ψ' (1991)	3685-3687	995	≈1200
ψ' background (1991)	3667	299	

Table 7.2: ψ' and background event samples.

angle. There is no way, at the trigger level, to determine which of two Čerenkov counter cells, upstream or downstream, is associated with the detected track. For this reason, trigger logic is designed to "OR" the two cells. Offline, a complete event reconstruction is performed. Using data from the calorimeter and the tracking chambers, the polar angles of the electron candidates are measured. In each event, the two tracks contained by the central calorimeter that form the highest invariant mass are considered electron candidates. Events with electron candidate tracks contained by the high efficiency regions of the Čerenkov counter, $\theta \in [15^o, 33^o]$ and $\theta \in [39^o, 60^o]$, that are not found to be associate with a Čerenkov counter hit are removed from the sample used in this analysis. In addition to the Čerenkov counter association selection requirement, loose cuts are made on the electron candidate coplanarity ($||\phi_1 - \phi_2| - \pi| < 1.0$ rad), the center of mass frame polar angle, ($||\theta_1^* - \theta_1^*| - \pi| < 1.0$ rad) and the invariant mass of the candidates ($M_{12} > 2.2\frac{GeV}{c^2}$). The efficiency of the filter was determined to be 0.974 ± 0.003 in the 1990 data sample and 0.987 ± 0.002 in the 1991 data sample. The filter efficiency does not vary between channels.

7.3 Electron Weight

In this experiment 4 detector subsystems, CCAL, Threshold Čerenkov, H2 and the RPC, provide independent information that can be used to distinguish J/ψ and ψ' decays to e^+e^- from background. The electron weight[56] (ELW) is a statistical quantity developed by this experiment to provide a single variable to discriminate between signal and background. ELW is defined as

$$ELW \equiv \prod_{i=1}^{6} \frac{f_i^{el}(x_i)}{f_i^{bkg}(x_i)}. \tag{7.1}$$

In this equation f_i^{el} is the distribution function (d.f.) for real electron tracks for detector subsystem measurement i, and f_i^{bkg} is the d.f. for background tracks. The 6 variables utilized by the electron weight are:

- $\frac{dE}{dx}$ measured by the RPC.
- Čerenkov pulse height corrected to give uniform response in θ.
- H2 pulse height corrected to give uniform response in θ.
- Second moment of CCAL energy deposition in ring direction.
- Second moment of CCAL energy deposition in wedge direction.
- Shower Containment: Ratio of energy in 3x3 block region and 5x5 block region.

Plotted in figure 7.1 are the ratios of the d.f.'s for the signal and background data samples that are used in the evaluation of ELW. J/ψ and χ_2 events, cleanly selected with only topological cuts, are used to evaluate the signal d.f.'s. A sample of triggers from the search for the $^1P_1$ state of charmonium were used to estimate the d.f.'s for the background. In the region of the $^1P_1$, the rate for the process $\bar{p}p \rightarrow e^+e^-X$ is low, so the background can be cleanly measured. Figures 7.2 and 7.3 show the product of

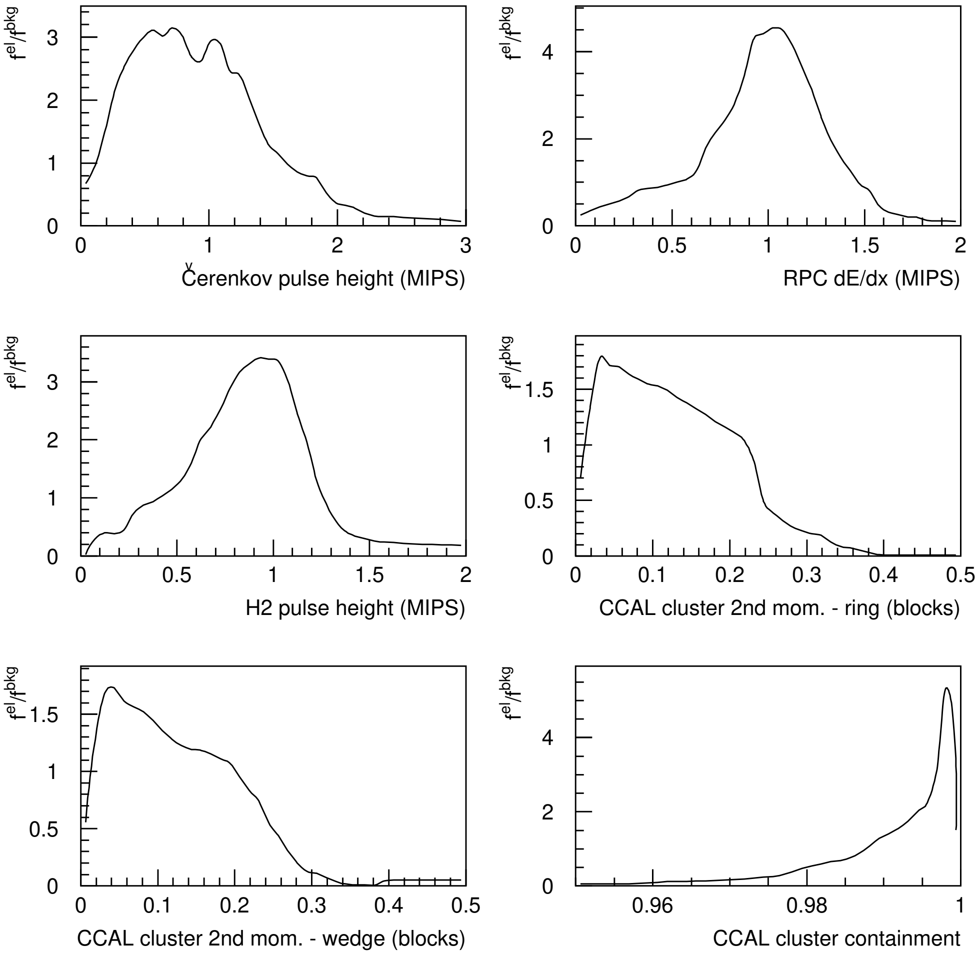

Figure 7.1: Ratio of the distribution functions for electrons and background for the 6 variables that contribute to the electron weight (ELW). The Čerenkov, RPC and H2 signals are normalized to a single minimum ionizing electron track (MIP) and the 2nd moments are given in CCAL block units.

the ELW's for the 2 electron candidate tracks for the J/ψ and ψ' data samples. Also shown are the ELW product distributions for background data scaled to represent equal luminosity as in the signal. For the J/ψ, the background contamination is estimated from data collected in the region of the η_C. For the ψ' the background

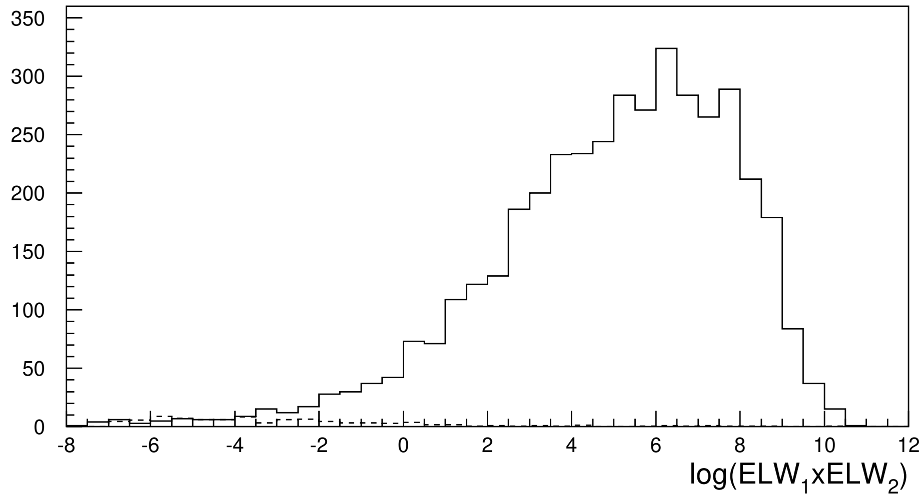

Figure 7.2: Log of the product of the electron weights of the electron track candidates from the 1991 J/ψ resonance scan (solid line) and an off resonance background sample (dashed). The background sample has been scaled to represent an equal luminosity to the signal.

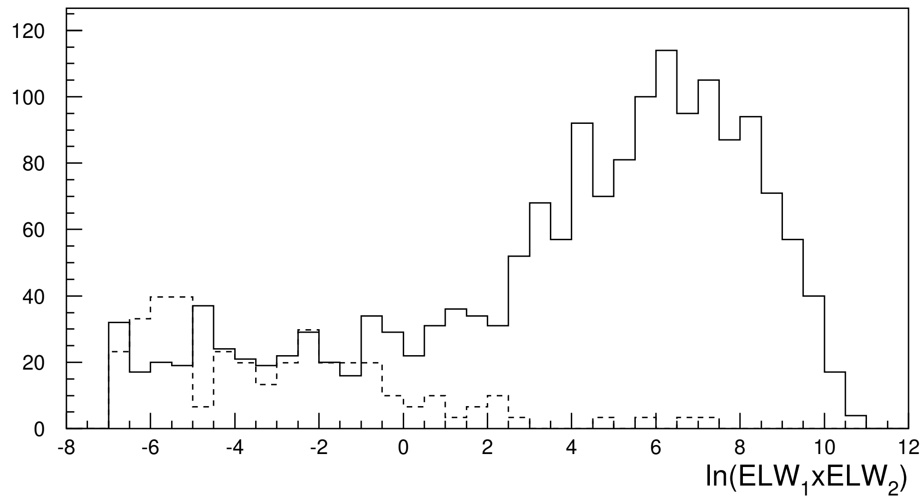

Figure 7.3: Log of the product of the electron weight of the electron track candidates from the 1991 ψ' resonance scan (solid line) and an off resonance background sample (dashed). The background sample has been scaled to represent an equal luminosity to the signal.

estimate is from the ψ' background point. The background samples have been scaled by the ratio of the luminosities to represent the background contribution in the data samples. These data samples include all events collected through the 1 and 2 Čerenkov triggers that have an electron pair mass in excess of $2.75\frac{GeV}{c^2}$ and with electron tracks confined to $\theta^{lab} \in [15^0, 60^0]$. Notice that it is not possible to eliminate the background by cutting on ELW without compromising the efficiency of selection for the ψ' events, but, because of the much higher cross section, J/ψ events can be selected with high efficiency and almost no background contamination.

7.4 Measurement of $\lambda_{J/\psi}$ and $\lambda_{\psi'}$

As shown in chapter 2, the angular distributions of leptonic decays of J/ψ and ψ' are determined entirely by the ratio of formation helicity amplitudes from $\bar{p}p$, $\frac{C_0^2}{C_1^2}$, denoted by λ. The angular distribution of ψ' decays to $J/\psi\pi\pi$ (approximately 90% of all $\psi' \to J/\psi X$ decays) are also described by $\lambda_{\psi'}$ if the $\pi\pi$ system has l=0 and the ψ' decay to $J/\psi(\pi\pi)$ is s-wave. High statistics studies of $\psi' \to J/\psi\pi\pi$ by e^+e^- collider experiments have demonstrated that the $\pi\pi$ system's angular distribution and mass spectrum is consistent with pure s-wave [36]. Figure 7.4 is a plot of M_X for events from the 1991 ψ' data sample selected with a 1c kinematical fit to the reaction $\psi' \to J/\psi X \to e^+e^-X$. In the fit M_X is the mass recoiling against the J/ψ in the ψ' decay. The plotted distribution is the best estimate of M_X reported by the fit. Overlayed on the plot is the distribution

$$\frac{dN}{dM_X} \propto (M_X^2 - 4M_\pi^2)^2 (M_X^2 - 4M_\pi^2)^{\frac{1}{2}} \left[(M_{\psi'}^2 - M_{J/\psi}^2 - M_X^2)^2 - 4M_{J/\psi}^2 M_X^2 \right]^{\frac{1}{2}}. \quad (7.2)$$

This distribution [57] is the predicted $\pi\pi$ mass distribution for a s-wave $\pi\pi$ system. Figure 7.5 is a plot of the angular distribution of the J/ψ for the process $\psi' \to J/\psi X$.

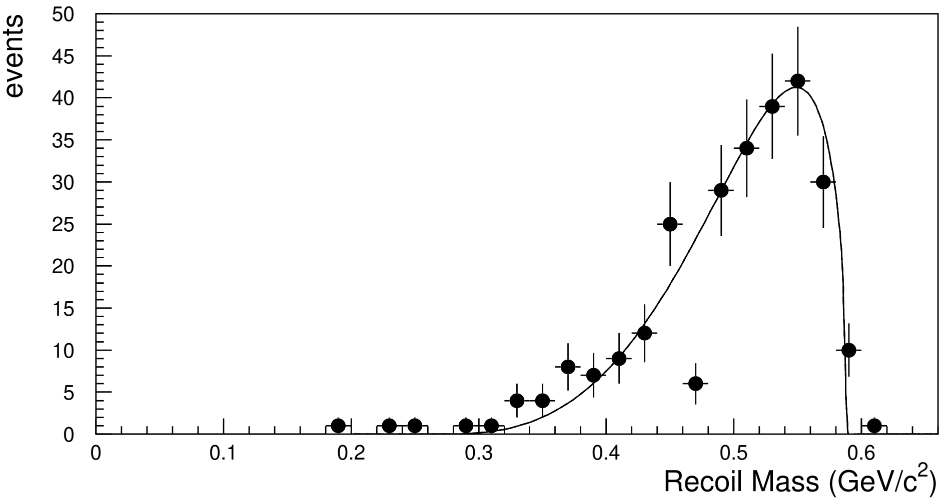

Figure 7.4: Mass recoiling against J/ψ for events from the 1991 ψ' data sample selected by kinematical fit to the process $\psi' \to J/\psi X \to e^+e^-X$.

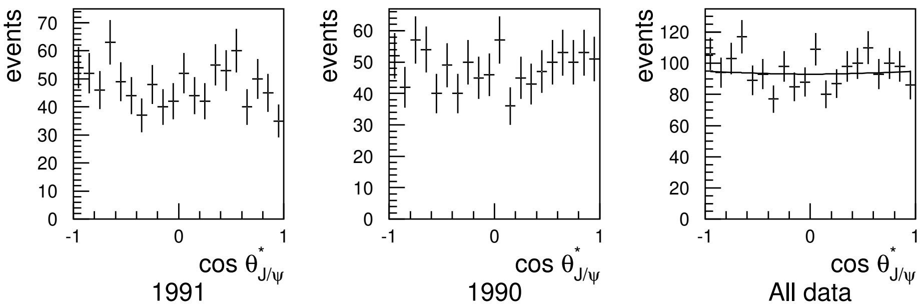

Figure 7.5: Angular distribution of J/ψ produced in ψ' decays to $J/\psi X$.

Both the 1990 and 1991 distributions are flat. The combined distribution was fit to the function $1 + \alpha cos^2\theta^*_{J/\psi}$. α was determined to be -0.027 ± 0.030, consistent with an isotropic, s-wave, ψ' decay. For the purposes of measuring the angular distribution of inclusive ψ' decays, the ψ' decay to $J/\psi X$ is assumed to be isotropic, and the J/ψ is assumed to carry away the polarization of the ψ'.

The trigger simulation provides an accurate representation of the efficiency of the detector for the various J/ψ and ψ' decay channels as a function of the e^+ CMS polar angle θ^*. In this experiment, however, no distinction can be made between e^+ and e^-; therefore, $\cos\bar{\theta}^* = \frac{|cos\theta^*_{e^+} - cos\theta^*_{e^-}|}{2}$ is used to describe the angular distributions. This is reasonable since parity conservation requires that the angular distributions are described by even functions. The ψ' events are separated by decay channel into 2 subsets, inclusive decays ($\psi' \rightarrow J/\psi X$) and exclusive decays ($\psi' \rightarrow e^+e^-$). Classifying the events in this way is required because the detection efficiencies differ between the two channels as a function of $\cos\bar{\theta}^*$.

None of the E760 detector subsystems are symmetric in the polar angle θ. Pulse heights from the hodoscopes and the Čerenkov counter and the resolution of the Central Calorimeter all potentially have $cos\bar{\theta}^*$ dependence. In order to avoid systematic error, stringent cuts are avoided. For example, selection of ψ' events with hard cuts on their electron signature in the inner detectors or χ^2 from kinematical fits to allowed final states can easily achieve signal to noise ratios of greater than 100 to 1, but this is achieved at the cost of a selection efficiency of about 80% overall and may be non-uniform in $cos\bar{\theta}^*$. The approach taken in this analysis is to select events in such a way that efficiency as a function of $cos\bar{\theta}^*$ is uniform and high. In the ψ' analysis, the background contamination is estimated from data collected off resonance and included in the likelihood fit.

7.4.1 Measurement of $\lambda_{J/\psi}$

The J/ψ event samples are selected with the following cuts,

- $\theta^{lab}_{e^+}$ and $\theta^{lab}_{e^-} \in [15^o, 60^o]$,
- $M_{ee} > 2.75 \frac{GeV}{c^2}$,

- $(ELW_{e^+} \times ELW_{e^-}). > 0.1.$

The electron candidate tracks are the tracks associated with the two CCAL showers that form the highest invariant mass.

3565 events pass these cuts in the 1990 data sample and 4027 events pass in the 1991 data sample. The background is estimated by applying the cuts to data taken off resonance. In 1991, substantial quantities of data were collected in the region of the η_c, η_c' and the h_c charmonium states. Application of the J/ψ event selection to these data sets gives a measurement of the background for the energies spanning the charmonium spectrum. The mass cut, $M_{ee} > 2.75\frac{GeV}{c^2}$, is substituted with $\frac{E_{CMS}}{c^2} - M_{ee} < .347\frac{GeV}{c^2}$ so that the selection is more accurately represented for the span of center of mass energies. Events that are kinematically consistent with the hypothesis $\bar{p}p \rightarrow e^+e^-$ are excluded from the background estimates. These events are indistinguishable from J/ψ decays. The E_{CMS} dependence of these events is well understood and so they are considered separately. In the 1991 data set, the background cross-section at the J/ψ is 10 ± 2 pb or 7 ± 2 events.

In 1990, the only substantial background sample was collected in the region of the center of gravity of the χ states, $E_{CMS} = 3.525$ GeV. The background cross-section in 1990 is 5 ± 2.0 times larger than in 1991. The energy dependence of the background is assumed to be the same for both running periods. The background cross-section in the 1990 J/ψ data sample is 50 ± 20 pb, or 14 ± 6 events. The background from direct non-resonant $\bar{p}p \rightarrow e^+e^-$ is 4 events in 1991 and 2 event in 1990. The total background contamination in both data samples is less than 1%.

The efficiency of the electron weight cut is estimated with a test sample selected by 4c kinematical fit to the hypothesis $\bar{p}p \rightarrow J/\psi \rightarrow e^+e^-$. 3380 events satisfy this selection criteria in the 1990 data sample and 3728 events are selected in the 1991

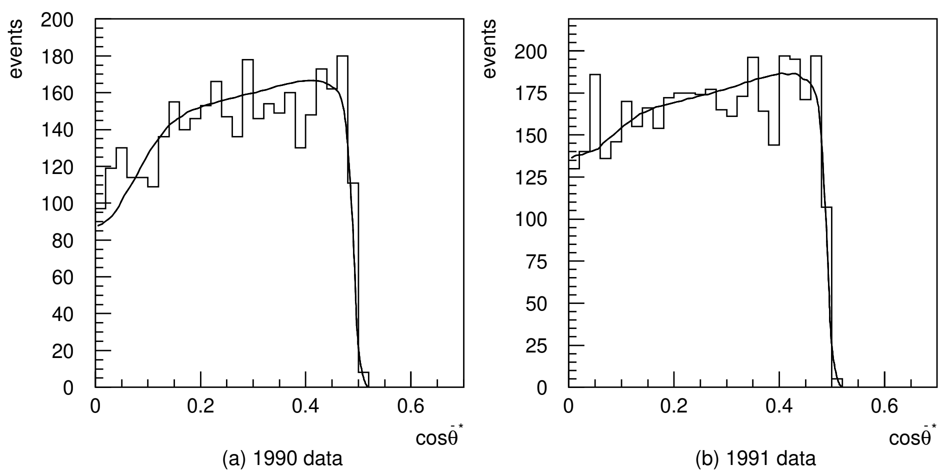

Figure 7.6: Angular distribution of the data for $J/\psi \to e^+e^-$. The solid line is the curve represents the best fit angular distribution multiplied by the detection efficiency.

data sample. From these samples, 3342 events pass the electron weight cut in the 1990 data for an efficiency of $98.9 \pm 0.2\%$, and 3679 events pass the cut in the 1991 data for an efficiency of $98.7 \pm 0.2\%$.

The best estimate of the parameter $\lambda_{J/\psi}$ is determined by the maximization of the likelihood function

$$lnL(\lambda_{J/\psi}) = \sum_{i=1}^{N_{events}} ln \frac{\varepsilon(cos\bar{\theta}_i^*)(1+\lambda_{J/\psi}cos^2\bar{\theta}_i^*)}{\int_0^1 \varepsilon(cos\theta')(1+\lambda_{J/\psi}cos^2\theta')d(cos\theta')} \tag{7.3}$$

In this equation, ε is the efficiency for detecting an event as a function of the decay angle of the electrons. Maximization of the likelihood for both data samples yields $\lambda_{J/\psi}(1990) = 0.86 \pm 0.27$, and $\lambda_{J/\psi}(1991) = 0.95 \pm 0.26$. Combining the two results gives

$$\lambda_{J/\psi} = 0.91 \pm 0.19. \tag{7.4}$$

Figure 7.6 shows the angular distributions of the two data sets. Overlayed on the figure is the curve that represents the best fit to the angular distribution multiplied by the detection efficiency.

7.4.2 Measurement of $\lambda_{\psi'}$

The cross-section for resonant formation and detection of the ψ' is smaller by about a factor of 10 compared to the J/ψ while the background rate at the ψ' resonance is about 3 times higher. Therefore, the ψ' event sample is contaminated by background at a much higher rate than the J/ψ sample. This contamination can be easily observed by examining figures 7.2 and 7.3. To account for the contributions made by the background to the angular distribution, a modified "likelihood" function is used to estimate $\lambda_{\psi'}$ that includes the measured background distribution.

The cuts applied to the ψ' data samples are

- θ_1^{lab} and $\theta_2^{lab} \in [15^o, 60^o]$.
- $M_{e^+e^-} > 2.75 \frac{GeV}{c^2}$.
- $(ELW_1 \times ELW_2) > 1.0$.
- Events collected through 1Č or 2Č triggers.

The 0Č trigger is excluded because fewer than 1 event is expected to be collected in each of the data samples through this trigger. The reason for this is purely kinematics. For ψ' decays, both inclusive and exclusive, if one electron is in the low efficiency Čerenkov septum region, the second electron is necessarily not in that region. Therefore, ψ' decays almost always contain at least one Čerenkov counter hit. The exclusion of the 0Č trigger reduces background without deteriorating the signal.

The ELW cut has been increased to 1.0 from 0.1 used to select J/ψ events. This modification was made to reduce the background contribution. The efficiency of the this cut was calculated using a clean sample of J/ψ events selected by kinematical fit. In the 1990 data the ELW cut efficiency was $95.1 \pm 0.4\%$ and in the 1991 data sample the ELW cut efficiency was found to be $95.0 \pm 0.4\%$.

In the 1990 data sample, 1379 events pass the cuts; 1308 pass these cuts in the 1991 data sample. The backgrounds are estimated by applying these cuts to the background data samples. 3 events are selected in the 1990 background sample which represents a luminosity corrected background contribution of 24 ± 14 events. In 1991, 5 events pass the selection criteria for a luminosity corrected background of 17 ± 7 events.

Exclusive ψ' decays are separated from the inclusive decays by kinematical fit probability. Events in the sample that fail both the 1C inclusive fit and the 4C exclusive fit are separated by electron pair mass using as the dividing line the mean of the J/ψ and ψ' masses. Events with $M_{e^+e^-} > 3.391\frac{GeV}{c^2}$ are identified as exclusive and events with $M_{e^+e^-} < 3.391\frac{GeV}{c^2}$ are identified as inclusive. In the 1990 data sample, 14 events failed both fits, and in the 1991 data only one event failed. No effort is made at this stage to identify specific inclusive decay channels.

As before with the J/ψ, the trigger Monte Carlo is used to produce efficiency distributions as a function of $cos\bar{\theta}^*$. These distributions when combined with the predicted form of the angular distribution, $1 + \lambda_{\psi'} cos^2\bar{\theta}^*$, give the probability distribution for both inclusive and exclusive decay channels. From these probability distributions a pseudo-likelihood function[58] is formulated by combining the product of the normalized probabilities for each event from the data samples, and dividing the result by the product of the normalized probabilities for each event in the background sample weighted in such a way as to compensate for the different amount of integrated luminosity collected at each point. The log of the pseudo-likelihood function is

$$lnL(\lambda_{\psi'}) = \sum_{i=1}^{N_{signal}} ln \frac{\varepsilon_{ch}(cos\bar{\theta}_i^*)(1+\lambda_{\psi'}cos^2\bar{\theta}_i^*)}{\int_0^1 \varepsilon_{ch}(cos\bar{\theta}')(1+\lambda_{\psi'}cos^2\bar{\theta}')d(cos\bar{\theta}')}$$
$$- \sum_{i=1}^{N_{back}} ln \frac{w\varepsilon_{ch}(cos\bar{\theta}_i^*)(1+\lambda_{\psi'}cos^2\bar{\theta}_i^*)}{\int_0^1 \varepsilon_{ch}(cos\bar{\theta}')(1+\lambda_{\psi'}cos^2\bar{\theta}')d(cos\bar{\theta}')}. \quad (7.5)$$

$$w = \frac{\int \mathcal{L}_{\psi'} dt}{\int \mathcal{L}_{back} dt} \quad (7.6)$$

ch identifies the channel inclusive or exclusive. The weighting factor w is required to compensate for the different amounts of integrated luminosity in the resonance scans and in the background region. Weighting the likelihood distribution in this fashion yields a maximum that represents the best estimate of $\lambda_{\psi'}$. But, unlike the standard likelihood method where the rms error in parameter $\lambda_{\psi'}$ can be estimated to be $(-\frac{\partial^2 lnL}{\partial\lambda_{\psi'}^2})^{-\frac{1}{2}}$, $\delta_{\lambda_{\psi'}}$ must be determined by an alternate method. In this analysis, the statistical error is estimated using simulated data sets with the same numbers of events observed in the data samples. The systematic error due to the unknown background contribution and angular distribution is estimated by varying the background distribution and observing the effect on the best estimation of the fit parameter $\lambda_{\psi'}$.

In this formulation, both the e^+e^- decays and the $J/\psi X$ decays are combined to produce a single estimate of $\lambda_{\psi'}$. This approach assumes that the angular distribution of the electrons from the J/ψ decay is described by $1 + \lambda_{\psi'}cos^2\bar{\theta}'$. This has been demonstrated to be true for the $J/\psi\pi\pi$ decays, but is certainly not true for the other J/ψ inclusive ψ' decays. About 10% of ψ' decays to J/ψ proceed through the channels $\psi' \to \chi\gamma \to J/\psi\gamma\gamma$ and $\psi' \to J/\psi\eta$. There is no way to cleanly separate the $J/\psi\pi\pi$ decays from the other channels, so the contamination is accepted. Monte Carlo studies have determined that the systematic error introduced by the contamination is an order of magnitude smaller than the statistical error in the measurement.

lnL is maximized w.r.t $\lambda_{\psi'}$. The best fit values for angular distribution parameters are $\lambda_{\psi'}(1990) = 0.01 \pm 0.31$ and $\lambda_{\psi'}(1991) = 1.11 \pm 0.33$. The systematic error due

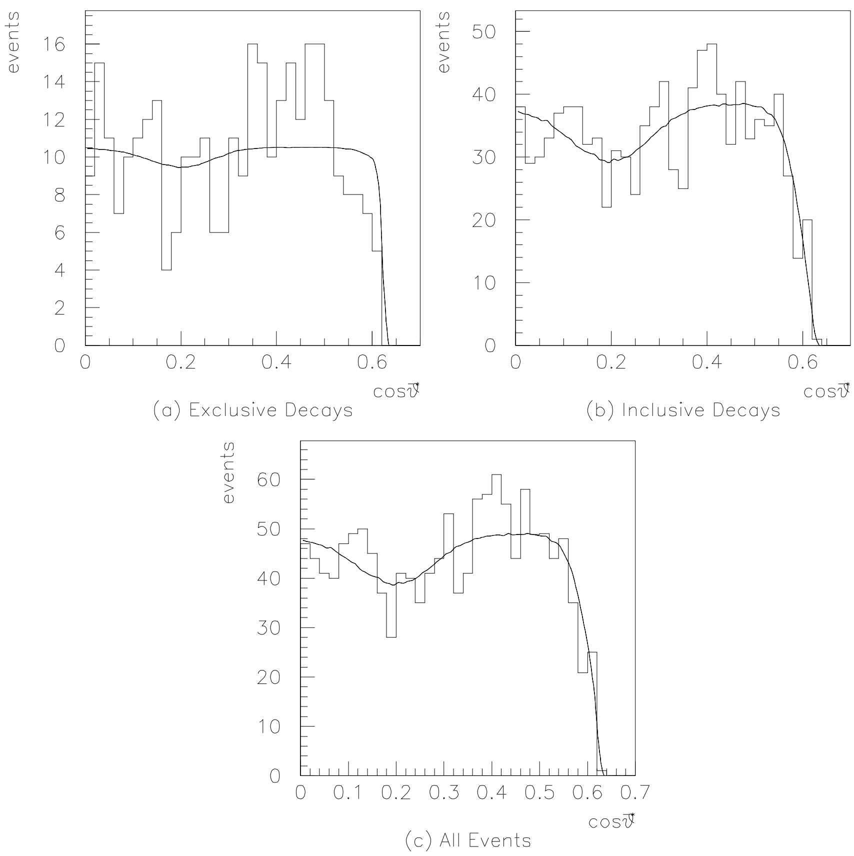

Figure 7.7: Plot of the 1990 ψ' angular distribution for inclusive decays, exclusive decays and all events. The estimated contribution of the background has been subtracted. Overlayed on the plot is the function that maximizes the likelihood. The function is normalized to the number of events.

to the unknown distribution of the background events was conservatively estimated to be 0.25 for the 1990 sample and 0.15 for the 1991 sample. Combining the results, adding both systematic and statistical errors, in gives

$$\lambda_{\psi'} = 0.63 \pm 0.26. \tag{7.7}$$

Figures 7.7 and 7.8 are plots of the $cos\bar{\theta}^*$ distribution for the ψ' background subtracted data samples. Separate plots are made of the inclusive and exclusive event

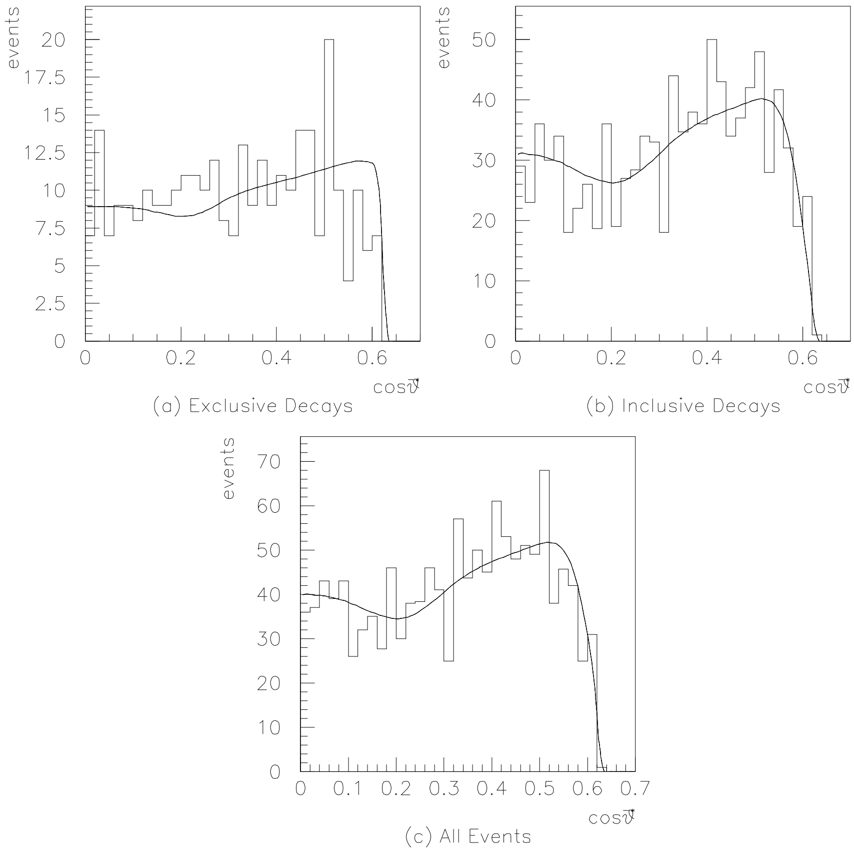

Figure 7.8: Plot of the 1991 ψ' angular distribution for inclusive decays, exclusive decays and all events. The estimated contribution of the background has been subtracted. Overlayed on the plot is the function that maximizes the likelihood. The function is normalized to the number of events.

samples as well as a plot that combines each data sample. Overlayed on the plots are the angular distribution functions that maximize the pseudo-likelihood functions.

7.4.3 Conclusions

Although this is the first experiment to study the angular distribution of the process $\bar{p}p \to J/\psi \to e^+e^-$, the angular distribution of the reverse process has been studied by several electron positron collider experiments[59, 60, 61, 62]. The results of previous experiments and this experiment are give in table 7.4.3. All of the measurements are consistent with the theoretical predictions presented in chapter 2. Combining the measurements of E760, DM2 and Mark-II, gives a world average estimate of $\lambda_{J/\psi} = 0.68 \pm 0.09$. This measurement is inconsistent by more than 2σ with the hypothesis that form factor $F_2 = 0$ proposed by Claudson, Glashow and Wise. The prediction using the distribution amplitude of Gari and Stefanis is also inconsistent with this measurement. Greater precision is required to distinguish between the remaining theoretical predictions.

Experiment	$\lambda_{J/\psi}$
Mark-I	1.45 ± 0.56
DASP	1.7 ± 1.7
Mark-II	0.61 ± 0.23
DM2	0.62 ± 0.11
E760	0.91 ± 0.19

Table 7.3: Results of measurements of $\lambda_{J/\psi}$.

E760 is the first experiment to study the polarization of ψ' formed in proton-antiproton annihilations. However, the measurement of $\lambda_{\psi'}$, lacks the precision necessary to distinguish a prefered theoretical model.

7.5 Measurement of $Br(\psi' \to e^+e^-)$, $Br(\psi' \to J/\psi\pi^0\pi^0)$, $Br(\psi' \to J/\psi\pi^+\pi^-)$ and $Br(\psi' \to J/\psi\eta)$

By measuring the ratio of the number of event collected through various ψ' decay channels and comparing these measurements with the well known $\psi' \to J/\psi X$ decay rate, this experiment is able to provide a better than world average measurement for $Br(\psi' \to e^+e^-)$ and measurements of $Br(\psi' \to J/\psi\pi^0\pi^0)$ and $Br(\psi' \to J/\psi\pi^+\pi^-)$ that have errors comparable to the world average. We are also able to measure $Br(\psi' \to J/\psi\eta)$, but better measurements of this channel have been made by other experiments. Despite this experiment's relatively low statistics, it has low backgrounds for charmonium decays to e^+e^-, making it competitive.

In measuring $Br(\psi' \to e^+e^-)$, values for $Br(\psi' \to J/\psi X)$ and $Br(J/\psi \to e^+e^-)$ from other experiments are required. The world average of $Br(J/\psi \to e^+e^-)$ is $(5.99 \pm 0.25) \times 10^{-2}$ and $Br(\psi' \to J/\psi X)$ is $(57 \pm 4) \times 10^{-2}$. Together, these 2 measurements contribute a limiting 8% systematic error to our results. The expression for the branching fraction of ψ' to e^+e^- is

$$\begin{aligned} \mathrm{B}(\psi' \to e^+e^-) = & \left(\frac{\epsilon_{J/\psi X}}{\epsilon_{ee}}\right)_{geom} \left(\frac{\epsilon_{J/\psi X}}{\epsilon_{ee}}\right)_{trigger} \left(\frac{\epsilon_{J/\psi X}}{\epsilon_{ee}}\right)_{select} \frac{N_{ee}}{N_{J/\psi X}} \\ & \times \mathrm{B}(\psi' \to J/\psi X)\mathrm{B}(J/\psi \to e^+e^-). \end{aligned} \tag{7.8}$$

In this equation ϵ_{geom},$\epsilon_{trigger}$, and ϵ_{select} are the acceptance, trigger efficiency and selection efficiencies for the exclusive (e^+e^-) and inclusive $(J/\psi X)$ decays of ψ'. N_{ee} and $N_{J/\psi X}$ are the numbers of exclusive and inclusive events detected.

Similarly, the expression for the observable inclusive ψ' branching fractions to final state f is

$$\begin{aligned} \mathrm{B}(\psi' \to f) = & \left(\frac{\epsilon_{J/\psi X}}{\epsilon_{f}}\right)_{geom} \left(\frac{\epsilon_{J/\psi X}}{\epsilon_{f}}\right)_{trigger} \left(\frac{\epsilon_{J/\psi X}}{\epsilon_{f}}\right)_{select} \frac{N_{f}}{N_{J/\psi X}} \\ & \times \mathrm{B}(\psi' \to J/\psi X). \end{aligned} \tag{7.9}$$

In this equation f represents detected final states $J/\psi\pi^0\pi^0$, $J/\psi\pi^+\pi^-$ or $J/\psi\eta$. π^0 and η are detected through their decays to $\gamma\gamma$.

7.5.1 Event Selection

As in the angular distribution analysis, in this analysis the cuts are kept loose and data collected near the ψ' resonance is used to estimate the background. This approach maximizes the selection efficiency. The following cuts are applied to select ψ' decay candidates

- $\theta^{lab}_{e^+}$ and $\theta^{lab}_{e^-} \in [15^o, 60^o]$,
- $M_{e^+e^-} > 2.5\frac{GeV}{c^2}$,
- $(ELW_{e^+} \times ELW_{e^-}) > 0.1$,
- All events collected with the 2Č trigger.

Events collected with the 0Č and 1Č triggers are not considered because they include multiplicity cuts on the hodoscopes that have a very low efficiency for the $\psi' \to J/\psi\pi^+\pi^-$ channel. The invariant mass distribution of the candidate electron tracks for the 1990 and 1991 data sets are shown in Figure 7.9 . The shaded region in this data sample is an estimate of the background contamination.

Data Set	Candidates	e^+e^- (4c)	$J/\psi X$ (1c)	$J/\psi\pi^+\pi^-$	$J/\psi\pi^0\pi^0$ (7c)	$J/\psi\eta$ (6c)
ψ' data	1643	216	1029	217	87	23
Background	25	0	2	5	0	0
Effective Back.	203±41	0±8	16 ±11	41±18	0±8	0±8
Internal Back.		0	15	1	0	1.5
Signal	1440±41	216±17	998±34	175±23	87±12	21.5±9

Table 7.4: 1990 ψ' data

From the samples of candidates, events from $\psi' \to e^+e^-$ are selected by means of a 4c kinematical fit. Inclusive $\psi' \to J/\psi X$ decays are selected by a 1c kinematical fit

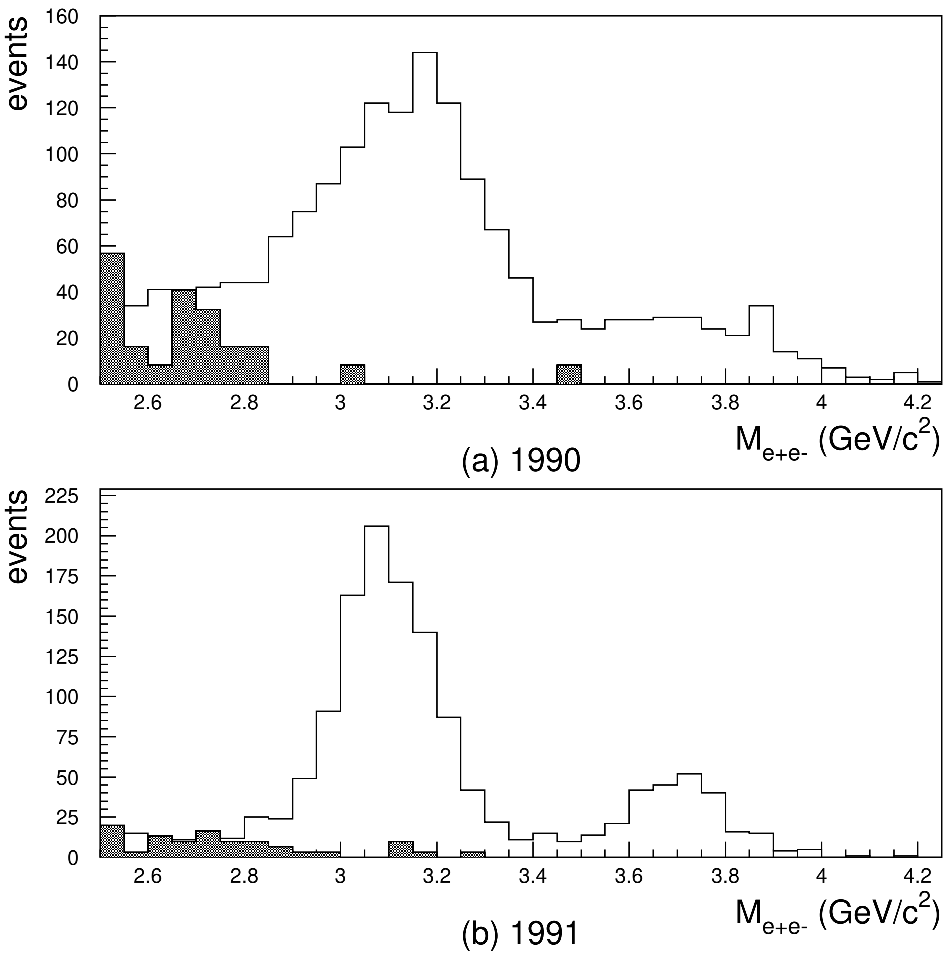

Figure 7.9: e^+e^- mass spectrum for ψ' candidates.

where M_X is allow to vary. Because this fit is so weakly constrained, an additional requirement that the fit probability for the hypothesis $\psi' \to e^+e^-$ is less that 10^{-6} is also applied to the inclusive selection. Inclusive decays of ψ' to $J/\psi\pi^0\pi^0 \to e^+e^-\gamma\gamma\gamma\gamma$ and $J/\psi\eta \to e^+e^-\gamma\gamma$ are selected by means of 7c and 6c kinematical fits respectively. Some events contain showers whose timing is "undetermined". These showers may or may not be associated with the event. The fitting algorithm considers all plausible

Data Set	Candidates	e^+e^- (4c)	$J/\psi X$ (1c)	$J/\psi\pi^+\pi^-$	$J/\psi\pi^0\pi^0$ (7c)	$J/\psi\eta$ (6c)
ψ' data	1396	248	993	199	70	17
Background	34	0	10	3	0	0
Effective Back.	113±19	0±3	33±11	10±6	0	0±3
Internal Back.		0	7	1	0	2
Signal	1283±19	248±16	953±33	188±15	70±9	15±5

Table 7.5: 1991 ψ' data

Channel	$\frac{N_f}{N_{J/\psi X}}$ (1990)	$\frac{N_f}{N_{J/\psi X}}$ (1991)
$\psi' \to e^+e^-$	0.216 ± 0.019	0.260 ± 0.019
$\psi' \to J/\psi\pi^+\pi^-$	0.175 ± 0.024	0.197 ± 0.017
$\psi' \to J/\psi\pi^0\pi^0$	0.087 ± 0.012	0.073 ± 0.010
$\psi' \to J/\psi\eta$	0.022 ± 0.009	0.016 ± 0.005

Table 7.6: Ratios of ψ' decay rates to $J/\psi X$.

combinatorical combinations of "undetermined" showers. The fit which produces the lowest χ^2 is used to evaluate the event. For each of the channels, a χ^2 cut equivalent to a 1% confidence level is made. Because the resolution in the measurement of the energies and angles by the calorimeters are not exactly Gaussian, the χ^2 probability cut efficiency is not 99%. The efficiencies of the fits are determined by Monte Carlo. ψ' decays to $J/\psi\pi^+\pi^-$ are identified by topological cuts alone. $J/\psi\pi^+\pi^-$ candidates are required to have 4 non-adjacent hits in the H2 hodoscope. The 2 hodoscope hits not associated with electron tracks are required to be unassociated with Čerenkov counter hits. The Čerenkov counter requirement is made to exclude backgrounds from the $J/\psi\pi^0\pi^0$ channel where a γ from π^0 converts or a π^0 Dalitz decays to $e^+e^-\gamma$.

Tables 7.4 and 7.5 show the number of events selected for each of the detected channels, the number of events in the background samples, the effective background expected in the data sample, and the internal background. The effective background is simply the measured background scaled according to luminosity. The internal background is the expected number of events from real ψ' decays to other channels that are misidentified. The rates for misidentifying events are determined with the Monte Carlo simulation. The simulation includes $\psi' \to J/\psi\pi^+\pi^-$, $\psi' \to J/\psi\pi^0\pi^0$, $\psi' \to J/\psi\eta$ and radiative transitions through each of the χ states. Table 7.6 shows the ratios of the number of events selected in each of the detectable channels to the number of events selected in the $J/\psi X$ channel.

In the 1990 data, one event was found to pass both the $J/\psi\eta$ and the $J/\psi\pi^o\pi^o$ selections, and two events were found to pass the $J/\psi\pi^+\pi^-$ and the $J/\psi\pi^o\pi^o$ selections. In the 1991 data, there is no overlap between the selected events. This overlap is not unexpected and is accounted for by the internal background estimates.

7.5.2 Selection Efficiency

The efficiency of electron weight cut is determined by its application to a clean sample of $\bar{p}p \to J/\psi \to e^+e^-$ events collected through the $2\check{C}$ trigger and selected by a kinematical fit. For the 1990 J/ψ data, in a sample of 2874 J/ψ events 2799 events have $(ELW_1 \times ELW_2) > 0.1$. The efficiency of this cut is 0.974 ± 0.004. A similar analysis yields an efficiency of 0.983 ± 0.002 for the 1991 J/ψ data. The efficiency of the electron weight cut for the ψ' channels is almost unity and is not expected to vary with channel. Therefore, the electron weight cut does not contribute to $\left(\frac{\epsilon_{J/\psi X}}{\epsilon_f}\right)_{select}$.

The efficiency of the electron positron mass cut is lower for $J/\psi X \to e^+e^-X$ decays of the ψ' than it is for the higher mass $\psi' \to e^+e^-$ decays. Using the GEANT

Monte Carlo simulation, the ratio of the efficiency of the mass cut is determined to be $\left(\frac{\epsilon_{J/\psi X}}{\epsilon_{ee}}\right)_{M_{ee}} = 0.985 \pm .003$ for the 1990 data. The superior energy resolution cut in the 1991 increases the efficiency for 1991 $J/\psi X$ data. The ratio of the efficiency of the mass cut in the 1991 data is $\left(\frac{\epsilon_{J/\psi X}}{\epsilon_{ee}}\right)_{M_{ee}} = 0.992 \pm 0.004$.

The efficiencies of the 4 kinematical fits are determined by GEANT Monte Carlo simulation. Each channel is simulated with both direct decays of charmonium to e^+e^- and radiative decays to $e^+e^-\gamma$ as predicted by Q.E.D. If the radiative contribution was neglected, the 4c fit efficiency would have been over-estimated by about 5% and the 1c fit efficiency by about 1%. Table 7.7 shows the estimated fit efficiency for each of the ψ' decay channels. In this table the efficiencies for decays to $J/\psi\pi^0\pi^0$ and $J/\psi\eta$ include the angular acceptance of the γs and the branching fractions of π^0 and η to $\gamma\gamma$. In table 7.8 are the estimated and measured efficiencies for fits to $\bar{p}p \to J/\psi \to e^+e^-$ and $\bar{p}p \to \chi_2 \to J/\psi\gamma \to e^+e^-\gamma$. J/ψ and χ_2 events can be cleanly selected with only electron weight and mass cuts, making it possible to measure their fit efficiencies directly. The J/ψ events are fitted with 4 constraints, and χ_2 sample is selected by a 1c fit where the γ from the radiative transition to J/ψ is not measured and M_γ is allowed to vary. These data provide a test of the accuracy of the Monte Carlo simulation.

The efficiency of the $J/\psi\pi^+\pi^-$ selection was determined with the charged trigger simulation. The selection efficiency for the 1990 data was determined to be 0.369±0.010. The selection efficiency for the 1991 data is 0.368±0.010. The error in the efficiencies are due to the uncertainty in the rate for spurious hits in H2.

The selection efficiencies for $\psi' \to J/\psi\pi^+\pi^-$ is estimated with the trigger Monte Carlo.

The ratios of the selection efficiencies for the 4 detected ψ' decays to the selection efficiency for detection of $\psi' \to J/\psi X$ are given in table 7.9.

Channel	ϵ_{fit} MC(1990)	ϵ_{fit} MC(1991)
$\psi' \to e^+e^-$	$0.715 \pm .047$	0.848 ± 0.01
$\psi' \to J/\psi X$	$0.853 \pm .029$	0.932 ± 0.01
$\psi' \to J/\psi\pi^0\pi^0$	$0.188 \pm .009$	0.224 ± 0.014
$\psi' \to J/\psi\eta$	$0.488 \pm .022$	0.546 ± 0.017

Table 7.7: Fit efficiencies for ψ' decay channels.

Channel	ϵ_{fit} MC(1991)	ϵ_{fit} Meas. (1991)
$J/\psi \to e^+e^-$	0.896 ± 0.005	0.894 ± 0.005
$\chi_2 \to e^+e^-\gamma$	0.902 ± 0.007	0.916 ± 0.006

Table 7.8: A test of the Monte Carlo Simulation using clean samples of J/ψ and χ_2 decays collected during the 1991 data run.

Channel	$\left(\frac{\epsilon_{J/\psi X}}{\epsilon_f}\right)_{select}$(1990)	$\left(\frac{\epsilon_{J/\psi X}}{\epsilon_f}\right)_{select}$(1991)
$\psi' \to e^+e^-$	1.17 ±0.04	1.090±0.006
$\psi' \to J/\psi\pi^+\pi^-$	2.31 ±0.07	2.53 ±0.03
$\psi' \to J/\psi\pi^0\pi^0$	4.54 ±0.14	4.17 ±0.03
$\psi' \to J/\psi\eta$	4.51 ±0.15	4.40 ±0.09

Table 7.9: Ratio of the $\psi' \to J/\psi X$ selection efficiency to selection efficiencies of the ψ' final states.

7.5.3 Trigger Efficiency and Acceptance

The 2Č trigger contains a multiplicity cut on the number of hits in the hodoscope arrays: $N_{H1} \leq 4$ and $N_{H2} \leq 4$. Although this cut does not exclude any ψ' decay channels directly, 4 charged track decays, such as the dominant $\psi' \to J/\psi\pi^+\pi^-$ decays, can be rejected in the event of an extra spurious hit in either hodoscope. As discussed in chapter 4, the dominant source for spurious hits in H1 is δ-rays from beam-target interactions, and the dominant source in H2 is δ-rays from interactions of charges tracks with the detector materials. The trigger Monte Carlo simulation is used to determine the trigger efficiency for each channel as a function of the angular distribution parameter $\lambda_{\psi'}$.

The angular distribution for both exclusive and inclusive ψ' decays has been shown to be $1 + \lambda_{\psi'} cos^2\theta^*$, where $\lambda_{\psi'}$ depends entirely on the formation helicity amplitudes. Because both the inclusive and exclusive channels have the same form, the ratio of the acceptances for the inclusive and exclusive channels varies by only 0.5% over a wide range of allowed values of $\lambda_{\psi'}$. This is despite the fact that in the same range of $\lambda_{\psi'}$ the absolute acceptance for either the exclusive channel or the inclusive channel vary by more than 10%. The exception to this rule is the $J/\psi\eta$ decay channel. Because of the negative parity of the η, the angular distribution of this decay is $1 + \lambda_{\psi'} cos^2\theta^*$ as it is for e^+e^- and $J/\psi\pi\pi$ decays, but $1 - \frac{4\lambda_{\psi'}}{5\lambda_{\psi'}+4} cos^2\theta^*$. For this reason, the error in $\left(\frac{\epsilon_{J/\psi X}}{\epsilon_f}\right)_{trig/geom}$ is about 10 times larger (5% compared with 0.5%) for $J/\psi\eta$ decays than for e^+e^- decays.

Channel	$\left(\frac{\epsilon_{J/\psi X}}{\epsilon_f}\right)_{trig/geom}$ (1990)	$\left(\frac{\epsilon_{J/\psi X}}{\epsilon_f}\right)_{trig/geom}$ (1991)
$\psi' \to e^+e^-$	0.903±0.005	0.900±0.005
$\psi' \to J/\psi\pi^+\pi^-$	1.070 ±0.005	1.070 ±0.005
$\psi' \to J/\psi\pi^0\pi^0$	0.952±0.009	0.944±0.009
$\psi' \to J/\psi\eta$	0.808 ±0.041	0.802±0.041

Table 7.10: Ratio of $\psi' \to J/\psi X$ acceptance and trigger efficiency to the acceptance and trigger efficiencies of ψ' final states.

The combined trigger efficiency and acceptance are given in table 7.10. Included in the acceptance for $\psi' \to J/\psi\eta$ is the branching fraction for η to decay to $\gamma\gamma$. The efficiency ratio reported for the $J/\psi\pi^+\pi^-$ channel includes the selection efficiency.

7.5.4 ψ' Branching Fractions

Inserting the measured rates, estimated efficiencies, and the PDG [37] value for $Br(\psi' \to J/\psi X)$ and $Br(J/\psi \to e^+e^-)$ into equations 1.9 and 1.10 yields the values given in table 7.11. Combining the 1990 and 1991 data sets the best estimates of the

Channel	Br (1990) ($\times 10^{-2}$)	Br (1991) ($\times 10^{-2}$)
$\psi' \to e^+e^-$	$0.78 \pm 0.07_{stat} \pm 0.06_{syst}$	$0.87 \pm 0.07_{stat} \pm 0.07_{syst}$
$\psi' \to J/\psi\pi^+\pi^-$	$24.7 \pm 3.5_{stat} \pm 1.7_{syst}$	$30.4 \pm 2.7_{stat} \pm 2.1_{syst}$
$\psi' \to J/\psi\pi^0\pi^0$	$21.4 \pm 3.0_{stat} \pm 1.5_{syst}$	$16.5 \pm 2.4_{stat} \pm 1.2_{syst}$
$\psi' \to J/\psi\eta$	$4.6 \pm 1.9_{stat} \pm 0.3_{syst}$	$3.2 \pm 1.0_{stat} \pm 0.2_{syst}$

Table 7.11: Results.

branching fractions are

$$Br(\psi' \to e^+e^-) = (0.83 \pm 0.05_{stat} \pm 0.07_{syst}) \times 10^{-2}, \tag{7.10}$$

$$Br(\psi' \to J/\psi\pi^+\pi^-) = (28.3 \pm 2.1_{stat} \pm 2.0_{syst}) \times 10^{-2}, \tag{7.11}$$

$$Br(\psi' \to J/\psi\pi^0\pi^0) = (18.4 \pm 1.9_{stat} \pm 1.3_{syst}) \times 10^{-2}, \tag{7.12}$$

$$Br(\psi' \to J/\psi\eta) = (3.5 \pm 0.9_{stat} \pm 0.2_{syst}) \times 10^{-2}. \tag{7.13}$$

The statistical errors are added in quadrature and the systematic errors, being from the same source, are carried through the average unchanged.

7.5.5 Conclusions

The results of this experiment are presented in table 7.12 with the previous published values and the PDG[37] world averages. All the results of this experiment are consistent with the previously determinations and significantly improve upon the world

Channel	**E760**($\times 10^{-2}$)	previous ($\times 10^{-2}$)	Reference
$\psi' \to e^+e^-$	$0.83 \pm 0.05_{stat} \pm 0.07_{syst}$	0.93 ± 1.6	Mark I [63]
		0.88 ± 0.13	PDG [37]
$\psi' \to J/\psi\pi^+\pi^-$	$28.3 \pm 2.1_{stat} \pm 2.0_{syst}$	32.0 ± 4.0	Mark I [64]
		36.0 ± 6.0	DASP [65]
		32.4 ± 2.6	PDG [37]
$\psi' \to J/\psi\pi^0\pi^0$	$18.4 \pm 1.9_{stat} \pm 1.3_{syst}$	18.0 ± 6.0	DASP [65]
		18.4 ± 2.7	PDG [37]
$\psi' \to J/\psi\eta$	$3.5 \pm 0.9_{stat} \pm 0.2_{syst}$	2.5 ± 0.6	Mark II [66]
		2.18 ± 0.14	CBAL [67]
		3.6 ± 0.5	CNTR [68]
		2.7 ± 0.4	PDG[37]

Table 7.12: Comparison of E760 results for ψ' branching fractions with previous determinations.

average for the $\psi' \to e^+e^-$ mode. They modestly improve upon the world averages for the $\psi' \to J/\psi\pi^+\pi^-$ and $\psi' \to J/\psi\pi^0\pi^0$ modes.

Chapter 8

Observation of $J/\psi \to e^+e^-\gamma$

In e^+e^- collider experiments large backgrounds exist to e^+e^- and $e^+e^-\gamma$ final states from direct electron-positron scattering. In this experiment such backgrounds do not exist, making it possible to detect the decay $J/\psi \to e^+e^-\gamma$. The three sources of background that are not negligible are e^+e^- events in which bremsstrahlung interactions with material in the beam pipe or the inner detectors produce a radiated photon, e^+e^- events with an extra shower from an unrelated $\bar{p}p$ annihilation, and non-resonant hadronic interactions that are misidentified as $e^+e^-\gamma$ events. Interactions of electrons with detector materials are simulated with the GEANT Monte Carlo. In the 1991 data, timing information is available to determine if showers are on-time, sharply reducing backgrounds from pileup showers. Data collected near the J/ψ resonance is used to directly measure the non-resonant background.

Observation of $J/\psi \to e^+e^-\gamma$ has never been reported. However, the decay $J/\psi \to \mu^+\mu^-\gamma$ was observed by the Mark III experiment[69], and found to be consistent with QED predictions. The reaction $e^+e^- \to e^+e^-\gamma$ was studied as a possible source of background for $\pi^+\pi^-\gamma$ decays of the J/ψ by the Mark III experiment[70]. They concluded that the radiative Bhabha rate is the dominate channel for producing the $e^+e^-\gamma$ final state.

The ratio of the decay rate of $\Gamma(J/\psi \to e^+e^-\gamma)$ to the non-radiative process is

$$\frac{d\Gamma^{e^+e^-\gamma}}{\Gamma^{e^+e^-}} = \frac{\alpha}{\pi^2}\left(1-\frac{2\omega}{\sqrt{s}}\right)^2 \frac{d\omega}{\omega}\left(\frac{sin^2\theta'_\gamma}{(1-\beta_e^2 cos^2\theta'_\gamma)^2}\right) d\Omega'_\gamma. \tag{8.1}$$

In this equation, ω is the energy of the radiated photon in the overall center of mass frame and θ'_γ is the angle between the positron and the radiated photon in the e^+e^- center of mass system. Notice that the distribution of the photon energy and the photon angle are nearly decoupled. The θ'_γ distribution is sharply peaked at $\theta'_\gamma \approx \sqrt{3(1-\beta_e^2)} \approx 10^{-3}$ rad, and falls off as $\frac{1}{sin\theta'_\gamma}$ as θ'_γ increases. Because this experiment has no magnetic field, typically the photon showers overlap with the electron shower in the calorimeter and are undetectable. The photon energy distribution is divergent with falling photon energy as expected for a radiative process.

10,000 $J/\psi \to e^+e^-$ and 60,000 $J/\psi \to e^+e^-\gamma$ events are generated that pass the trigger simulation. An energy cutoff of 20 MeV and an opening angle cutoff of 2 mrad are applied in the simulation to remove the energy divergence and the almost diverging portion of the theta distribution. These data are boosted to the E760 lab frame and processed by the GEANT[50] Monte Carlo simulation. The program tracks the primary particles through the beam pipe and inner detector systems where scattering and production of secondaries due to interactions with materials are simulated. Both data sets are reconstructed with the analysis program used to reconstruct data.

The following cuts are applied to the 1991 filtered J/ψ data set as well as the two Monte Carlo data sets to select J/ψ candidates:

- $\theta^{lab}_{e^+}$ and $\theta^{lab}_{e^-} \in [15^o, 60^o]$,
- $M_{e^+e^-} > 2.5\frac{GeV}{c^2}$,
- $(ELW_{e^+} \times ELW_{e^-}) > 1.5$ (not applied to MC data),

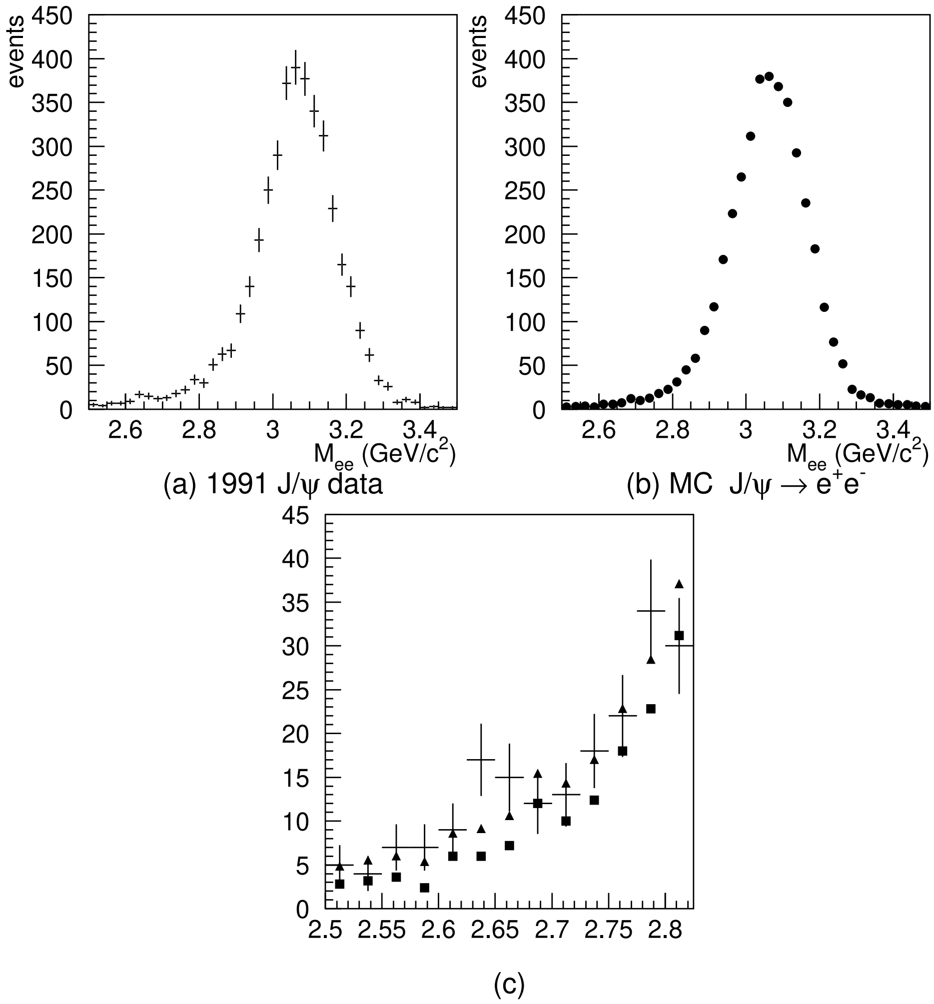

Figure 8.1: Mass of electron-positron pair for J/ψ decay candidates from (a) 1991 J/ψ data, (b) Monte Carlo $J/\psi \to e^+e^-$ and (c) Comparison data (+), MC $J/\psi \to e^+e^-$ ($\square$) and MC $J/\psi \to MCe^+e^-$ and $J/\psi \to e^+e^-\gamma$ as predicted by QED ($\triangle$).

A total of 3933 candidate events were selected from the data. Figure 8.1 shows the electron pair mass distributions for the three data sets. Notice that the low mass tail in the data cannot be adequately simulated by the e^+e^- decays alone.

From the J/ψ candidate event subset, $J/\psi \to e^+e^-\gamma$ events are selected by requiring that one and only one extra shower exists with:

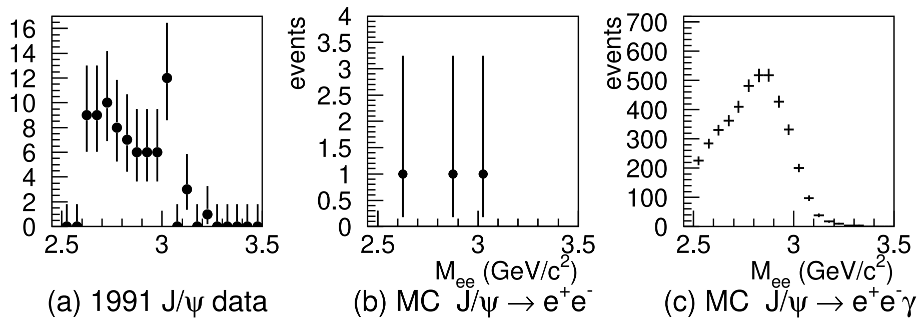

Figure 8.2: Electron-positron mass distribution for $J/\psi \to e^+e^-\gamma$ candidates in (a) 1991 J/ψ data., (b) Monte Carlo $J/\psi \to e^+e^-$ and (c) Monte Carlo $J/\psi \to e^+e^-\gamma$

- Energy > 200 MeV,
- Extra shower is separated from both the e^+ and e^- showers by more than 200 mrad,
- Extra shower is either on-time or its timing is undetermined.

77 events from the J/ψ candidate subset are selected. The cut in opening angle guarantees that all three showers are isolated. This reduces backgrounds from bremsstrahlung interactions of the electron and positron with the detector materials and eliminates backgrounds from single electron or positron showers, with large transverse fluctuations, mistakenly being reconstructed as two showers. Figure 8.2 is a plot of the electron-positron mass for events passing the $J/\psi \to e^+e^-\gamma$ event selection. Notice that only three events from the MC $J/\psi \to e^+e^-$ sample pass the $e^+e^-\gamma$ selection. This represents a normalized background of one event in the data. Backgrounds from interactions with detector materials are nearly negligible with these cuts.

Figures 8.3 and 8.4 show the total lab energy and invariant mass distributions for the $J/\psi \to e^+e^-\gamma$ candidates. Mass and lab energy distributions for both the e^+e^- alone and all three particles are plotted. For a majority of the events, the total energy and mass of the e^+e^- alone are well below the total lab energy and J/ψ mass.

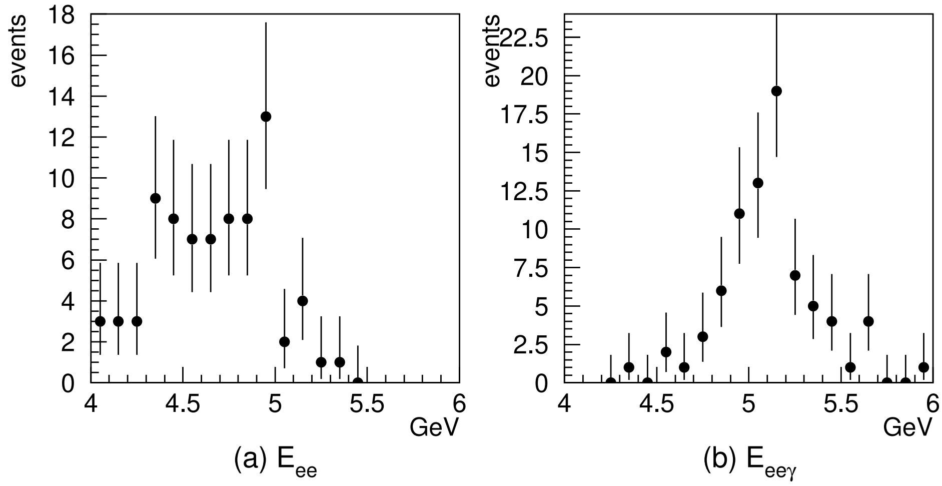

Figure 8.3: Total lab energy of (a) the e^+e^- pair and (b) the e^+e^- pair and the radiated photon. The total energy available in the lab frame is 5.11 GeV.

However, with the addition of the extra shower, the distributions become centered about the total available energy and the J/ψ mass. This is clear evidence that the background from pileup showers is small. Were a substantial portion of the sample from e^+e^- decays of J/ψ accompanied by a pileup photon, the plot of M_{ee} would be sharply peaked near the J/ψ mass and the energy of the e^+e^- pair would be peaked near the total lab energy. Additional showers would push the mass and the energy higher and broaden the distributions. In the sample of 77 $e^+e^-\gamma$ candidates, the background contribution from pileup is estimated by fitting the electron-positron mass spectrum to a normalized linear combination of the pure e^+e^- decay mass distribution (figure 8.1b) and the e^+e^- mass distribution expected for $e^+e^-\gamma$ events (figure 8.2c). The fit determines the $e^+e^-\gamma$ contribution to be $(86 \pm 7)\%$ of the sample. A second fit was performed on the e^+e^- energy distribution. As with the mass fit, a linear combination of the energy distributions for the simulated e^+e^- and $e^+e^-\gamma$ samples was fit to the data. The energy fit estimates the $e^+e^-\gamma$ contribution to be $85 \pm 7\%$. The two fits are consistent, but also highly correlated, so the errors are not combined

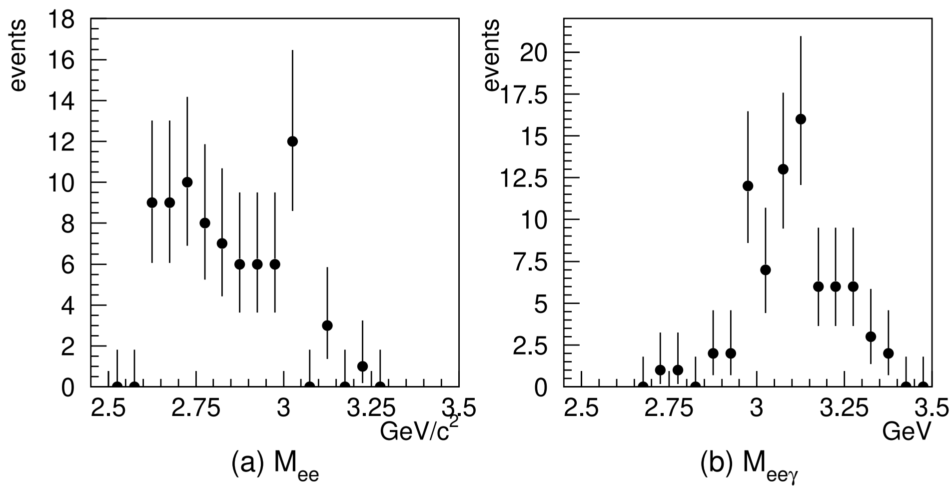

Figure 8.4: Invariant mass of (a) the e^+e^- pair and (b) the e^+e^- pair and the radiated photon.

in quadrature. Figure 8.5 shows the best fit curves for both fits and the estimated contribution from e^+e^- events. The estimated background from pileup is 10.4 ± 5.2 events.

The background from non-resonant $\bar{p}p$ annihilations can be easily estimated by applying the cuts to data taken away from the J/ψ resonance. The principal component of this background is $\bar{p}p \to \pi^0\pi^0$ where the π^0's either Dalitz decay or a photon converts in the beam pipe. Application of the cuts for $e^+e^-\gamma$ selection to the data collected in the region of the η_c yields 10 events. The η_c data sample is 3.3 times larger than the J/ψ data sample, so the estimated background from all non-resonant sources is 3.0 ± 1.0 events.

The background contribution from bremsstrahlung by the electron or positron in the beam pipe or inner detectors is estimated with the $J/\psi \to e^+e^-$ Monte Carlo simulation. three of the 10,000 events simulated pass the selection criteria for $e^+e^-\gamma$. This represent a normalized background of 1.0 ± 0.6 events.

Subtracting all backgrounds, the estimated number of $e^+e^-\gamma$ events in the data

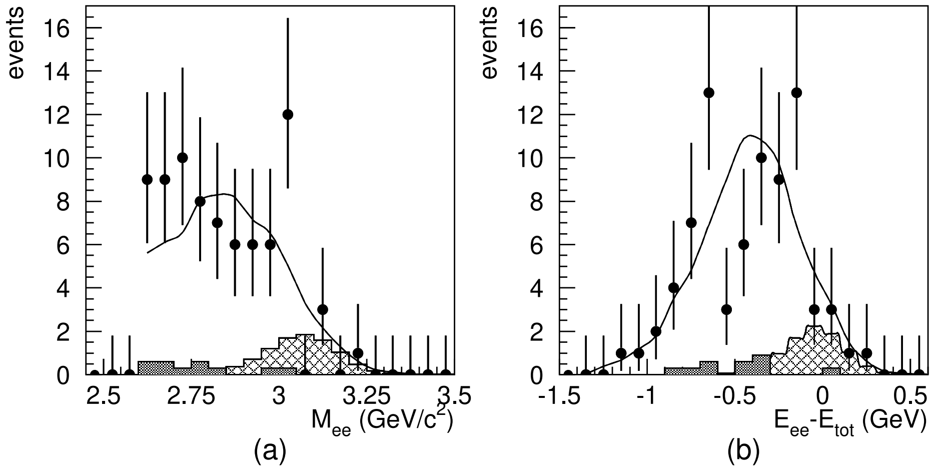

Figure 8.5: Fit to $e+e-$ mass and energy distributions. The estimated contribution from e^+e^- plus a pileup shower is shown as the hatched regions. The shaded area is the estimated non-resonant background.

sample is 62.6 ± 10.3 events.

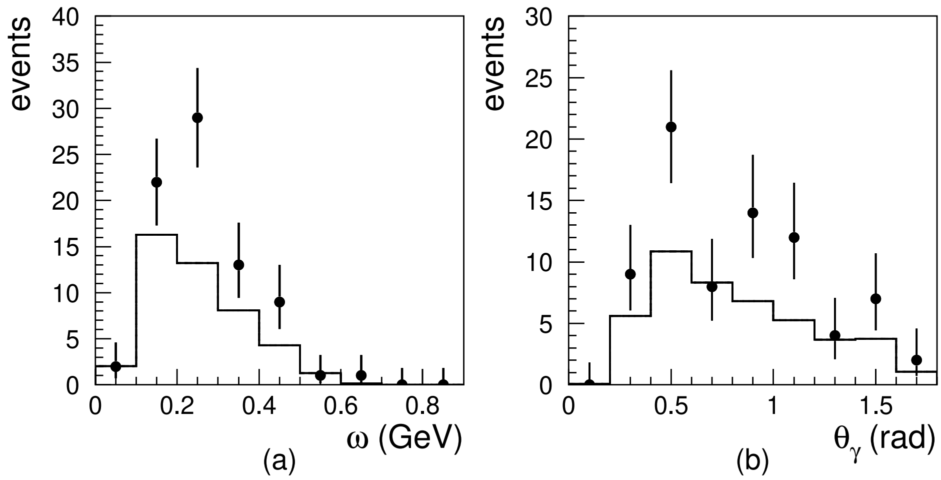

Figure 8.6: Comparison between MC (solid line) and data for $J/\psi \to e^+e^-\gamma$. Figure (a) is the CMS energy distribution of the radiated photon. Figure (b) is the CMS opening angle between the radiated photon and the nearest e^+ or e^- track.

The ratio of the contributions of the $J/\psi \to e^+e^-$ and $J/\psi \to e^+e^-\gamma$ is determined by integrating equation 8.1 with the cutoffs imposed in the simulation. The simulated data set is normalized to the number total events that pass the J/ψ candidate selection criteria, 3933. 44 events are predicted by QED to be compared with 62.3 ± 10.3 events observed in the data. The measurement is consistent with the predicted rate, and there is no evidence for $\bar{p}p \to J/\psi \to e^+e^-\gamma$ events from any source other than final state radiation in this experiment. Figure 8.6 shows the expected (solid line) and measured distributions for the center of mass system energy and opening angle of the radiated photon. There is good consistency between the predicted and the measured distributions.

Bibliography

[1] T.A. Armstrong et al. Study of χ_1 and chi_2 charmonium states formed in $\bar{p}p$ annihilations. *Nucl. Phys. B*, 373:35, 1992.

[2] T.A. Armstrong et al. Observation of the $^1\mathrm{p}_1$ state of charmonium. *Phys. Rev. Lett.*, 69:2337, 1992.

[3] T.A. Armstrong et al. Precision measurements of charmonium states formed in $\bar{p}p$ annihilations. *Phys. Rev. Lett.*, 68:1468–1471, 1992.

[4] T.A. Armstrong et al. Measurement of the $\gamma\gamma$ partial width of the χ_2 charmonium resonance. *Phys. Rev. Lett.*, 70:2988, 1993.

[5] T.A. Armstrong et al. Production of the $f_2(1520)$ resonance in antiproton-proton annihilations at $2980 < \sqrt{s} < 3526$ mev. *Phys. Lett. B*, 307:399, 1993.

[6] T.A. Armstrong et al. Measurement of the j/ψ and ψ' resonance param-eters in $\bar{p}p$ annihilations. *Physical Review D*, 47:772, 1993.

[7] T.A. Armstrong *et. al.* Proton electromagnetic form factors in the timelike region from 8.9 to 13.0 gev^2. *Phys. Rev. Lett.*, 70:1212, 1993.

[8] T. A. Armstrong *et. al.* Study of the $\eta_c(1^1s_0)$ state of charmonium formed in $\bar{p}p$ anihilations and a search for the $\eta_c'(2^1s_0)$. *Physical Review D*, 59(9):4839–4854, 1995.

[9] M. Gell-Mann. A schematic model of baryons and mesons. *Phys. Lett.*, 8(3):214–215, 1964.

[10] G. Zweig. Cern report no. 8182/th. 401. Technical report, CERN, 1964.

[11] B.J. Bjørken and S.L. Glashow. Elementry particles and su(4). *Phys. Lett.*, 11(3):255–257, 1964.

[12] L. Maiani S.L. Glashow, J. Iliopoulos. Weak interactions with lepton-hadron symmetry. *Physical Review D*, 2(7):1285–1292, 1970.

[13] N. Cabibbo. Unitary symmetry and leptonic decays. *Phys. Rev. Lett.*, 10(12):531–533, 1963.

[14] M. Kobayashi and T. Masakawa. Cp-violation in the renormalizable theory of weak interactrions. *Progress of Theoretical Physics*, 49:652–657, 1973.

[15] M.K. Gaillard and B.W. Lee. Rare decay modes of the k meson in gauge theories. *Physical Review D*, 10(3):897–916, 1974.

[16] T. Appelquist and D. Politzer. Heavy quarks and e^+e^- annihilations. *Phys. Rev. Lett.*, 34(1):43–45, 1975.

[17] J.E. Augustin *et. al.* Discovery of a narrow resonance in e^+e^- annihilation. *Phys. Rev. Lett.*, 33(23):1406–1408, 1974.

[18] J.J. Aubert *et. al.* Experimental observation of a heavy particle j. *Phys. Rev. Lett.*, 33(23):1404–1406, 1974.

[19] A.M. Boyarski et. al. Quantum numbers and decay widths of the $\psi(3095)$. *Phys. Rev. Lett.*, 34(21):1357–1359, 1975.

[20] V. Luth *et. al.* Quantum numbers and decay widths of the $\psi(3684)$. *Phys. Rev. Lett.*, 35(17):1124–1126, 1975.

[21] R. Brandelik *et. al.* Results from dasp on e^+e^- annihilation between 3.1 and 5.2 gev. *Zeitschrift Fuer Physik C: Particles and Fields*, 1:233–256, 1979.

[22] D. Coffman et. al. Direct measurement of the j/ψ leptonic branching fraction. *Phys. Rev. Lett.*, 68(3):282–285, 1975.

[23] C. Baglin *et. al.* Search for the ^{1}p$_1$ charmonium state in $\bar{p}p$ annihilations at the cern intersecting storage rings. *Phys. Lett. B*, 171:135–141, 1986.

[24] C. Baglin *et. al.* Formation of the chi_1 and chi_2 charmonium resonances in antiproton-proton annihilation and measurements of their masses and total widths. *Phys. Lett. B*, 172:455–460, 1986.

[25] C. Baglin *et. al.* Angular distributions in the reactions $\bar{p}p$ to $\chi_{1,2}$ to gamma psi to gamma e$^+$e$^-$. *Phys. Lett. B*, 195:85–90, 1987.

[26] C. Baglin *et. al.* j/ψ resonant formation and mass measurement in antiproton-proton annihilations. *Nucl. Phys. B*, 286:692–634, 1987.

[27] M.N. Rosenbluth. High energy elastic scattering of electrons and protons. *Phys. Rev.*, 79:615, 1950.

[28] M.B. Wise M. Claudson, S.L. Glashow. Isospin violation in $j/\psi \rightarrow$ baryon + antibaryon. *Physical Review D*, 25(5):1345–1347, 1982.

[29] C. Carimalo. Quark mass effects in $\psi \rightarrow \bar{B}b$ decays. *Int. J. Mod. Phys. E*, A2:249–263, 1987.

[30] F. Murgia and M. Melis. Mass corrections in $j/\psi \to b\bar{B}$ decay and the role of distribution amplitudes. *Physical Review D*, 51(7):3487–3500, 1995.

[31] V.L. Chernyak and I.R. Zhitnitsky. Asymptotic behaviour of exclusive processes in qcd. *Physics Reports*, 112:174, 1984.

[32] A.A. Ogloblin V.L. Chernyak and I.R. Zhitnitsky. Wave functions of octet baryons. *Z. Phys. C*, 42:569–82, 1989.

[33] I.D. King and C.T. Sachrajda. Nucleon wavefunctions and qcd sum rules. *Nucl. Phys. B*, 279:785–803, 1987.

[34] M. Gari and N.G. Stefanis. Electromagnetic form factors of the nucleon from perturbative qcd and qcd sum rules. *Phys. Lett. B*, 175:462–466, 1986.

[35] N.G. Stefanis and M. Bergmann. Nucleon distribution amplitude: the heterotic solution. *Physical Review D*, 47:3685–3689, 1993.

[36] T. Himmel. *Decays of the ψ'(3684) to other charmonium states.* PhD thesis, Stanford University, 1980.

[37] L. Montanet *et. al.* Particle Data Group. Review of particle properties. *Physical Review D*, 50(3):1173–1826, 1994.

[38] Fermi National Accelator Laboratory. Design report: Tevetron 1 project. Technical report, Universities Research Association, Inc., Batavia, IL, 1984. unpublished.

[39] Universities Research Association. Design report tevetron 1 project. Technical report, Fermi National Accelerator Laboratory, 1984.

[40] J. D. Reid. *Production of two pseudoscalar mesons in antiproton-proton annihilations at 2.9 ¡ $\sqrt{s}$ 3.6 GeV*. PhD thesis, Pennsylvania State University, 1993.

[41] M. Macri. Gas jet targets. In *CERN Accelerator Summer School*, 1983.

[42] S. Trokenheim, M. Sarmiento, K. K. Seth, and L. Bartoszek. A $\bar{p}p$ luminosity monitor for fermilab experiement e760. *Nucl. Instrum. Methods*, A355:308–319, 1995.

[43] C. Biino, R. Mussa, S. Palestini, N. Pastore, and L. Pesando. Charge division in a small proportional chamber constructed with aluminum mylar tubes. *Nucl. Instrum. Methods*, A271:417–422, 1988.

[44] C. Calabreese, V. Carassiti, P. Dalpiaz, P.F. Dalpiaz, E. Luppi, M. Martini, S. Palestini, F. Petrucci, and M. Savri. A cylindrical mwpc and radial projection chamber for the e760 experiment. *Nucl. Instrum. Methods*, A277:116–120, 1989.

[45] C. Binno, G. Borreani, A. Ceccucci, R. Cester, G. Dughera, G. Giraudo, M. Mandelkern, F. Marchetto, E. Menichetti, A. Migliori, R. Mussa, S. Palestini, N. Pastrone, L. Pesando, and G. Rinaudo. A large acceptance threhold cherenkov counter for experiment e760 at fermilab. *Nucl. Instrum. Methods*, A317:135–142, 1992.

[46] L. Bartoszek *et. al.* The e760 lead-glass central calorimeter: design and initial test results. *Nucl. Instrum. Methods*, A301:47, 1991.

[47] M. A. Hasan *et. al.* The fermilab-e760 forward electromagnetic calorimeter. *Nucl. Instrum. Methods*, A295:73–80, 1990.

[48] R. Ray *et. al.* A trigger for the fermilab e760 lead-glass calorimeter. *Nucl. Instrum. Methods*, A307:245–264, 1991.

[49] J. L. Marques. *Study of the χ_1 and χ_2 States Produced in $\bar{p}p$ Annihilations in Fermilab Experiment E760.* PhD thesis, University of California, Irvine, 1992.

[50] R. Brun *et. al.* *GEANT Detector Description and Simulation Tool: CERN Programing Library Long Writeup W5013*, version 3.21 edition.

[51] B. Rossi. *High-Energy Particles.* Prentice-Hall, Inc., 1952.

[52] K. E. Gollwitzer. *The Charmonium $^1P_1$ State (h_c) Produced in Antiproton-proton Annihilations.* PhD thesis, University of California, Irvine, 1993.

[53] G.A. Akopdjanov *et*. al. Determination of photon coordinates in a hodoscope Čerenkov spectrometer. *Nucl. Instrum. Methods*, 140:441–445, 1977.

[54] W.T. Vetterling W.H. Press, S.A. Teukolsky and B.P. Flannery. *Numerical Recipes in FORTRAN.* Cambridge University Press, 1986.

[55] F. James. *MINUIT Functional Minimization and Error Analysis Reference Manual.*

[56] C. Patrignani. A criterium to select inclusive j/ψ events. E760 collaboration memo.

[57] B. Pire T.N. Pham and T.N. Truong. two-pion spectrum and angular distribution in $\psi' \rightarrow \psi + 2\pi$ decays. *Phys. Lett. B*, 61b:183–186, 1976.

[58] L. Lyons. *Statistics for nuclear and particle physicists.* Cambridge University Press, 1993.

[59] I. Peruzzi *et. al.* Baryonic decays of the psi (3095). *Physical Review D*, 17(11):2901–2914, 1978.

[60] M.W. Eaton *et. al.* Decays of the $\psi(3097)$ to baryon-antibaryon final states. *Physical Review D*, 29(5):804–821, 1984.

[61] D. Cords. Lectures presented at the int. school of elementary particle physics. DESY preprint 78-32, July 1977.

[62] D. Pallin *et. al.* Baryon pair production in j/ψ decays. *Nucl. Phys. B*, 292:653–669, 1987.

[63] V. Luth et. al. Quantum numbers and decay widths of the $\psi(3684)$. *Phys. Rev. Lett.*, 35:1124–1126, 1975.

[64] G. Abrams *et. al.* Decay of $\psi(3684)$ into $\psi(3095)$. *Phys. Rev. Lett.*, 34(18):1181–1183, 1975.

[65] B. Wiik *et. al.* Recent results from doris. In *International Symposium on Lepton-Photon Interactions*, volume 69, 1975.

[66] T. Himel *et. al.* Observations of the $\eta_c(2980)$ produced in the radiative decay of the $\psi'(3684)$. *Phys. Rev. Lett.*, 45(4):1146–1149, 1980.

[67] M. Oreglia *et. al.* Measurement of the decays ψ' to $\eta j/\psi$ and ψ' to $\pi^0 j/\psi$. *Phys. Rev. Lett.*, 45(12):959–962, 1980.

[68] W. Bartel *et. al.* Cascade radiative decays of $\psi'(3684)$ and evidence for a new intermediate state of even c-parity. *Phys. Lett. B*, 79(4):492–496, 1978.

[69] John Scott Brown. *Selected Studies of Elastic and Radiative Two Body Decays of Charmonium.* PhD thesis, University of Washington, 1984.

[70] Timothy Alan Bolton. *Radiative Decays of J/ψ to Two Pseudoscalar Final States.* PhD thesis, Stanford University, 1988.